SCIENTIFIC REPORTS
nature research

OPEN

Precursory worldwide signatures of earthquake occurrences on Swarm satellite data

A. De Santis[1*], D. Marchetti[1,2], F. J. Pavón-Carrasco[1,3], G. Cianchini[1], L. Perrone[1], C. Abbattista[4], L. Alfonsi[1], L. Amoruso[4], S. A. Campuzano[1], M. Carbone[4], C. Cesaroni[1], G. De Franceschi[1], Anna De Santis[1], R. Di Giovambattista[1], A. Ippolito[1,5], A. Piscini[1], D. Sabbagh[1], M. Soldani[1], F. Santoro[4], L. Spogli[1,6] & R. Haagmans[7]

The study of the preparation phase of large earthquakes is essential to understand the physical processes involved, and potentially useful also to develop a future reliable short-term warning system. Here we analyse electron density and magnetic field data measured by *Swarm* three-satellite constellation for 4.7 years, to look for possible *in-situ* ionospheric precursors of large earthquakes to study the interactions between the lithosphere and the above atmosphere and ionosphere, in what is called the Lithosphere-Atmosphere-Ionosphere Coupling (LAIC). We define these anomalies statistically in the whole space-time interval of interest and use a Worldwide Statistical Correlation (WSC) analysis through a superposed epoch approach to study the possible relation with the earthquakes. We find some clear concentrations of electron density and magnetic anomalies from more than two months to some days before the earthquake occurrences. Such anomaly clustering is, in general, statistically significant with respect to homogeneous random simulations, supporting a LAIC during the preparation phase of earthquakes. By investigating different earthquake magnitude ranges, not only do we confirm the well-known Rikitake empirical law between ionospheric anomaly precursor time and earthquake magnitude, but we also give more reliability to the seismic source origin for many of the identified anomalies.

A large earthquake comes after a long-term preparation phase composed of different stages of seismicity evolution driven by the continuous but variable tectonic stress[1,2]. The understanding of the underlying physical processes is likely to deliver the most reliable prediction method[3]. As it is practically impossible to follow this process at the level of the fault (typically at least tens of km depth), an alternative is to study if the lithosphere interacts with the above atmosphere and ionosphere, i.e. assuming a Lithosphere-Atmosphere-Ionosphere Coupling (LAIC[4–8]), during this long-term phase, but with particular attention to the very last stages. Co-seismic coupling in the atmosphere is well established[9], while the possible pre-earthquake coupling is more debated. A recent example is the possible ionospheric electron density enhancement before large earthquakes[10].

To explain the LAIC effects, different models have been proposed in the last years. Freund[5] proposed a mechanism based on the theory of *p-holes* (positive holes), which are produced by the stress along the fault. When p-holes reach the Earth's surface, they could ionize the atmosphere. These charged particles could create instability in the mesosphere and on the edge of the ionosphere. The mechanisms were tested successfully in laboratory[11]. An alternative mechanism is proposed by Pulinets and Ouzounov[6], based on gas and fluid that could rise up toward the surface in the preparatory phase of the earthquake. Another model was provided by Kuo *et al.*[12], which relies on a numerical simulation. It takes into consideration the role of the Earth's magnetic field, suggesting a possible mechanism of alteration of the ionosphere that improves their previous model[13].

[1]Istituto Nazionale di Geofisica e Vulcanologia, Via di Vigna Murata 605, Roma, 00143, Italy. [2]Now at School of Remote Sensing and Geomatics Engineering NUIST, Nanjing University of Information Science and Technology, Nanjing, China. [3]Now at Univ. Complutense de Madrid, Facultad CC. Físicas, Avd. Complutense, s/n – Madrid 28040, Spain & Geoscience Institute IGEO (CSIC – UCM), Madrid, 28040, Spain. [4]Planetek Italia srl, via Massaua 12, Bari, 70132, Italy. [5]Now at ASI, Via del Politecnico snc, Roma, 00133, Italy. [6]SpacEarth Technology, Via di Vigna Murata 605, Roma, 00143, Italy. [7]European Space Agency, ESTEC, Keplerlaan 1, NL-2201 AZ, Noordwijk, The Netherlands. *email: angelo.desantis@ingv.it

A third possible mechanism for the pre-earthquake electric field appearance is the possibility of modification of the electric field around the height of 100 km due to internal atmospheric gravity waves[14].

De Santis *et al.*[7], Pulinets and Boyarchuk[15] and Hayakawa[16] presented a general review about the processes that can occur in the atmosphere and ionosphere before and during an intense earthquake, and their possible correlations.

To detect the pre-earthquake ionospheric anomalies, various parameters can be monitored by ground-based equipment such as ionosondes[17–23], Global Navigation Satellite System (GNSS) receivers[24,25] and ULF magnetic field sensors[26–28].

Parrot[29] reviewed the most important results from the space investigations. The seminal satellite mission DEMETER[30] was specifically designed to possibly identify a wide range of electromagnetic pre-earthquake signals[31] and its statistical analyses were encouraging, pointing to LAIC above some reasonable level of randomness for 6.5 years of earthquakes[32–34].

A promising application of the geomagnetic field monitoring by the *Swarm* satellite mission to the 2015 Nepal earthquake (M7.8) showed a correlation between the magnetic anomalies and earthquakes temporal pattern[35]. A similar approach, applied to other earthquakes provided promising results[36–41].

Here we investigate the correlation of *in-situ* electron density and magnetic field anomalies from *Swarm* satellites with earthquakes. For this scope, a Worldwide Statistical Correlation (WSC) analysis based on a superposed epoch approach has been applied to *Swarm* data for the first time. This approach is applied in a time window around earthquakes that occurred during a period of four years and eight months since 1 January 2014.

Results

Worldwide statistical correlation analysis. We analyse the electron density (Ne) and magnetic field data from the three *Swarm* satellites to detect possible anomalies associated with the earthquakes from 1 January 2014 to 31 August 2018 (30 August for Ne). For the magnetic field anomalies we consider only the Y-East magnetic field component in the analysis (see Methods section for more details).

The worldwide earthquake data were extracted from the USGS (United States Geological Survey) catalogue (https://earthquake.usgs.gov), in terms of the time of occurrence, hypocenter location (geographical coordinates and depth) and magnitude. We selected the same time span of the satellite data (from 1 January 2014 to 31 August 2018) and declustered the catalogue to remove dependent earthquakes[42], in order to avoid bias in superposed epoch approach. For the purpose of this study, only earthquakes with the hypocentral depth less than 50 km are considered, since deeper earthquakes are less likely to affect the ionosphere[43]. The final dataset of 1312 M5.5+ worldwide shallow earthquakes was the base for the statistical correlation analysis with *Swarm* satellite data (see Methods section for more details).

Electron density and Y magnetic component signals from all the *Swarm* satellites have been analysed track by track by a moving window to provide two anomaly datasets according to a universal threshold k_t, one for each investigated quantity (see Methods section for algorithms description). Then we apply WSC to extract those anomalies (if any) associated in space and in time to the earthquakes and to obtain the superposed epoch diagrams (see Methods section for more details). Figures 1 and 2 show the correlation results when applied to the electron density by considering:

1. Anomaly threshold $k_t = 3.0$ within 1000 km from epicentres (bins of 2.4 days × 3 degrees).
2. Anomaly threshold $k_t = 3.0$ within Dobrovolsky radius[44] (bins of 2.4 days × 3.34 degrees).

Figures 3 and 4 show the correlation results when applied to the Y magnetic field data by considering:

3. Anomaly threshold $kt = 2.5$ within 1000 km from epicentres (bins of 2.4 days × 3 degrees).
4. Anomaly threshold $kt = 2.5$ within Dobrovolsky radius (bins of 2.4 days × 3.34 degrees).

Although our algorithm accepts any value of the threshold k_t, we applied a larger value ($k_t = 3.0$) for Ne than Y ($k_t = 2.5$), because the former quantity is more variable than the latter, producing usually more outliers.

Please note that Figs. 1 and 3 concern with analyses up to 1000 km from epicentres, however the diagrams extend the representation even after 1000 km (this explains the abrupt passage from colors to blue at 9°), although they do not have any physical meaning (in these cases, there are no anomaly data detected after 1000 km), only to maintain simple comparison with those of Figs. 2 and 4 that extend up to around 30°. From Figs. 1 to 4, the panels (a) include all possible anomaly-earthquake associations, i.e. anytime an anomaly falls inside the area and the time span investigated around the event a point is inserted. The advantage of this method (here also called Method 1) is to not make any hypothesis, but we know that it is extremely unlikely that an anomaly could be produced by two or even more seismic events at the same time and this case could appear too frequently when this method is applied. To overcome this unlikely situation, we propose also two other methods that are both plausible but introduce other assumptions: the first one (here also called Method 2) is shown in panels (b) where we associate the anomaly to the space-time closer earthquake by minimizing $Log_{10}(\Delta T \cdot R)$, being ΔT the time between anomaly occurrence and earthquake origin time, while R is the distance between the location of the anomaly and the epicentre. The second one (here also called Method 3) is shown in panels (c) and associates the anomaly to the largest magnitude event among all earthquakes compatible with that anomaly.

By looking at Figs. 1 and 2, large precursory concentrations of Ne anomalies fall few days (6–8 days) before the earthquakes, although some meaningful concentrations are also noticeable about 45 days and between 70 and 85 days before the events. We estimated the statistical significance of the correlation by means of two statistical parameters that indicate how much the maximum concentration is higher than a typical random maximum concentration (*d* parameter) and how many standard deviations σ the concentration is far from the simulated ones (*n*

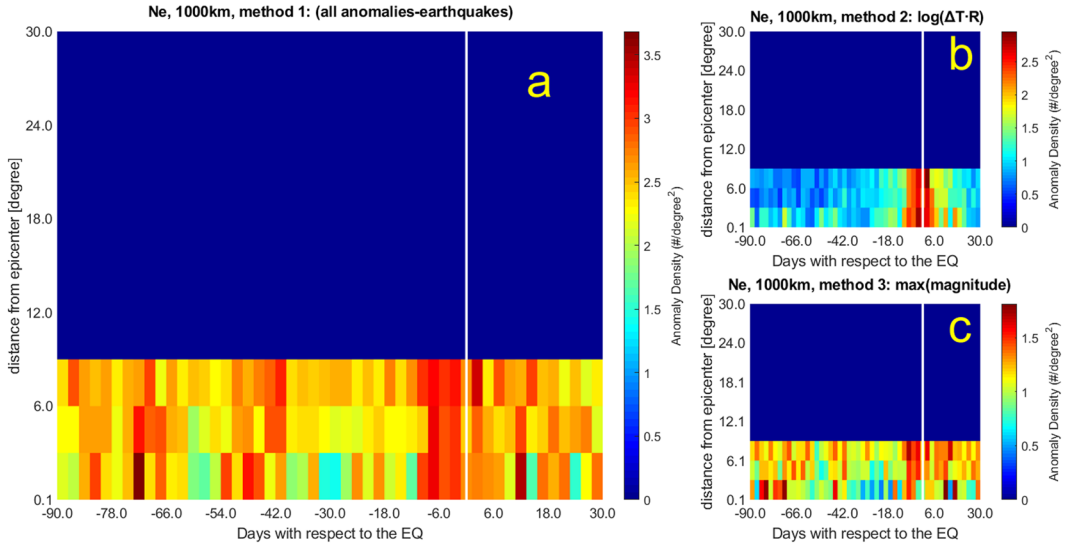

Figure 1. Worldwide Statistical Correlation (WSC) in terms of a superposed epoch approach applied to electron density Ne with threshold $k_t = 3.0$ considering a distance of 1000 km from earthquake (EQ) epicentre; *x*-axis presents the days before (negative days) or after (positive days) the EQ occurrence, while *y*-axis shows the distance from the earthquake epicentres in degrees. The analysis has been made for all hours (H24). (**a**) No constraints are imposed on anomaly-EQ association (Method 1). (**b**) Association EQ-Anomaly is made minimizing the value of $Log_{10}(\Delta T \cdot R)$, where ΔT is the precursor time and R the distance of the anomaly with respect to EQ epicentre (Method 2). (**c**) The same as (**b**) but assigning just the EQ with maximum magnitude for each anomaly (i.e. Method 3 or MaxM method). Most of the concentrations appear before and around the EQ occurrences. For the meaning of *d* and *n*, please refer to the main text. Please note the vertical extent of the bin is 3°.

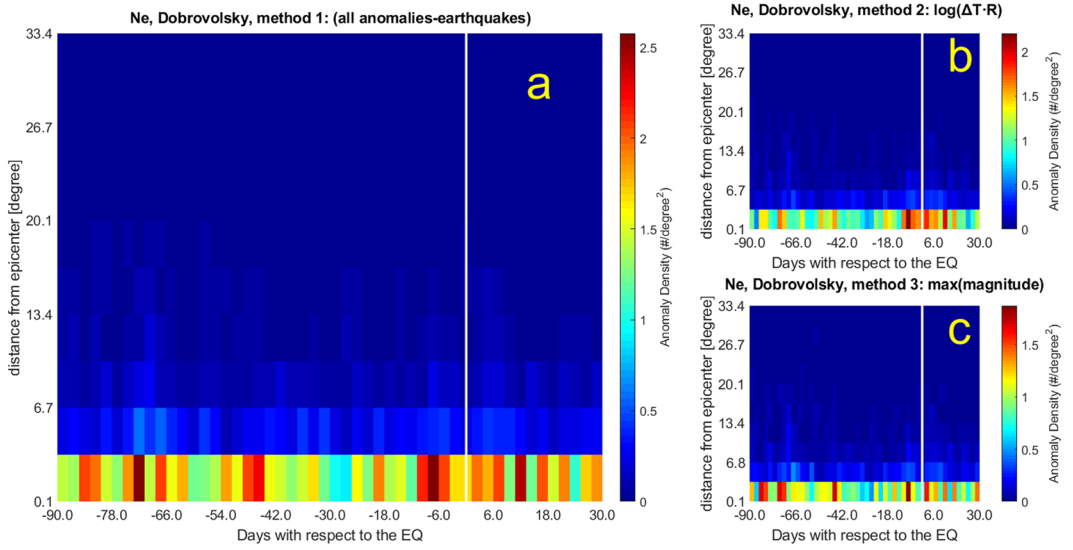

Figure 2. The same as Fig. 1 (Ne WSC analysis) but considering the Dobrovolsky area (DbA). Please note the vertical extent of the bin is 3.4°.

parameter) (for more details see the Methods). The statistical significance of the electron density anomalies is very low for the 1000 km analyses ($d = 1.0$–1.3 and $n = 0.3$–4.1), being comparable with typical random distributions of anomalies when Method 1 and 2 are applied, while is high for Dobrovolsky Area (DbA) analyses ($d = 1.5$–1.7 and $n = 4.6$–15.1). The 6–8 days anomaly concentration confirms previous results from DEMETER satellite[34]. The other longer precursory times had never been investigated so far and are the topic of the next section, where we will explain and justify this aspect in terms of the Rikitake empirical law[45]. It is encouraging that the methods that introduce some earthquake physical model and parameters such as Dobrovolsky strain radius as a limit of the spatial search (Fig. 2) and their maximum magnitude (Fig. 2c) show a higher statistical significance, giving empirical evidence for the seismic origin of most of these anomalies.

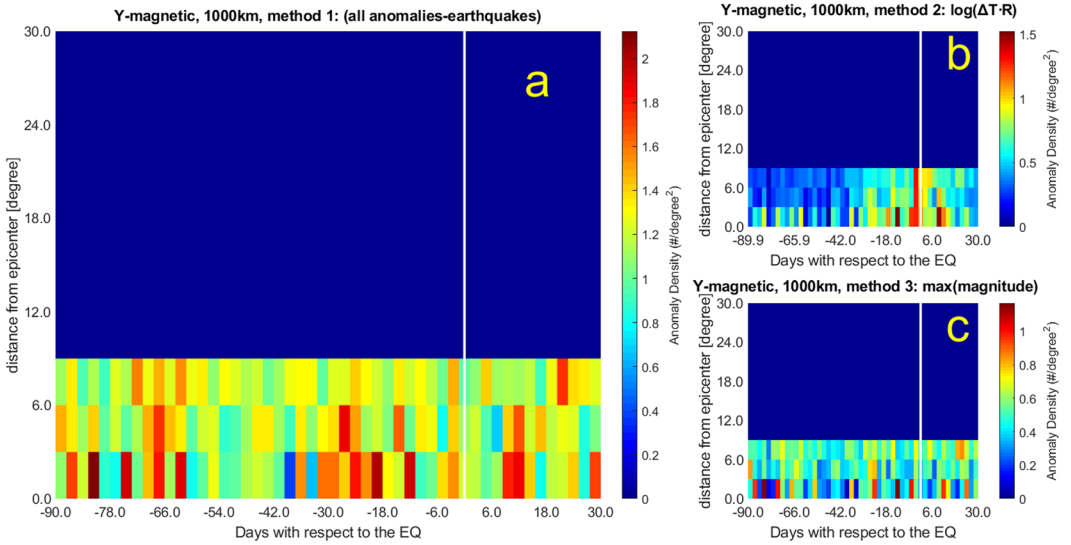

Figure 3. The same as Fig. 1 but for Y magnetic field component and $k_t = 2.5$. (**a**) Method 1; (**b**) Method 2; (**c**) Method 3.

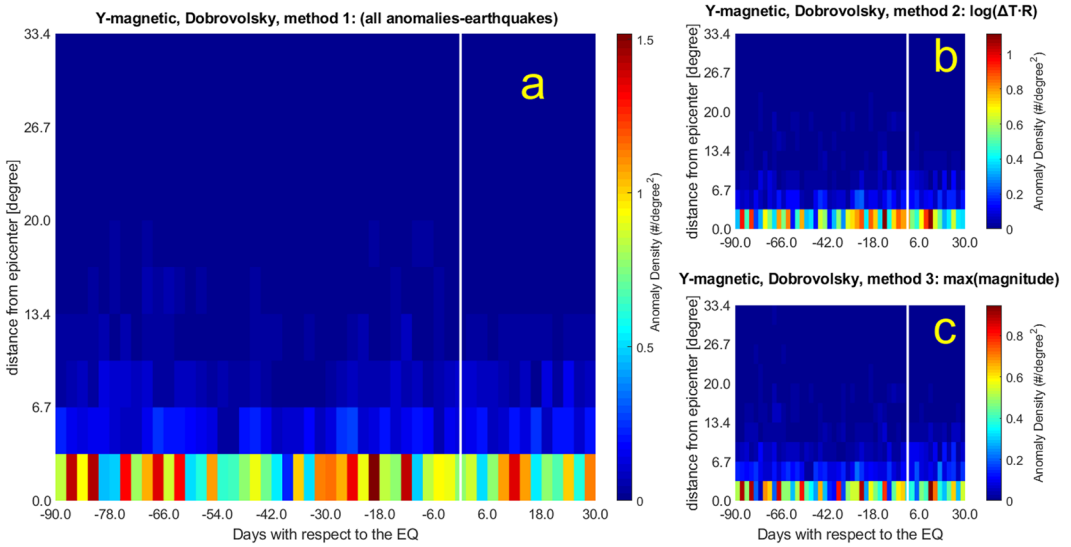

Figure 4. The same as Fig. 3 (Y magnetic field WSC analysis) but considering the Dobrovolsky Area (DbA).

We notice that in the analyses performed within a radius of 1000 km from epicentres (Fig. 1a–c) some unrealistic concentrations (although not the largest ones, which always fall at the closest band to epicentres) appear at farther distances. We can interpret these features as due to anomalies actually belonging to other closer earthquake epicenters, but included in the analyses, especially for smaller earthquake magnitudes. We suspect that this feature contributes to the low statistical significance of these kinds of analyses. However, this effect disappears when analysing the data according to the Dobrovolsky area (Fig. 2a–c), for which the distance of interest for smaller magnitude earthquakes is much smaller than 1000 km.

In Fig. 3b,c, and Fig. 4b the anomalies found in the Y magnetic field component analysis maximize around 12 days before the earthquake occurrences. Figure 3a,c (and Fig. 4a,c) show concentrations at even longer time intervals (about 80 days), the same period that we found for electron density anomalies. Figure 4a presents the largest concentration around 20 days before the earthquakes, a precursor time that appears also in other analyses, although with less significance.

The Y magnetic field component analyses show larger values of d and n ($d = 1.4$–2.1; $n = 6.0$–16.6) than Ne analyses ($d = 1.0$–1.7; $n = 0.3$–15.1).

The adoption of the Dobrovolsky strain radius slightly affects the main temporal features of the WSC analysis: although the anomaly density decreases (e.g., compare Fig. 2 with Fig. 1), the periods of higher density before

	Figure	Anomalies in the 120 day window	EQs with anomalies	Day of largest concentration	Anomalies in the max	EQs in the max	$[Dmax/D_0]_{real}$	*d*	*n*
Ne: $k_t = 3.0$ 1000 km Method 1	1a	32568	1170	−72, −7	126	40	1.1	1.0	1.7
Ne: $k_t = 3.0$ 1000 km, Method 2 log(ΔT·R)	1b	14846	992	+2*, −2	93	35	1.0	1.0	0.3
Ne: $k_t = 3.0$ 1000 km, Method 3 MaxM	1c	14846	888	−82, −72, −7*, +12*, +14*	63	23	0.7	1.3	**4.1**
Ne: $k_t = 3.0$ DbA Method 1	2a	7731	722	−72, −7	90	33	1.3	**1.5**	**8.7**
Ne: $k_t = 3.0$ DbA, Method 2 Log(ΔT·R)	2b	5958	611	−7	77	33	1.3	**1.5**	**4.6**
Ne: $k_t = 3.0$ DbA, Method 3 MaxM	2c	5958	495	−7	65	27	1.3	**1.7**	**15.1**
YMag: $k_t = 2.5$, 1000 km Method 1	3a	15747	1171	−82, −19, −12, +12	71	27	1.8	1.4	**7.5**
YMag: $k_t = 2.5$, 1000 km, Method 2 Log(ΔT·R)	3b	6605	857	−12, +10	53	19	1.8	**1.6**	**6.0**
YMag: $k_t = 2.5$, 1000 km, Method 3 MaxM	3c	6605	751	−82, −12	40	14	1.5	**2.0**	**10.3**
YMag: $k_t = 2.5$, DbA, Method 1	4a	3987	538	−19	53	24	2.8	**2.0**	**16.6**
YMag: $k_t = 2.5$, DbA, Method 2 Log(ΔT·R)	4b	2805	437	−12	39	12	2.5	**1.8**	**9.5**
YMag: $k_t = 2.5$, DbA, Method 3 MaxM	4c	2805	328	−86, −82, −24, +12	33	15	2.8	**2.1**	**15.8**

Table 1. Statistics for the real cases analysed in the paper in all space-time interval compared with the values of the random data analyses (Table S1). Ne/YMag at the lefter column indicate Ne/YMag real analysis. Day(s) of the largest concentration(s) (usually Brown colors; sometimes also Red in Figs. 1–4) of anomalies is(are) taken with respect to the earthquake (EQ) occurrence, where negative means before and positive means after it, with ±1.2 day uncertainty. For the analyses of Ne the anomalies in the whole space-time window were 58692, while for the Y magnetic field were 22142. For convenience to the reader, there is also the column of the corresponding Figure to which the results refer. Please note that *d* is actually estimated as the ratio of the $[D_{max}/D_0]_{real}$ with that $[D_{max}/D_0]_{rand}$ obtained from the mean of 100 simulations with the same exact number of anomalies, as shown in Table S1. *n* measures the significance of the $[D_{max}/D_0]_{real}$ with $[D_{max}/D_0]_{rand}$ as times of standard deviations (see main text). Bold numbers are those of the real cases that are significantly different than the random simulations in terms of $d \geq 1.5$ or $n \geq 4$. Four cases present both values as significant: all Y magnetic field component analyses in the DbA, and the Y magnetic field component analysis in 1000 km with MaxM, i.e. Method 3. *At the third and farthest band from epicentres.

earthquakes are confirmed. From the spatial point of view, anomalies cluster closer to the epicentres (i.e. always within the first spatial band).

Table 1 reports the main properties of the analyses performed over the real cases as well the results on their reliability, obtained by comparison with random distributions through the *d* and *n* parameters, whose values range from 1.0 to 2.1 and from 0.3 to 16.6, respectively. Bold numbers in *d* and *n* evidence the best cases for which the real analyses are well distinct from random simulations (selected as $d \geq 1.5$, because the density is equal to or larger than 50% of random distribution, or $n \geq 4$, because the probability to be random is equal to or less than 0.1%). Generally the *d* values increase when the Dobrovolsky area and the maximum earthquake magnitude criteria are considered (this is consistent with the expectation that larger earthquakes cause greater anomalies). The best results are reported when correlation is applied to the Y component of the magnetic field. Regarding the largest anomaly concentrations, some appear in almost all analyses, in particular 7, 12, 20 and 82 days before the earthquakes. Having enlarged the temporal window of analysis with respect to previous studies allowed us to detect also high precursor times such as 86 and 82 days before the earthquakes. They look significant and appear both in Ne and in Y.

In general, one method to select the association of the anomaly with the earthquake emphasises anomalies closer to earthquake occurrences (Log(ΔT·R), panel b), while another one tends to show also longer precursory times (earthquake magnitude, panel c). Applying all methods, however, we find signatures in electron density and Y magnetic field component anticipating the earthquakes, from a few days to around 80 days and the statistical correlation obtained makes this precursory feature compelling.

Rikitake law and its interpretation as result of a diffusion process. From what we carried out and summarized in Table 1, earthquake precursors would appear at different lead times, i.e. we would expect not only a single concentration but several concentrations at different times in advance before the earthquake occurrences, according to the range of earthquake magnitudes. A formula relating precursor time ΔT in days to magnitude M was proposed by Rikitake[45]: $\mathrm{Log}_{10}(\Delta T) = a + bM$. To deeper investigate this concept, we extended our analysis to 500 days before the earthquake occurrences, applying Method 1, i.e. without imposing any earthquake-anomaly association, in order to not favour closer or farther anomalies with respect to earthquake occurrences. We considered both the electron density and the Y-component of the magnetic field within the Dobrovolsky area and grouped the correlations for the following individual bands of earthquake magnitude: 5.5–5.9, 6.0–6.4, 6.5–6.9, 7–7.4, 7.5+. Of course, the choice of 500 days could be critical because for a large number of events (i.e. the ones occurred in the first 500 days of 4.7 years of investigated period) not all the time domain was covered by our analysis. On the other hand, this would allow us to look at longer potential precursor times.

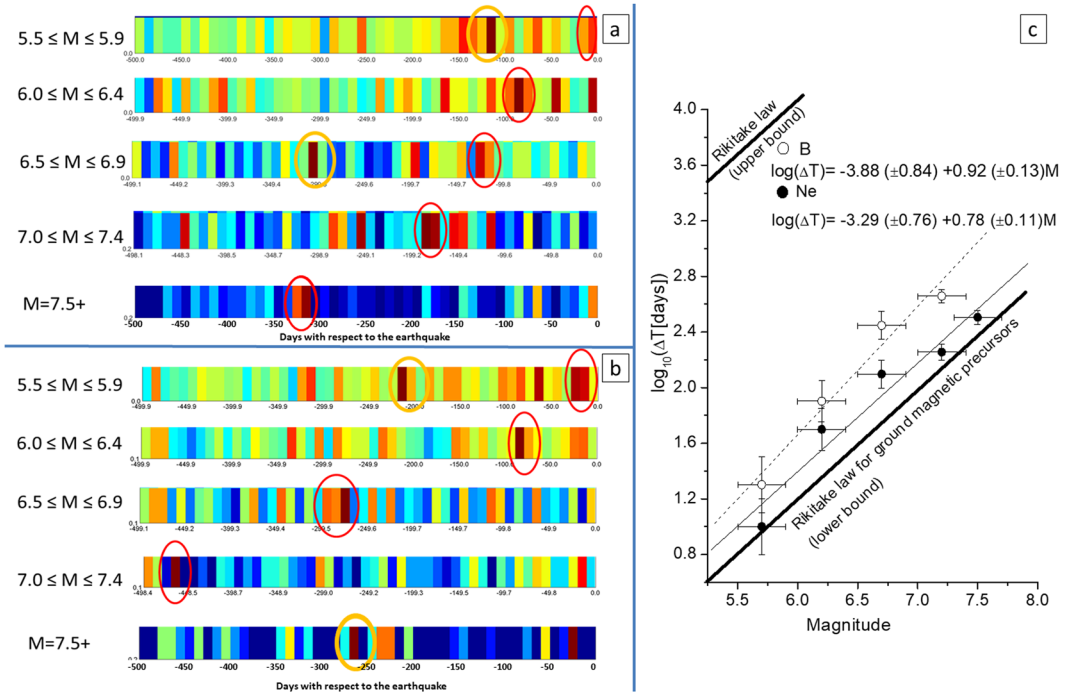

Figure 5. Worldwide Statistical Correlation (WSC) in terms of a superposed epoch approach applied to electron density with threshold $k_t = 3.0$ (**a**) or Y magnetic field with threshold $k_t = 2.5$ (**b**) considering the DbA around the EQ epicentre and different ranges of magnitude values. Please note that the investigated time interval is 500 days (versus 90 days before and 30 days after in the previous analyses) before the EQ occurrences and each temporal bin is of 10 days (versus 2.4 days of previous analyses). Only the closest spatial band to the EQ epicentre is shown; for convenience colour palettes are not shown, although blue stands for the lowest density (close to zero) and brown for the largest density (that differs from case to case). Red ovals indicate the larger concentrations considered for the Rikitake law; yellow ovals are not taken into account for the reason given in the main text. (**c**) shows the Rikitake law for electron density Ne (black circles and thin fitting solid line) and Y magnetic field (empty circles and thin fitting dash line). Also the corresponding *a* and *b* coefficients are given, together with the upper and lower bounds of the Rikitake law for ground magnetic precursors[45].

Figures 5a,b show the WSC results, for Ne and Y component of the magnetic field, respectively (now every single bin is 10 days × 3.34 degrees large). At a first glance, the identification of the largest group of anomalies (red ovals), taken as considering two adjacent bins of these new diagrams, is straightforward in all magnitude intervals with a few exceptions (yellow ovals). Among them, however, some can be easily excluded: the yellow ovals in the middle panel of Fig. 5a and in the top panel of Fig. 5b are actually two-bin combinations less significant than the corresponding red ovals. In addition, for the top panel of Fig. 5a, we exclude the yellow oval because is too distant from earthquake occurrence, giving more credit to the closer concentration (red oval). The results for M7.5+ are not sufficiently robust, because the number of earthquakes is rather small (16) in the 4.7 years of the study. However, to test the Rikitake law[45], we included this largest range of magnitude for the electron density. We fit the same Rikitake functional law to our precursor times with respect to the central value of magnitude for each band. We estimated the error bars for the magnitude as the half width of the investigated range and for the time interval as the bin span of the anomalies concentration. Figure 5c shows the results for both Ne (black circles and thin fitting solid line) and Y (empty circles and thin fitting dash line), together with lower and upper bounds of the Rikitake law for magnetic ground precursors[45] (thick lower and upper lines). It is surprising that, within the estimated errors, we find similar *a*,*b* values ($a = -3.29 \pm 0.76$, $b = 0.78 \pm 0.11$ for Ne and $a = -3.88 \pm 0.84$, $b = 0.92 \pm 0.13$ for Y) to those proposed for ground magnetic observations by Rikitake[45] (see Methods section).

Apparently the two fitting lines for Ne and Y are distinct, but both fits are within the errors. In addition, for both quantities, it appears that earthquake precursors occur within a day for events with magnitude below 4.2, although is it very unlikely that these weaker earthquakes could produce an effect in the ionosphere[20].

On the other hand, the greater the earthquake magnitude, the greater the difference between the ΔT referred to Ne and Y-component: for instance, for M7.5, the Ne relation provides $\Delta T = 363$ days, while Y relation gives ΔT around 1000 days. This could explain why we do not find a statistical significance in the M7.5+ analysis for Y magnetic component.

This result strongly supports the empirical law found by Rikitake[45] for ground magnetic observations, even extended it to electron density and magnetic field satellite data, with a little adjustment of the coefficient values.

The Rikitake law is reasonable for the process of earthquake generation and coupling with the above atmosphere and ionosphere layers with simple arguments (more details are shown in Methods). Assuming a lithospheric process of stress diffusion[46] across the Dobrovolsky strain radius R_{Db}[44], we obtain the relationships

$a = -\mathrm{Log}(4\pi D)$ and $b = 2\beta$, D is the coefficient of diffusion and β is the Dobrovolsky exponent: 0.43 (see Methods for all the passages). We can verify them by comparing the b value obtained from Rikitake (around 0.8) that, within the error, resembles the value of 0.86 deduced from Eq. 7b in Methods. From the value of a, we can even estimate D. Although a value has large uncertainty, i.e. $a \cong -2$ (Rikitake), $a \cong -3.3$ and $a \cong -3.9$ (in our analysis of Ne and Y, respectively), we can take the central value of $a \cong -3$, obtaining $D \cong 100\ \mathrm{m}^2/\mathrm{s}$, which is one-two order more than a reasonable value for the crust[1]. However, it is really interesting that this same order of diffusivity can be found for slow earthquakes when a diffusion model is considered[47]. This interesting coincidence would merit more future attention, potentially opening new perspectives in seismological studies.

Conclusions

The electron density and magnetic field WSC analyses applied to about 4.7 years of *Swarm* satellite observations highlight that anomalies appear to occur before the earthquake occurrences, between a few days and 80 days before the earthquakes, with larger peaks at around 10, 20 and 80 days. We find that in all analysed cases considering the DbA, the largest concentration of pre-earthquake anomalies is statistically significant by a factor up to around 2 (i.e. $d \sim 2$) times the simulated data, with up to 15–17 σ (i.e. $n = 15$–17). We note that the detected anomalies seem better correlated with earthquakes of stronger magnitude.

We confirm linear relation between the $\mathrm{Log}\Delta T$ and magnitude, and the found a, b coefficients are, within the estimated errors, close to those proposed by Rikitake[45]. We also provide a simple explanation of this relationship and show that the empirical expressions we found for satellite data anomalies are consistent with a stress diffusion process in the crust as that producing slow earthquakes.

The Rikitake law, confirmed by the separate analyses of Fig. 5a,b at different ranges of magnitude, supports the argument that the precursor times are related to the earthquake magnitude. Its expected effect would be to theoretically smear out eventual peaks in the analyses of all magnitude earthquakes, what we do not actually find in Figs. 1–4. However, our results are not in contradiction for two main reasons: i) The analysis limited to 90 days before and 30 days after earthquake occurrence is heavily influenced by the preponderance of low magnitude earthquakes, so concentrations are more confined within the closest times before earthquakes, while the longer time precursors, likely produced by larger earthquakes, are out of the analysed temporal interval. ii) The analyses reported in Fig. 5 are extended to 500 days before, to include longer precursor times, typical of larger magnitude earthquakes tend to appear well in advance with respect to earthquake occurrences. However, the law is an empirical law which is not "exclusive", so an earthquake could even provide other precursors in different time.

Although this investigation would support the LAIC with clear statistical significance, another clear message emerges: not all earthquakes are in the favourable conditions to produce significant effects in the ionosphere. Only a portion of them (we estimate something around 40%; see section of Methods) generates a non-negligible electromagnetic effect that cannot be due to simple chance. Several causes can be attributed to this deficiency: insufficient satellite passes available, an inappropriate coversphere (e.g. vegetation), adverse meteorological conditions, and/or still not perfect anomaly detection strategy.

More detailed analyses, as the study of the type of earthquakes analysed, according to their occurrence in subduction zones or along strike-slip faults, in the land or under the sea, in interplate or intraplate, and the inspection of single anomalies, would help to better understand the physics behind the possible coupling phenomena. In this respect, a prolongation of the *Swarm* satellite mission is greatly encouraged: for example, with at least 10 years of data, longer precursor times could be investigated without loss of statistical significance. Data from other quasi-polar satellites, equipped with magnetometers and Langmuir probes (e.g. the Chinese seismo-electromagnetic satellite[48]), would also be useful for this scope.

A final point is clearly important here: since the ionospheric anomalies are causally related to what happens inside the Earth and at the ground-to-air interface, the corresponding parameters should be, or even must be, included in any further study. This is implicit in the Geosystemics concept[8], by which we can consider the Earth system as an ensemble of cross-interacting parts. Therefore, it is mandatory to consider a multiparametric point of view to address this kind of complex phenomena, by combining seismological, atmospheric and ionospheric information[8,40].

Methods

Satellite data. *Swarm* mission is an ESA satellite mission[49] composed of three identical quasi-polar orbiting satellites, two (Alpha and Charlie satellites, also named as *Swarm*-A and *Swarm*-C, respectively) at lower orbit (around 460 km above the Earth's surface) and the third (Bravo or *Swarm*-B) at the highest orbit (around 510 km). The satellites were placed in orbit on 22 November 2013 and are still orbiting around the Earth. The original configuration with *Swarm*-A and *Swarm*-B flying in parallel and *Swarm*-C in a higher orbit[49] was changed to the present one because of early problems (from 5 November 2014) in the scalar magnetometer of *Swarm*-C.

The satellite payloads comprise, among others, a Langmuir probe (LP) and two magnetometers, i.e. a vector fluxgate magnetometer (VFM) and an absolute scalar magnetometer (ASM). These sensors have been here analysed systematically to detect possible pre-earthquake Lithosphere-Atmosphere-Ionosphere Coupling (LAIC) electron density and magnetic field anomalies from space.

The Ne data used in this work are measured by the LP of *Swarm* satellites with a sampling rate of 2 Hz. The input data have been provided by the original *Swarm* Advanced product called "2_Hz_Langmuir_Probe_Extended_Dataset". This dataset is provided in Common Data Format (CDF) and freely available in the ESA *Swarm* FTP and HTTP Server swarm-diss.eo.esa.int (the *Swarm* data are also available from VIRES web platform: http://vires.services). The current release of 2 Hz Langmuir Probe Extended Dataset (Release 101) is the ESA reprocessing of all *Swarm* Electric Field Instrument data from the beginning of the mission to 30 August 2018.

According to ESA, the current values of electron density are up to a few 10% too high at low density (https://earth.esa.int/web/guest/missions/esa-eo-missions/swarm/data-handbook/preliminary-level-1b-plasma-dataset). This is not an issue for the purposes of our anomaly detection, as it is not based on the absolute value itself, but its derivative as reported later in the text.

We also considered scalar intensity (F) and vector X,Y,Z magnetic components. The data are at 1 Hz sampling that correspond to the low resolution magnetic data contained in the Level 1b (L1b) products. All the L1b magnetic data are provided by ESA in Common Data Format (CDF) and hosted in the ESA *Swarm* server.

In order to select data without evident troubles/problems during the satellite flying (https://earth.esa.int/web/guest/swarm/data-access/quality-of-swarm-l1b-l2cat2-products), we took into account the quality flags associated with both the electron density and magnetic field data.

In detail, we extracted different information from original CDF files, including the type of satellite, i.e. A for Alpha, B for Bravo, and C per Charlie, the UTC time, data quality flags, the electron density or the vector magnetic components in NEC (North, East, Centre) reference frame by the VFM instrument and the magnetic absolute intensity by ASM instrument (for A, B and C satellites; however, as ASM of C after 5 Nov. 2014 is out of work, the total intensity is calculated from the Cartesian magnetic components given by VFM instruments).

The error of the magnetic field measured by *Swarm* satellites can be estimated to be less than 0.3 nT, with a typical value of 0.1 nT[50].

Algorithms for electromagnetic anomaly detection. The approach to identify anomalies is based on two novel algorithms, i.e. *NeAD (Electron Density Anomaly Detection)* and *MASS* (*MAgnetic Swarm anomaly detection by Spline analysis*), applied to the electron density Ne (2 Hz sampling) and magnetic field (components and total intensity-1Hz sampling) from *Swarm* satellites (A,B,C), respectively. These algorithms share the main features that we highlight below.

For each day and for all the satellites tracks (the daily number of semi-orbit for each satellite is about 32), the Local Time (LT) and the geomagnetic latitudes are evaluated, the latter based on a tilted geocentric dipole field from the last generation of the IGRF (International Geomagnetic Reference Field) global model of the geomagnetic field (IGRF-12[51]). Then, the first time derivatives of Ne and of the magnetic field are estimated as the first difference values divided by the time interval between two consecutive samples. Finally, a fit with cubic splines is applied to remove the long term trend.

Figures S1, S2 show an example of the output from *NeAD* and *MASS*, respectively, carried out for two different epochs and for *Swarm* C: April 27, 2015 (two days after the M7.8 Nepal earthquake occurred on 25 April 2015) and February 14, 2016 (almost two weeks before the M7.8 Sumatra earthquake occurred on 2 March, 2016). The track number, descending (D)/ascending (U), the corresponding local time (LT) and UTC, the geospace conditions given by the Dst and a_p geomagnetic indices, areprovided. The geographical area of interest with satellite track (red), the Dobrovolsky area (yellow oval; circular on the terrestrial sphere) and the earthquake epicentre (green star) are also shown. It is worth noticing that, from Figure S2, an anomalous signal is visible especially in the East magnetic component (Y), while the total intensity does not show appreciable variability[39]. This could be simply explained by field aligned current processes that do not practically affect the total intensity of the magnetic field vector, but only its direction[35]. Accordingly, instead of analysing the whole magnetic field, we focused only on the magnetic Y component because it is less affected by external perturbations than X and Z components[52] and this increases the possibility to detect Earth internal source anomalies.

To detect anomalies of interest for the WSC analysis, *NeAD* and *MASS* outputs (for the entire *Swarm* data set) are further analysed by overlapping sliding windows within $\pm 50°$ geomagnetic latitude, to limit the effects due to the high latitude ionosphere, and under quiet magnetic conditions in terms of Dst and a_p indices ($|Dst| \leq 20$ nT, $a_p \leq 10$ nT) to limit the effects of perturbations coming from the outer space.

We consider overlapping sliding windows of 7.0° latitude length, moving by 1.4° (1/5 of window length) along the whole $\pm 50°$ geomagnetic latitude range. Since the satellite speed is of about 7.6 km/s, the choice of the 7.0° sliding window allows us to include typical pre-earthquake satellite signals of some tens of seconds into a sufficiently short spatial length[34,53]. The approach with overlapping sliding windows provides an output matrix in which each row identifies a given window and each column contains the following quantities: the date and central time (UTC and LT) of the given window, the satellite (A,B,C), the track number, Dst, a_p, the root mean square error (rms) over the samples distribution within the given window and the frequency content of the window (the latter not used in this work), together with the root mean square error (RMS) over the whole track in $\pm 50°$ geomagnetic latitude.

Finally, from the output matrix, we define as anomalous those windows (i.e. the Ne and Y magnetic field component values within them) for which $rms > k_t \cdot RMS$, where k_t is an appropriate threshold (normally 2.5–3) and RMS is the root mean square error computed for the whole track.

Summarizing, criteria adopted by *NeAD* and *MASS* to detect anomalies are:

- *Swarm* tracks within $\pm 50°$ geomagnetic latitude;
- Low magnetic activity: $|Dst| \leq 20$ nT, $a_p \leq 10$ nT during the track acquisition time;
- sliding windows of 7.0° latitude length, moving by 1.4° along the tracks;
- rms (of each sliding window) $> k_t \cdot RMS$ (evaluated along the track).

Worldwide statistical correlation algorithm. The WSC algorithm evaluates the possible correlation in space and time of the detected anomalies by *NeAD* and *MASS* with the earthquake locations and occurrences. The earthquake catalogue was declustered first by extracting all M5+ earthquakes, then detecting and removing the dependent earthquakes, i.e. those earthquakes with magnitude $M \leq M_{ms} - 1$ (M_{ms} is the mainshock magnitude) that happen inside 10 km from the mainshock epicenter and a 10-day time window from its origin time. In the declustered catalogue, the magnitude of the mainshock is replaced by the equivalent magnitude of the seismic

cluster. We then selected those shallow earthquakes with $M \geq 5.5$ for which LAIC signatures are more likely to be captured as highlighted by Liu *et al.*[20] who found a dramatic enhancement in the statistical correlation between ionospheric anomalies and earthquakes with magnitude greater than 5.4. In addition, this choice avoids problems of catalogue incompleteness[54].

WSC cumulates all the anomalies of the same family (Ne or Y magnetic field component) associated with each earthquake (occurring in the time interval normally ranging between 90 days before and 30 days after the earthquakes; but we also extended the time interval up to 500 days before earthquakes to verify Rikitake law; see next dedicated section) in a unique space-time graph by a superposed epoch approach having as common origin the occurrence time and the epicentre of all investigated earthquakes along the available *Swarm* mission data (4.7 years). The horizontal axis of the WSC diagrams is the time lag between the anomalies and the seismic events and the vertical axis is the distance of the anomalies with respect to the epicentre (in degrees). The common time origin is represented by the white vertical line. The colour bar identifies the density level of the anomalies (number of anomalies for squared degree). A simplified flowchart of the WSC algorithm is shown in Figure S3. This method is similar to that one applied to DEMETER satellite data analysis[32–34], apart from the use of a wider time window around the earthquakes (in Yan *et al.*[34], for example, it was −15 to 5 days; here we normally considered −90 to 30 days). We considered a longer time window according to the empirical relationship given by Rikitake[45]: for a typical M5.5 earthquake, which is the most frequent in our dataset, we would expect a precursor at a mean advance time of 16 days, in a range from 2 to 144 days (see also Piscini *et al.*[55]). Therefore, extending the analysis to 90 days before the earthquake occurrence, seems to be a good compromise, avoiding border effects in time. In space, we consider either an area comprised by a fixed radius of 1000 km around the earthquake epicentre[34] or the most popular Dobrovolsky's circular area (DbA) around the earthquake epicentre, whose radius R_{Db} in km scales with magnitude M, i.e. $R_{Db} = 10^{0.43M}$, as suggested by Dobrovolsky *et al.*[44]. For our selected earthquakes, the radius of this area is between 230 km or 2.2° (M5.5) and 3700 km or 33.4° (M8.3). The DbA is considered a good empirical approximation of the preparation area of an impending earthquake[56].

In addition to the adopted spatial (anomalies within 1000 km and/or within the DbA from the epicentres) and temporal (anomalies occurring from −90 days to 30 days around the earthquake occurrences) criteria, we present the analysis in three different ways.

The first method (Method 1) does not take into account any assumption, associating each anomaly to all earthquakes that fall inside the analysed space time. In the next two methods, we introduce some limitations to prevent an anomaly from being associated to more than one earthquake, which is very unlikely to happen. This can be done by:

Method 2: Referring a given anomaly to that earthquake for which $\mathrm{Log}_{10}(\Delta T \cdot R)$ is minimum, where ΔT is the time lag between the anomaly occurrence and the earthquake (we also call it precursor time), and R is the spatial distance of the anomaly from the earthquake epicentre. This method intends to assign to the anomaly the closest earthquake in space and time. This limitation takes also into account the correlation found between $\mathrm{Log}_{10}(\Delta T \cdot R)$ and the earthquake magnitude M when ionosphere anomalies from HF ionosondes are considered[18,19,22,23].

Method 3: Referring a given anomaly to that earthquake with the greatest magnitude M (also referred as MaxM method), falling inside the analysed space-time window.

The Method 1 has the advantage to not impose any further constraints on the anomalies, but has the disadvantage to have eventually some anomalies with more than one associated earthquake.

We would underline that the selection of a particular method affects only a small percentage of the whole cases. So, all the methods have a common anomaly-earthquake association.

Therefore, we provided space-time distributions, one for each earthquake, of the anomalies (Ne and/or Y-magnetic field component) associated with it. Then we superposed all the distributions imposing a common origin that identifies the earthquake occurrence times and the epicentres. The resulting WSC distribution (one for each parameter, Ne and/or Y magnetic field component) contains all the anomalies overlapped. The density level of the anomalies (number of anomalies per squared degree) is estimated in 50 temporal bins and 10 spatial bins, so each bin of the diagram usually covers 2.4 days (120 days divided by 50 bins). The epicentral distance (vertical extent) of each bin is of 3°, i.e. about 330 km at the Earth's surface for the 1000 km analyses (or 3.34°, i.e. about 370 km at the Earth's surface, for the DbA analyses), up to 30° (33.4° for the DbA analyses, corresponding to the largest DbA for the largest magnitude M8.3 in the earthquake dataset). The small difference in the two full-scales is due to the different height of the bins in the two kinds of analysis. In the 1000 km analyses, it allows to complete the whole distance with three full bands, but almost preserving the possibility to compare these analyses with those made across the DbA. In any case, to maintain perfect agreement in all (1000 km and DbA) analyses the anomalies and earthquakes have been counted always in a bin of 3.34°.

The statistical significance of the WSC analysis results is based on the introduction of quality statistical quantities as follows.

To estimate how much reliable is the largest concentration of anomalies, we firstly considered the ratio between the largest concentration of the real anomalies D_{MAX} and that of a theoretical uniform distribution (in space and time) D_0 of anomalies, i.e. D_{MAX}/D_0.

D_0 can be analytically defined as:

$$D_0 = \frac{N_{an}}{A \cdot \Delta t} \cdot N_{eq} \quad (1)$$

where N_{an} is the total number of anomalies in the whole analysed region and in all times; A is the whole area of the analysis in square degrees (in this case it is the area of a tesseral zone between −50° and + 50° of geomagnetic latitude); Δt is the analysed time in days, in this study it is 1703 days, i.e. 4.7 years. N_{eq} is the number of earthquakes associated with at least one anomaly. Thus, the units of D_0 are (square degrees × days)$^{-1}$.

D_{MAX} is calculated as:

$$D_{MAX} = \frac{N_{exan}}{A_{BIN} \cdot \Delta t_{BIN}} \quad (2)$$

N_{exan} is the number of anomalies associated with earthquakes in the bin of the first row (i.e. the anomalies closest to the epicentre) with the largest concentration of anomalies; A_{BIN} is the area of the bin (i.e. the area of the circle or of the annulus region of the first bin around the epicentre); Δt_{BIN} is the time width of the bin in the same unit of Δt (2.4 days if we investigate a window from 90 days before to 30 days after the earthquake occurrence).

Note, however, that D_{MAX}/D_0 is biased because the areas associated with the earthquakes could overlap, either in case of considering circles of 1000 km around the epicentres or the effective DbA. In addition, we do not analyse all the temporal periods but only those with low magnetic disturbance (i.e. $|Dst| \leq 20$ nT, $a_p \leq 10$ nT), to roughly "filter out" those anomalies clearly depending on solar geomagnetic activity.

Then, to establish the actual statistical significance of D_{MAX}/D_0, we compare it with its analogous obtained by correlating the real earthquake dataset with a certain number (usually 100) of random distributions of anomalies (with same number of the real cases), almost homogeneous in space and time. The random anomalies are generated assigning to each of them a latitude, a longitude and an occurrence time. The latitude and longitude are selected (with homogeneous probability in space) within the analysed global area (i.e. the area with |geom. latitude| $\leq$50°). The occurrence time is selected among the geomagnetic quiet times with uniform probability. From the random simulations, we also calculate the average and the standard deviation σ_{rand} of the parameter $[D_{MAX}/D_0]_{rand}$, to be further compared with that one corresponding to $[D_{MAX}/D_0]_{real}$ for the real cases.

Table S1 summarizes the main features of the random simulations, each of them referring to the different criteria adopted in the WSC real cases. For each series of 100 random simulations, we provide also the standard deviation σ_{rand}.

Then we consider the statistical parameter d defined as the ratio between $[D_{MAX}/D_0]_{real}$ (Table 1), estimated over the real anomaly data, and $[D_{MAX}/D_0]_{rand}$, estimated over a set of simulated random anomaly data (Table S1). That is:

$$d = \frac{[D_{MAX}/D_0]\text{real}}{[D_{MAX}/D_0]\text{rand}}. \quad (3)$$

In this way, d would show how much the real maximum concentration is above the expected typical maximum concentration of a random anomaly distribution: the larger is the d value, the more the results of the WSC applied to real data deviate from randomness.

Finally, to increase the WSC reliability, we provide also the parameter n measuring the significance of the real statistical results with respect to the random distributions, defined as: $n = ([D_{max}/D_0]_{real} - [D_{max}/D_0]_{rand})/\sigma_{rand}$. Also in this case, the larger n, the more significant the corresponding real analysis.

Fraction of earthquakes with ionospheric effects. We can provide a rough estimate of the fraction of earthquakes that produce ionospheric effect in two ways. A way is based on the best cases of Table 1: this estimate is given by the ratio between the earthquakes with anomalies (third column) and the total number of earthquakes, i.e. 1312. Another way is based on the separate analyses of Fig. 5a,b: we can count the number of earthquakes in the largest concentrations that contribute to the Rikitake law. Both estimates point to values between 25% and 55%. Therefore, the given value of 40% is a reasonable estimation.

Rikitake law. We recall the empirical law by Rikitake[45], that relates precursor time ΔT with the earthquake magnitude M:

$$\text{Log}_{10}(\Delta T) = a + bM \quad (4)$$

where $a = -2.08$ ($\pm$1.43) and $b = 0.78$ ($\pm$0.23), for geomagnetic field ground observations[45].

Although out of our scope, we sketch some simple reasoning on why the Rikitake law is reasonable for the process of earthquake generation and coupling with the above atmosphere and ionosphere layers. Adopting a lithospheric process of stress diffusion[46] across the DbA, we can relate the spatial distance R (in km) of the anomaly from the earthquake epicentre with the time ΔT:

$$R = \sqrt{4\pi D \Delta T} \quad (5)$$

where D is the diffusivity. If we suppose that the first precursor can appear at the beginning of the stress evolution, then ΔT will be the precursor time.

According to Dobrovolsky *et al.*[44] we can express R_{Db}, as:

$$\text{Log}R_{Db} = \beta M \quad (6)$$

with $\beta = 0.43$ and M the earthquake magnitude.

If we assume $R = R_{Db}$, we can replace R_{Db} in (6) with R of the Eq. (5), so that the coefficients in Eq. (4) become:

$$a = -\text{Log}(4\pi D) \quad (7a)$$

and

$$b = 2\beta \tag{7b}$$

From our results we could even deduce D from (7a) and verify the relationship (7b) (see Section before Conclusions).

Dedication. We would like to make a special dedication to the memory of Eigil Friis-Christensen (1944–2018), lead investigator of the *Swarm* satellite mission. Without him probably nothing of all published works about *Swarm* mission could ever have been written.

Received: 10 July 2019; Accepted: 25 November 2019;
Published online: 30 December 2019

References

1. Scholz, C. H. *The Mechanics of Earthquake and Faulting* (ed. Cambridge Univ. Press) vol. xxiv., 471 (Cambridge/New York, 2002).
2. Olaiz, A. J. *et al*. European continuous active tectonic strain–stress map. *Tectonophysics* **474**, 33–40 (2009).
3. Kanamori, H. Earthquake prediction: an overview in *International Handbook of Earthquake and Engineering* Seismology (ed. Academic Press) 1205–1216 (Amsterdam, 2003).
4. Hayakawa, M. & Molchanov, O. A. *Seismo Electromagnetics Lithosphere-Atmosphere-Ionosphere Coupling* (ed. TERRAPUB) 477 (Tokyo, 2002).
5. Freund, F. Pre-earthquake signals: Underlying physical processes. *Journal of Asian Earth Sciences* 383–400 (2011).
6. Pulinets, S. & Ouzounov, D. Lithosphere-Atmosphere- ionosphere coupling (LAIC) model-an unified concept for earthquake precursors validation. *J. Asian Earth Sci.* **41**(4–5), 371–382 (2011).
7. De Santis, A. *et al*. Geospace perturbations induced by the Earth: the state of the art and future trends. *Phys. & Chem. Earth* **85-86**, 17–33 (2015).
8. De Santis, A. *et al*. Geosystemics View of Earthquakes. *Entropy* **21**, 412, https://doi.org/10.3390/e21040412 (2019).
9. Tanimoto, T., Heki, K. & Artru-Lambin, J. Interaction of Solid Earth, Atmosphere, and Ionosphere in Gerald Schubert (editor-in-chief) *Treatise on* Geophysics, 2nd *edition* (ed. Gerald Schubert), vol. 4, 421–443 (Oxford: Elsevier, 2015).
10. He, L. & Heki, K. Ionospheric anomalies immediately before Mw7.0– 8.0 earthquakes. *J. Geophys. Res. Space Phys.* **122**, 8659–8678, https://doi.org/10.1002/2017JA024012 (2017).
11. Freund, F. T. *et al*. Stimulated infrared emission from rocks: assessing a stress indicator. *eEarth* **2**, 1–10 (2007).
12. Kuo, C. L., Huba, J. D., Joyce, G. & Lee, L. C. Ionosphere plasma bubbles and density variations induced by pre-earthquake rock currents and associated surface charges. *J. Geophys. Res.* **116**, A10317 (2011).
13. Kuo, C. L., Lee, L. C. & Huba, J. D. An improved coupling model for the lithosphere–atmosphere–ionosphere system. *J. Geophys. Res. Space Phys.* **119**, 3189–3205 (2014).
14. Yang, S. S., Asano, T. & Hayakawa, M. Abnormal gravity wave activity in the stratosphere prior to the 2016 Kumamoto earthquakes. *J. Geophys. Res. Space Phys.* **124**, https://doi.org/10.1029/2018JA026002 (2019).
15. Pulinets, S. & Boyarchuk, K. *Ionospheric* Precursors *of Earthquakes* (ed. Springer) (Berlin, 2004).
16. Hayakawa, M. *Earthquake prediction with radio techniques* (ed. Wiley, J. & Sons) 294 (Singapore, 2015).
17. Ondoh, T. & Hayakawa, M. Synthetic study of precursory phenomena of the M7.2 Hyogo-ken Nanbu earthquake. *Phys. Chem. Earth* **31**, 378–388 (2006).
18. Korsunova, L. P. & Khegai, V. V. Medium-term ionospheric precursors to strong earthquakes. *Int. J. Geomagn. Aeron.* **6**, GI3005, https://doi.org/10.1029/2005GI000122 (2006).
19. Korsunova, L. P. & Khegai, V. V. Analysis of seismo-ionospheric disturbances at the chain of Japanese stations for vertical sounding of the ionosphere. *Geomagn. and Aeronom.* **48**, 392–399 (2008).
20. Liu, J. Y., Chen, Y. I., Chuo, Y. J. & Chen, C. S. A statistical investigation of pre-earthquake ionospheric anomaly. *J. Geophys. Res.* **111**, A05304, https://doi.org/10.1029/2005JA011333 (2006).
21. Xu, T., Hu, Y. L., Wang, F. F., Chen, Z. & Wu, J. Is there any difference in local time variation in ionospheric F2 layer disturbances between earthquake induced and Q- disturbances events? *Ann. Geophysicae.* **33**, 687–695 (2015).
22. Perrone, L., Korsunova, L. & Mikhailov, A. Ionospheric precursors for crustal earthquakes in Italy. *Ann. Geophysicae* **28**, 941–950 (2010).
23. Perrone, L. *et al*. Ionospheric anomalies detected by ionosonde and possibly related to crustal earthquakes in Greece. *Ann. Geophysicae* **36**, 361–371, https://doi.org/10.5194/angeo-36-361-2018 (2018).
24. Dautermann, T., Calais, E., Haase, J. & Garrison, J. Investigation of Ionospheric Electron Content Variations before Earthquakes in Southern California, 2003–2004. *J. Geophys. Res.* **112**(B2), 1–20, https://doi.org/10.1029/2006JB004447 (2007).
25. Heki, K. Ionospheric Electron Enhancement Preceding the 2011 Tohoku-Oki Earthquake. *Geophys. Res. Lett.* **38**(17), 1–5, https://doi.org/10.1029/2011GL047908 (2011).
26. Fraser-Smith, A. C. *et al*. Low-frequency magnetic field measurements near the behaviour of the Ms 7.1 Loma Prieta Earthquake. *Geophys. Res. Lett.* **17**(9), 1465–1468, https://doi.org/10.1029/GL017i009p01465 (1990).
27. Hattori, K. ULF Geomagnetic Changes Associated with Large Earthquakes. *TAO* **15**(3), 329–360 (2004).
28. Donner, R. V., Potirakis, S. M., Balasis, G., Eftaxias, K. & Kurths, J. Temporal correlation patterns in pre-seismic electromagnetic emissions reveal distinct complexity profiles prior to major earthquakes. *Phys. Chem. Earth Parts A/B/C*; https://doi.org/10.1016/j.pce.2015.03.008 (2015).
29. Parrot, M. Satellite observations of ionospheric perturbations related to seismic activity in *Earthquake Prediction Studies:* Seismo Electromagnetics (ed. Hayakawa, M.) 1–16 (TERRAPUB, Tokyo, 2013).
30. Lagoutte, D. *et al*. The DEMETER science mission centre. *Planetary and Space Science* **54**(5), 428–440 (2006).
31. Parrot, M. *et al*. Examples of unusual ionospheric observations made by the DEMETER satellite over seismic regions. *Phys. Chem. Earth* **31**, 486–495 (2006).
32. Nêmec, F., Santolik, O., Parrot, M. & Berthelier, J. J. Spacecraft observations of electromagnetic perturbations connected with seismic activity. *Geophys. Res. Lett.* **35**, L05109, https://doi.org/10.1029/2007GL032517 (2008).
33. Piša, D., Nêmec, F., Santolik, O., Parrot, M. & Rycroft, M. Additional attenuation of natural VLF electromagnetic waves observed by the DEMETER spacecraft resulting from preseismic activity. *J. Geophys. Res. Space Phys.* **118**; https://doi.org/10.1002/jgra.50469 (2013).
34. Yan, R., Parrot, M. & Pinçon, J.-L. Statistical study on variations of the ionospheric ion density observed by DEMETER and related to seismic activities. *J. Geophys. Res. Space Phys.* **122**; https://doi.org/10.1002/2017JA024623 (2017).
35. De Santis, A. *et al*. Potential earthquake precursory pattern from space: the 2015 Nepal event as seen by magnetic *Swarm* satellites. *Earth Planet. Sci. Lett.* **461**, 119–126 (2017).

36. Akhoondzadeh, M., De Santis, A., Marchetti, D., Piscini, A. & Cianchini, G. Multi precursors analysis associated with the powerful Ecuador (MW = 7.8) earthquake of 16 April 2016 using *Swarm* satellites data in conjunction with other multi-platform satellite and ground data. *Advances in Space Research* **61**(1), 248–263 (2018).
37. Akhoondzadeh, M., De Santis, A., Marchetti, D., Piscini, A. & Jin, S. Anomalous seismo-LAI variations potentially associated with the 2017 M_w = 7.3 Sarpol-e Zahab (Iran) earthquake from *Swarm* satellites, GPS-TEC and climatological data. *Advances in Space Research* **64**, 143–158 (2019).
38. Marchetti, D. & Akhoondzadeh, M. Analysis of *Swarm* satellites data showing seismo-ionospheric anomalies around the time of the strong Mexico (Mw = 8.2) earthquake of 08 September 2017. *Advances in Space Research* **62**(3), 614–623, https://doi.org/10.1016/j.asr.2018.04.043 (2018).
39. Marchetti, D. *et al*. Magnetic field and electron density anomalies from *Swarm* satellites preceding the major earthquakes of the 2016-2017 Amatrice-Norcia (Central Italy) seismic sequence. *Pure appl. Geophys*.; https://doi.org/10.1007/s00024-019-02138-y (2019).
40. Marchetti, D. *et al*. Pre-earthquake chain processes detected from ground to satellite altitude in preparation of the 2016-2017 seismic sequence in Central Italy. *Remote Sensing of Environment* **229**, 93–99 (2019).
41. De Santis, A. *et al*. Magnetic Field and Electron Density Data Analysis from *Swarm* Satellites Searching for Ionospheric Effects by Great Earthquakes: 12 Case Studies from 2014 to 2016. *Atmosphere* **10**(7), 371, https://doi.org/10.3390/atmos10070371 (2019).
42. Reasenberg, P. Second-order moment of central California seismicity, 1969-82. *J. Geophys. Res.* **90**, 5479–5495 (1985).
43. Molchanov, O. & Hayakawa, M. Subionospheric VLF signal perturbations possibly related to earthquakes. *J. Geophys. Res.* **103** (A8, 17), 489–17, 504 (1998).
44. Dobrovolsky, I. P., Zubkov, S. I. & Miachkin, V. I. Estimation of the Size of Earthquake Preparation Zones. *Pure appl. Geophys.* **117**, 1025, https://doi.org/10.1007/BF00876083 (1979).
45. Rikitake, T. Earthquake precursors in Japan: precursor time and detectability. *Tectonophysics* **136**, 265–282 (1987).
46. Shapiro, S. A., Huenges, E. & Borm, G. Estimating the crust permeability from fluid injection-induced seismic emission at the KTB site. *Geophysical Journal International* **131**(2), 15–18 (1997).
47. Ide, S., Beroza, G. C., Shelly, D. R. & Uchide, T. A scaling law for slow earthquakes. *Nature* **447**, 76–79 (2007).
48. Shen, X. *et al*. The earthquake-related disturbances in ionosphere and project of the first China seismo-electromagnetic satellite. *Earthq. Sci.* **24**, 639–650 (2011).
49. Friis-Christensen, E., Luhr, H. & Hulot, G. *Swarm*: A constellation to study the Earth's magnetic field. *Earth Plan. Space* **58**, 351–358 (2006).
50. Qiu, Y. *et al*. Combining CHAMP and *Swarm* Satellite Data to Invert the Lithospheric Magnetic Field in the Tibetan Plateau. *Sensors* **7**(17), 238 (2017).
51. Thébault, E. *et al*. International geomagnetic reference field: the 12th generation. *Earth Plan. and Space* **67**(1), 79 (2015).
52. Pinheiro, K. J., Jackson, A. & Finlay, C. C. Measurements and uncertainties of the occurrence time of the 1969, 1978, 1991, and 1999 geomagnetic jerks. *Geochemistry, Geophysics, Geosystems* **12**, Q10015 (2011).
53. Li, M. & Parrot, M. Statistical analysis of an ionospheric parameter as a base for earthquake prediction. *J. Geophys. Res. Space Phys.* **118**(6), 3731–3739 (2013).
54. Hakimhashemi, A. H. & Grünthal, G. A Statistical Method for Estimating Catalog Completeness Applicable to Long-Term Nonstationary Seismicity Data. *Bull. Seismol. Soc. Am.* **102**(6), 2530–2546, https://doi.org/10.1785/0120110309 (2012).
55. Piscini, A., De Santis, A., Marchetti, D. & Cianchini, G. A multi-parametric climatological approach to study the 2016 Amatrice-Norcia (Central Italy) earthquake preparatory phase. *Pure appl. Geophys.* **174**(10), 3673–3688 (2017).
56. Plastino, W., Bella, F., Catalano, P. G. & Di Giovambattista, R. Radon groundwater anomalies related to the Umbria–Marche, September 26, 1997, earthquakes. *Geofis. Int.* **41**(4), 369–375 (2002).

Acknowledgements

This work was undertaken in the framework of the ESA-funded project SAFE (*Swarm* for Earthquake study; http://safe-swarm.ingv.it), and partly (in its final part) under the LIMADOU-Science, a project funded by the Italian Space Agency (ASI). We thank ESA officers and all scientists of geomagnetism community for making possible the *Swarm* satellite mission. We also thank the members of the scientific panel that evaluated results by SAFE project (i.e. Drs. Lj.R. Cander – chair, G. Balasis, R. Console, P. Nenovsky and M. Parrot). We finally acknowledge the comments of three anonymous referees that helped us to improve the manuscript significantly.

Author contributions

Conceptualization, AngD.S., L.P., R.D.G. and G.D.F.; Methodology, AngD.S.; Software, F.J.P.C., D.M., L.S., G.C., M.S., S.A.C. and AnnD.S.; Validation, D.M., LuA. and L.S.; Formal Analysis, F.J.P.C., L.S. and D.M.; Investigation, AngD.S., D.M., D.S. and L.S.; Resources, AngD.S., L.P., G.D.F.; Data Curation, D.M., S.A.C., L.S., A.I. and A.P.; Writing – Original Draft Preparation, AngD.S., D.M., S.A.C.; Writing – Review & Editing, all authors; Visualization, D.M., L.S. and AnnD.S.; Supervision, AngD.S., L.P., R.D.G., C.C., R.H.; Project Administration, L.A., M.C., F.S., C.A. and D.D.; Funding Acquisition, AngD.S. and C.A.

Competing interests

The authors declare no competing interests.

Additional information

Supplementary information is available for this paper at https://doi.org/10.1038/s41598-019-56599-1.

Correspondence and requests for materials should be addressed to A.D.S.

Reprints and permissions information is available at www.nature.com/reprints.

Publisher's note Springer Nature remains neutral with regard to jurisdictional claims in published maps and institutional affiliations.

remote sensing

MDPI

Article

Worldwide Statistical Correlation of Eight Years of *Swarm* Satellite Data with M5.5+ Earthquakes: New Hints about the Preseismic Phenomena from Space

Dedalo Marchetti [1], Angelo De Santis [2], Saioa A. Campuzano [3], Kaiguang Zhu [1,*], Maurizio Soldani [2], Serena D'Arcangelo [2,4], Martina Orlando [2], Ting Wang [1], Gianfranco Cianchini [2], Domenico Di Mauro [2], Alessandro Ippolito [2], Adriano Nardi [2], Dario Sabbagh [2], Wenqi Chen [1], Xiaodan He [1], Xuhui Shen [5], Jiami Wen [1], Donghua Zhang [1], Hanshuo Zhang [1], Yiqun Zhang [1] and Zhima Zeren [5]

1 College of Instrumentation and Electrical Engineering, Jilin University, Changchun 130061, China; dedalomarchetti@jlu.edu.cn (D.M.); tingwang20@mails.jlu.edu.cn (T.W.); wqchen21@mails.jlu.edu.cn (W.C.); hexd19@mails.jlu.edu.cn (X.H.); wenjm20@mails.jlu.edu.cn (J.W.); zhangdh6518@mails.jlu.edu.cn (D.Z.); zhanghs6518@mails.jlu.edu.cn (H.Z.); yiqun21@mails.jlu.edu.cn (Y.Z.)
2 Istituto Nazionale di Geofisica e Vulcanologia, 00143 Rome, Italy; angelo.desantis@ingv.it (A.D.S.); maurizio.soldani@ingv.it (M.S.); serena.darcangelo@ingv.it (S.D.); martina.orlando@ingv.it (M.O.); gianfranco.cianchini@ingv.it (G.C.); domenico.dimauro@ingv.it (D.D.M.); alessandro.ippolito@ingv.it (A.I.); adriano.nardi@ingv.it (A.N.); dario.sabbagh@ingv.it (D.S.)
3 Instituto de Geociencias IGEO (CSIC-UCM), 28040 Madrid, Spain; saioa.arquero@igeo.ucm-csic.es
4 Facultad de Ciencias Físicas, Universidad Complutense de Madrid (UCM), 28040 Madrid, Spain
5 Space Observation Research Center, National Institute of Natural Hazards, MEMC, Beijing 100085, China; xuhuishen@ninhm.ac.cn (X.S.); zerenzhima@ninhm.ac.cn (Z.Z.)
* Correspondence: zhukaiguang@jlu.edu.cn

Abstract: Nowadays, the possibility that medium-large earthquakes could produce some electromagnetic ionospheric disturbances during their preparatory phase is controversial in the scientific community. Some previous works using satellite data from DEMETER, *Swarm* and, recently, CSES provided several pieces of evidence supporting the existence of such precursory phenomena in terms of single case studies and statical analyses. In this work, we applied a Worldwide Statistical Correlation approach to **M5.5+ shallow earthquakes** using the first **8 years of *Swarm*** (i.e., from November 2013 to November 2021) **magnetic field and electron density signals** in order to improve the significance of previous statistical studies and provide some new results on how earthquake features could influence ionospheric electromagnetic disturbances. We implemented new methodologies based on the hypothesis that the anticipation time of anomalies of larger earthquakes is usually longer than that of anomalies of smaller magnitude. We also considered the **signal's frequency** to introduce a new identification criterion for the anomalies. We find that taking into account the frequency can improve the statistical significance (up to 25% for magnetic data and up to 100% for electron density). Furthermore, we noted that the **frequency** of the *Swarm* **magnetic field signal** of possible precursor anomalies seems to slightly **increase as the earthquake is approaching**. Finally, we checked a possible relationship between the frequency of the detected anomalies and earthquake features. The earthquake focal mechanism seems to have a low or null influence on the frequency of the detected anomalies, while the epicenter location appears to play an important role. In fact, **land** earthquakes are more likely to be preceded by **slower** (lower frequency) magnetic field signals, whereas **sea** seismic events show a higher probability of being preceded by **faster** (higher frequency) magnetic field signals.

Keywords: electromagnetic; frequency; *Swarm*; earthquake; precursors; ionosphere

Citation: Marchetti, D.; De Santis, A.; Campuzano, S.A.; Zhu, K.; Soldani, M.; D'Arcangelo, S.; Orlando, M.; Wang, T.; Cianchini, G.; Di Mauro, D.; et al. Worldwide Statistical Correlation of Eight Years of *Swarm* Satellite Data with M5.5+ Earthquakes: New Hints about the Preseismic Phenomena from Space. *Remote Sens.* **2022**, *14*, 2649. https://doi.org/10.3390/rs14112649

Academic Editor: Michael E. Gorbunov

Received: 7 May 2022
Accepted: 30 May 2022
Published: 1 June 2022

1. Introduction

In this paper, we will deal with the delicate research on the possible precursors of earthquakes, i.e., those anomalous phenomena that might appear before earthquakes because they are caused by their preparation phase and thus anticipate their imminent occurrence. The earthquake precursors could be simply classified as seismic precursors and non-seismic precursors: the former are eventual modifications of seismicity or seismological parameters before the occurrence of an earthquake, while the latter, the object of our present research, are alterations of some geophysical parameters, such as atmospheric chemical and physical characteristics, radon emission, and, furthermore, possible electromagnetic disturbances up to the ionosphere [1–3]. Historically, some evidence of electromagnetic precursors has been reported in the data from ground magnetic observatories—for example, before the M6.9 Spitak (Armenia) 1988 and M7.1 Loma-Prieta 1989 earthquakes by Fraser-Smith et al. [4] and Molchanov et al. [5]. A model to explain the generation of Ultra Low Frequency (ULF) electromagnetic waves responsible for such pre-earthquake disturbance was proposed by Molchanov and Hayakawa [6] and based on electromagnetic pulses produced by the separation of electric charges at the fault level due to micro-fracturing activity during the preparation phase of the earthquake. Variations of this explanation have been proposed; e.g., [7], introducing a better model for microfracturing rate variation on the time and improving the geometry of the fault. However, one of the most important theories was put forward by Freund [8,9], which proposed the generation of positive holes (called p-holes) due to the peroxy defects on the rocks also induced by stress on the rock. Freund proposed such theory as a "universal" explanation of all other precursors: for example, he proposed that the detected Thermal-InfraRed anomalies could be explained by photon emission in such wavelengths due to the recombination at the Earth's surface of the peroxy bonds, as well as their location atop topographical profiles by the electrical migration of p-holes in the lithosphere due to the "tip electric effect" [9]. Even if p-holes are a different source with respect to the one initially proposed, the propagation mechanism of the eventual pre-earthquake ULF waves could, in principle, remain unchanged. Other theories have also been developed and warrant consideration—for example, supposing that the release of p-holes at the Earth's surface can produce an accumulation of electric charges that could gradually create a perturbation in the atmosphere and then propagate up to the ionosphere in the form of plasma bubble, interacting and following the magnetic field, as numerically simulated by Kuo et al. [10,11]. Such simulation opened a scientific discussion, as Prokhorov and Zolotov [12] found that some assumptions in the model were too simplified, and Kuo and Lee replied with an update of the original work, showing that the model seems, in any case, valid [13]. Furthermore, Denisenko et al. [14,15] found some possible inaccuracies in the model of Kuo et al., proposing another model that improved the calculus of the conductivity in the ionosphere, but the value on the ground of the electric field strength signal necessary to create a small perturbation of the ionosphere was found to be very large, even if it is still possible. As stated by the same authors of all these papers, more pieces of evidence are necessary to understand if such phenomena exist and which could be the most reliable model to describe them. This paper aims to provide some further observational points for such discussion.

According to Pulinets and Ouzounov [16], the ionization of the air could be also produced by the release of radon instead of (or in addition to) the p-holes. Additionally, other mechanisms for electric (or electromagnetic) disturbances have been proposed based on the change of the resistivity of rocks caused by the movements of fluids (the highly conductive water that fills the new cracks) in the crust before the occurrence of the earthquake under the so-called "Dilatancy Model" by Scholz et al. [17]. For instance, the movement of fluids in Central Italy prior to the occurrence of significant earthquakes has been detected from seismological analyses [18]. Changes in resistivity have been supposed and calculated to describe the atmospheric electric and magnetic field anomalies detected by a ground antenna [19]. Furthermore, ground and atmospheric observations, together with *Swarm* magnetic field satellite anomalous data, have been proposed as good candi-

dates to describe a pre-earthquake chain of anomalies [20]. A comprehensive review of several models of the Lithosphere–Atmosphere–Ionosphere (or, in some cases, just the Lithosphere–Ionosphere) Coupling models has been provided by Liperovsky et al. [21], where other possible physical couplings are also proposed such as pre-earthquake acoustic gravity waves, atmospheric electric currents possibly generated by the release of charged aerosol, variations in the D and E layers in the ionosphere induced by radon release, a direct resonator between the lithosphere and the ionosphere that is supposed to form a spherical capacitor in this model, and even more challenging possible explanations. Previous statistical works have provided pieces of evidence of the correlation of the ionospheric disturbances in terms of electron density measured by the DEMETER satellite, finding a significant increase from 10 to 6 days prior to the seismic M4.8+ events [22–24], and an increase in the electric field (typically around 10/20 mV/m) from a few minutes to some days prior to several M5+ earthquakes was reported by Zolotov [25] using DEMETER and INTERCOSMOS-BULGARIA-1300 satellites. Previous studies by some of the authors of this paper analyzed the *Swarm* and China Seismo Electromagnetic Satellite (CSES) data prior to the occurrence of about 20 earthquakes in recent years with a magnitude "M" in the range $6.0 \leq M \leq 8.3$ [26–28]. The worldwide systematic association of detected ionospheric disturbances in the magnetic field and electron density with earthquakes has been statistically proved by De Santis et al. [29], and a preliminary investigation of CSES-01 electron density data has also shown promising results [30].

The present work is the natural extension of the first statistical and systematic analysis of correlation using satellite magnetic field data from *Swarm* satellites with global M5.5+ shallow earthquakes [29]. Here, a temporal extension of the analysis is provided in terms of analyzed time (i.e., 8 years instead of 4.7 years) and the preparation time before the earthquake (from 1000 days before, instead of 500 days before). Furthermore, some new methodologies are also provided to corroborate the results.

In Section 2, we provide a brief introduction about the investigated dataset and the data analysis method. Section 3 illustrates the results, which are deeply discussed in Section 4. In Section 5, we present some conclusions and future perspectives.

2. Materials and Methods

2.1. Investigated Datasets

This study investigates satellite datasets from the *Swarm* satellite mission and earthquakes from the United States Geological Survey (USGS) catalog, as described in the following sections.

2.1.1. Satellite Datasets

In this paper, we analyze the ionospheric disturbances retrieved from satellite in situ measurements possibly related to earthquakes. In particular, we analyze data from the *Swarm* three-identical satellite constellation launched by the European Space Agency (ESA) on 22 November 2013. At the present time (April 2022), all three satellites are still in orbit, with most instruments in good condition. The *Swarm* constellation is the "state of the art" to monitor with the best accuracy the spatial structure and the temporal evolution of the Earth's magnetic field from space [31]. All three *Swarm* satellites include identical payloads onboard. In particular, in this work, the Y-East component of the magnetic field and electron density (*Ne*) are analyzed as originally measured by fluxgate magnetometers (Vector Field Magnetometer, VFM) and Langmuir probes (Electric Field Instrument, EFI), respectively. The Y-East magnetic field component has been selected, as it is expected to be more sensitive to the internal perturbations [32] and, in the case of Lithosphere–Atmosphere–Ionosphere Coupling (LAIC) coupling, to the Field Aligned Currents (FAC) induced by air ionization from radon release or p-holes. At the ionospheric heights, these currents are expected to be almost horizontal, while at the ground/atmospheric level they are expected to be almost vertical [21]. Among the two X-North and Y-East horizontal components, the Y-East component should be more sensitive to such kinds of perturbations, as it is quasi-orthogonal

to the main geomagnetic field generated by the Earth's outer core, so we expect that the same absolute perturbation is more evident on the Y-East component. The used magnetic field data are at "Low-Resolution" and are provided at a sample rate of 1 Hz in a daily file that contains 86,400 samples associated with 31 or 32 tracks (i.e., half orbits) per day. *Swarm Ne* is sampled at 2 Hz and is provided in the Electric Field Instrument (EFI) product. There is an open debate on the discrepancies in the *Ne* absolute value calibration measured with another satellite in a similar orbit, the China Seismo-Electromagnetic Satellite (CSES). For instance, it is known that the absolute value of electron density measured by CSES-01 (i.e., the first satellite of the CSES series) is lower than the ones estimated by *Swarm* [33] and by the IRI-2016 ionospheric model (e.g., comparison in the Indonesia area in [34]). However, such an absolute difference (bias) does not affect our results because our algorithms work on residuals, i.e., they are based on variations measured along the track, which are well consistent between the two satellite missions [33,34].

This paper analyzes the nighttime and daytime tracks for both the magnetic field (B) and electron density (*Ne*) datasets. In fact, as the investigation approach is track-by-track, we do not expect that the solar-driven daytime activity can affect our result in terms of "false anomalies", even if some potential pre-earthquake anomalies could be lost inside the higher day noise (especially for *Ne*).

2.1.2. Earthquake Catalog Acquisition and Pre-Processing

We retrieved the M5+ global earthquakes (EQs) that occurred in the same analyzed time interval from the USGS global catalog, which provides an estimation of the hypocenter, origin time, and magnitude (generally, the moment magnitude Mw calculated from the centroid moment tensor inversion, or, in alternative, the short-period body wave magnitude mb or other values). We then applied a declustering technique using Reasenberg's [35] method to remove aftershocks and foreshocks. With respect to the previous work of De Santis et al. [29], here, a slightly larger time window is utilized—10 days before and 20 days after the events—to search for other possible related events of the same cluster, while the other parameters were unchanged (i.e., a radius of 10 km, magnitude cut-off of 5.0, confidence level of 95%, hypocenter uncertainty according to the catalog). For further details on the declustering of the catalog and how this impacts this work, the reader is invited to see Appendix A. In the declustered catalog, only the shallow (depth $\leq$ 50 km) EQs with a magnitude greater than or equal to 5.5 are selected as the seismic dataset for further processing. In the first 8 years of *Swarm*, slightly fewer than 2200 shallow M5.5+ earthquakes were finally selected.

2.2. Methods of Analysis

Firstly, the *Swarm* satellite data are pre-processed by MAgnetic *Swarm* anomaly detection by Spline analysis (MASS) or electron density (*Ne*) Anomaly Detection (NeAD) algorithms to search for anomalies. The approach applied to the magnetic field and electron density data is basically the same, and only some parameters are settled differently to consider the different sample frequencies and signal-to-noise ratios properly. MASS and NeAD perform the following operations while taking into account the data along the track between -50° and $+50^\circ$ geomagnetic latitude (see Figure S1 in the Supplementary Materials as an example of data processing):

1. First differences of the data: the difference between two consecutive data divided by the time interval between them (as a first order approximation of the temporal derivative).
2. Removal of the residual trend: a cubic spline coming from the fitting of the derivative of the data (as obtained from Step 1) is removed.
3. Analysis of the residuals obtained from Step 1 and Step 2 along the track: moving windows of 7° latitude are used, with an incremental shift of 1/5 of the window length (i.e., ~1.4° of latitude).

4. The root mean square (rms) is calculated inside the window and compared with the whole track's Root Mean Square (RMS). The anomaly is defined if $rms > k_t \cdot RMS$ (k_t is chosen as 2.5 or 3 if no-frequency investigation is performed; more details are given later on).

In addition, a new frequency analysis is carried out, and the Fast Fourier Transform (FFT) is calculated for each moving window and for the whole spectrum. Three sub frequency bands are divided according to their period ranges: (2–10) s, (10–25) s, and (25–50) s. In each frequency band, the anomaly is defined if the mean intensity overpasses the mean *FFT* intensity plus K_{FFT} times its standard deviation σ (for example, for the 2–10 s band, the anomaly is defined if $FFT(2s \leq p \leq 10s) > FFT + K_{FFT} \cdot \sigma(FFT)$. This criterion on K_{FFT} is in addition to Step 4 about k_t, but it is not applied for the basic anomaly extraction (i.e., when no frequency analysis is made). We recognize that the residuals with respect to the spectral mean are not Gaussian, but it is feasible to introduce the standard deviation simply as an operational measure of the data dispersion around the mean of the spectrum. Even if other quantities (e.g., the absolute mean deviation or the largest deviation) could be used, we found that the results are practically the same, so we preferred to use the standard deviation that can be easily and quickly estimated.

The two datasets (satellite anomalies and earthquakes) are investigated by the Worldwide Statistical Correlation (WSC) algorithm fully described in [29] that is only briefly summarized here.

The WSC algorithm first extracts the subset of anomalies and earthquakes to be correlated by a Superposed Epoch and Space Approach (SESA). The anomalies are selected by applying several thresholds. In particular, we only select tracks in geomagnetic quiet time (i.e., when the geomagnetic indices satisfy the following conditions: $|\,\mathrm{Dst}\,| \leq 20$ nT and $a_p \leq 10$ nT), with all samples acquired in nominal satellite conditions (checked by the "Quality Flags" of the *Swarm* satellite, according to the respective operating manuals), and put conditions over the rms of the window and, for some analyses, an additional threshold on the frequency. For each earthquake of magnitude M, the anomalies inside its preparation area, as defined by a circular area with a Dobrovolsky's radius (in km: $10^{(0.43 \cdot M)}$ [36]) that occurred in the analyzed window (for example, from 500 days before the earthquake until 500 days after it), are extracted. If an anomaly is univocally associated with one earthquake, this couple (anomaly–earthquake) is defined. In case the anomaly is compatible with more than one seismic event, one of the following four methods is used to select which earthquake is associated with the anomaly:

1. **Method 1 "All anomalies–EQs"**. This method selects all earthquakes compatible with the investigated anomaly. The advantage is that we do not apply any assumption for the analysis, and we can suppose that, in case the statistics are sufficient, the "wrong" anomaly–earthquake couples increase just the background without creating additional artificial concentrations of anomalies. On the other side, one disturbance can be produced only by one earthquake, and so, unless the signal is superposed (or under the satellite resolution), the anomaly could not be associated with more than one event. For this reason, we also introduce the following methods.
2. **Method 2 "Min [log(ΔT R)]"**. This method selects the closest earthquake in space ("R") and time (anticipation time $\Delta T = time_{EQ} - time_{anomaly}$). The selection is made by searching for the minimum of the following equation: $\log_{10}(|\,\Delta T \cdot R\,|)$. The criterion is based on the assumption that an anomaly is more likely to be produced by the closest earthquake in space and time.
3. **Method 3 "Max (magnitude)"**. This method selects the earthquake with the highest magnitude in the space and time domains of interest. The assumption is that a larger earthquake produces more anomalies before its occurrence that can be detectable in the ionosphere.

4. **Method 4 "Closer (Rikitake)"**. This method takes into account that a larger earthquake with a magnitude M is expected to have a longer anticipation time ΔT of its possible precursors, according to the Rikitake law [37], expressed as:

$$\Delta T = a + b \cdot M \quad (1)$$

With this method, the anticipation time ΔT is calculated using the a and b coefficients found for the *Swarm* satellite data (magnetic field or *Ne*) by De Santis et al. [29] and inserted in the Rikitake law expression. On the other side, the decimal logarithm of the real anticipation time is calculated, and the earthquake that presents the minimum difference with respect to the Rikitake law is selected.

Please note that the first three methods are the same as those used by De Santis et al. [29], while here, a new fourth method is also proposed. Hereafter, if no indication is given about the method, the analysis will follow Method 1, i.e., all anomalies are associated with all the compatible earthquakes. Finally, it is worth noticing that any method presents advantages and disadvantages, as we do not know the exact mechanism behind the generation of ionospheric disturbances (even if several theories have been proposed). We can rely on the concentrations of anomalies confirmed by several of these methods and expect that a future better understanding of the LAIC mechanism can improve the selection of the best of the above methods or help formulate a new one. Of course, all methods take advantage of the fact that all analyses are retrospective. It would be more difficult to adapt the methods for a real time analysis rather than establish a significant correlation between ionospheric anomalies and earthquakes, but this is not within the present scope of the work.

The results are illustrated in a "standard" representation graph (see, for example, Figure 1), where the horizontal axis represents the time of the anomaly with respect to the earthquake occurrence (i.e., negative days before the earthquake occurrence and positive days after), and the vertical axis is the distance of the detected anomaly in terms of degrees from the epicenter. Therefore, each anomaly is placed on this graph in terms of distance in time and space from its associated earthquake (according to one of the four previously listed methods). All the anomalies and earthquakes are superposed on the same graph, and, in the end, the results are binned in 50 horizontal and 10 vertical cells (or bins). For each bin, the number of anomalies falling in the bin is divided by its geographic area (circle or annulus), obtaining the anomalies' density represented by a color bar scale. For the first row (which represents the 50 temporal bins closer to the epicenters), the maximum concentration of such density is searched, and its location (pxmax), the number of anomalies (Nmax), the number of EQs associated with these anomalies (NEQmax), and the total sum of the released energy (E_{EQ}) is reported in the second line of the heading. Furthermore, for such a maximum density/concentration bin, other statistical quantities are evaluated and described in the following paragraph.

To evaluate if the results obtained from the WSC of real earthquake and anomaly data are statistically significant, 30 random space-time homogeneous distributions of anomalies, with the same number of anomalies as each real data analysis, have been generated. Then, the WSC algorithm has been applied with the same parameters used for the real satellite anomalies. In particular, for the maximum concentration, we estimate the quantity, D_{MAX}/D_0, that represents the density of anomalies in the maximum (D_{MAX}) with respect to a theoretical homogeneous distribution of anomalies (D_0):

$$D_{MAX}/D_0 = \frac{N_{anom}^{MAX} \cdot \Delta T^{Tot} \cdot Area^{Tot}}{N_{anom}^{Tot} \cdot \Delta T^{pixel} \cdot Area^{pixel} \cdot n_{EQ}} \quad (2)$$

where N_{anom}^{MAX} is the number of anomalies in the maximum pixel (which, in the title of the graphs, is indicated as "N_{MAX}") that has a duration ΔT^{pixel} and covers an area $Area^{pixel}$. The total number of identified anomalies (independently from the earthquakes) is N_{anom}^{Tot}, and it is also indicated in the first line of the heading of the graph as the second number (63,178 in the case of Figure 1). The whole analyzed area (i.e., the spherical zone between

50°S and 50°N of geomagnetic latitude) is $Area^{Tot}$, and the total analyzed time is ΔT^{Tot} (in this work, it is 8 years). The quantity D_{MAX}/D_0 has been calculated for real analysis, i.e., $[D_{MAX}/D_0]_{real}$, and its mean random value $\overline{[D_{MAX}/D_0]}_{random}$ and its standard deviation (σ) have been estimated over a set of 30 random simulations. By these quantities, we defined the two statistical parameters, d and n:

$$d = \frac{[D_{MAX}/D_0]_{real}}{\overline{[D_{MAX}/D_0]}_{random}}; n = \frac{[D_{MAX}/D_0]_{real} - \overline{[D_{MAX}/D_0]}_{random}}{\sigma([D_{MAX}/D_0]_{random})} \quad (3)$$

According to the above definitions, d represents how many times the real maximum concentration is higher than the one expected from random simulations, and n estimates how many standard deviations (of random simulations) the real concentration is higher than the random one. The number of random simulations was chosen as a function of the results in terms of the reached stability of the obtained values of d and n. We found that, generally, even with one or two random simulations, the estimation of d is accurate up to one decimal digit (if the number of anomalies is greater than 30,000), while n requires more random runs, i.e., at least 15 or 30 simulations for about 30,000 anomalies.

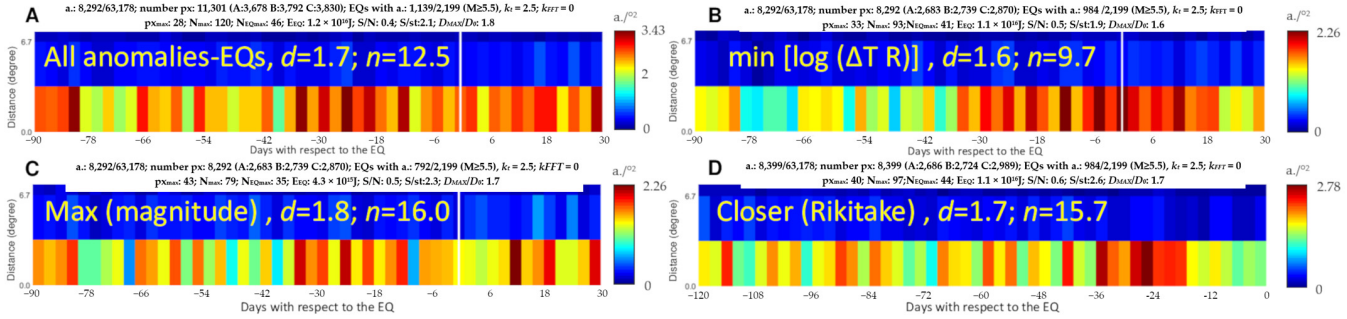

Figure 1. Correlation of *Swarm* magnetic field anomalies with M5.5+ earthquakes using four different methods: (**A**) all anomalies are associated with all compatible earthquakes; (**B**) each anomaly is associated with the closest earthquake in space and time, i.e., the minimum of log(ΔT R); (**C**) the anomaly is associated with the greatest magnitude earthquake; (**D**) the anomaly is associated with the earthquake closer to the Rikitake law, with coefficients from De Santis et al. [29]. The graphs are cut for the vertical section without significant information, showing only the closer band to the earthquake epicenter. The color bar represents the density of anomalies in terms of the number of anomalies per square degree.

When the concentration of the real anomalies is compatible with a homogeneous random simulation of anomalies, we expect $d \cong 1$ and $n \cong 0$. At the same time, we define a statistically significant concentration, i.e., a real distribution of anomalies with the largest concentration significantly differing from a random distribution, if $d \geq 1.5$ and $n \geq 4.0$, as suggested by De Santis et al. [29].

3. Results

We consider the three satellites of the *Swarm* mission and analyze two parameters: the Y-East component of the magnetic field and the electron density, *Ne*. All these results are shown in the following four subsections. Here, we present the figures with the most interesting results, while we provide other figures in the Supplementary Materials.

3.1. Swarm Magnetic Field Results

In this section, we applied the WSC algorithm to the *Swarm* magnetic field data recorded by the three main satellites of the constellation from 26 November 2013 until 25 November 2021, i.e., the first 8 years of available data. Figure 1 represents the WSC applied to the *Swarm* Y-East component magnetic field anomalies with M5.5+ earthquakes in a time window of 120 days (i.e., 90 days before each earthquake and 30 after for methods

1, 2, and 3, and 120 days before each earthquake for method 4) using the four methods to select which earthquake is associated with the anomaly in case of ambiguity. We note that all the methods identify the same group of anomalies from around −40 to −10 days, and, in some of them, it is also the absolute maximum concentration. It is very interesting that, even with Method 2, which minimizes the log (ΔT R), the absolute maximum concentration is 12 days prior to the earthquake and not the co-seismic, as the method would forcefully enhance the anomalies closer to the event (actually, it is only this method that presents a significant concentration at the earthquake occurrence, although it is not the largest one).

Figure S2 (in Supplementary Materials) reports the statistical correlation analysis for the *Swarm* Y-East magnetic field component anomalies (extracted with a threshold k_t = 2.5) with M5.5+ earthquakes from 500 days before until 500 days after each event using Method 1. With these criteria, we can obtain symmetric analyzed time and see that the maximum concentration of anomalies preceded the earthquake (of about 30 ± 10 days). Furthermore, the concentration of anomalies before the earthquake is slightly higher than that after the event. The total number of anomalies in the first row (i.e., the closest to the epicenter) before the earthquake is 16,630, while the total number after the earthquake is 16,436, showing that, before the earthquake, there are 194 more anomalies than the ones after it. Even if this number is just 1.2% more, it could support the idea that, inside the identified anomalies, there could be a part likely produced by ionospheric seismo-induced phenomena. A specific discussion that took into account the geomagnetic quiet and disturbed amount of time before and after each event is reported in Section 4.5, and the specific difference seems to be influenced by this aspect.

To search for a possible relationship between the anticipation time and magnitude of the earthquakes, the events have been divided into five magnitude bands (the same used in Figure 5 of De Santis et al. [30]): 5.5 ≤ M ≤ 5.9, 6.0 ≤ M ≤ 6.4, 6.5 ≤ M ≤ 6.9, 7.0 ≤ M ≤ 7.4, and M ≥ 7.5 using Method 1. Figure 2 represents the WSC applied to 8 years of *Swarm* magnetic field anomalies and earthquakes divided into magnitude bands. Here, an extended period before the earthquake (1000 days instead of 500, as in [29]) is used, as now the statistics are better supported by a larger amount of data. It is worth noting that, in these analyses, a part of the events is not fully analyzed. In particular, the earthquakes that occur in the first 1000 days of the analyzed years have an incomplete time window before them.

In Figure 2B, we can see that, in the four larger magnitude bands (i.e., for M6+), the absolute maximum concentration increases perfectly with the magnitude. The anticipation time in the function of the magnitude is presented with a fit (as determined by the Rikitake law, i.e., $\log\Delta T = a + bM$) in Figure 2A, where $a = -0.96 \pm 0.73$, and $b = 0.51 \pm 0.10$. For the lower magnitude earthquake bands (i.e., 5.5 ≤ M ≤ 5.9), the maximum concentrations are at −210, −150, and −90 days, but at the beginning of the graph (where we expect the maximum concentration corresponding to this band), there is also a high concentration of anomalies. We can explain such results in different ways, either independently or occurring simultaneously. One explanation is based on the fact that the lower magnitude earthquakes, i.e., those below M6.0, are less likely to produce distinguishable LAIC effects, while only a part of them can still show some possible ionospheric earthquake precursors. Furthermore, eventual ionospheric electromagnetic perturbations from lower magnitude earthquakes could be very much weaker, and the method presented in this paper could be insufficiently sensitive to detect all of them. An alternative explanation is that these lower magnitude earthquakes are so frequent that an anomaly can be associated with many of them, including those with a longer anticipation time. A third possible reason is that this lower magnitude band could have a typical anticipation time of less than 20 days, which is the most affected by the removal of earthquakes at these distances from larger earthquakes due to the applied declustering method. Despite these considerations, we noted that, in the Rikitake law of Figure 2A, the "not aligned" magnitude band with the fit is the one with earthquakes in the range of 6.0 ≤ M ≤ 6.4. Future investigations are necessary to clarify such ambiguity.

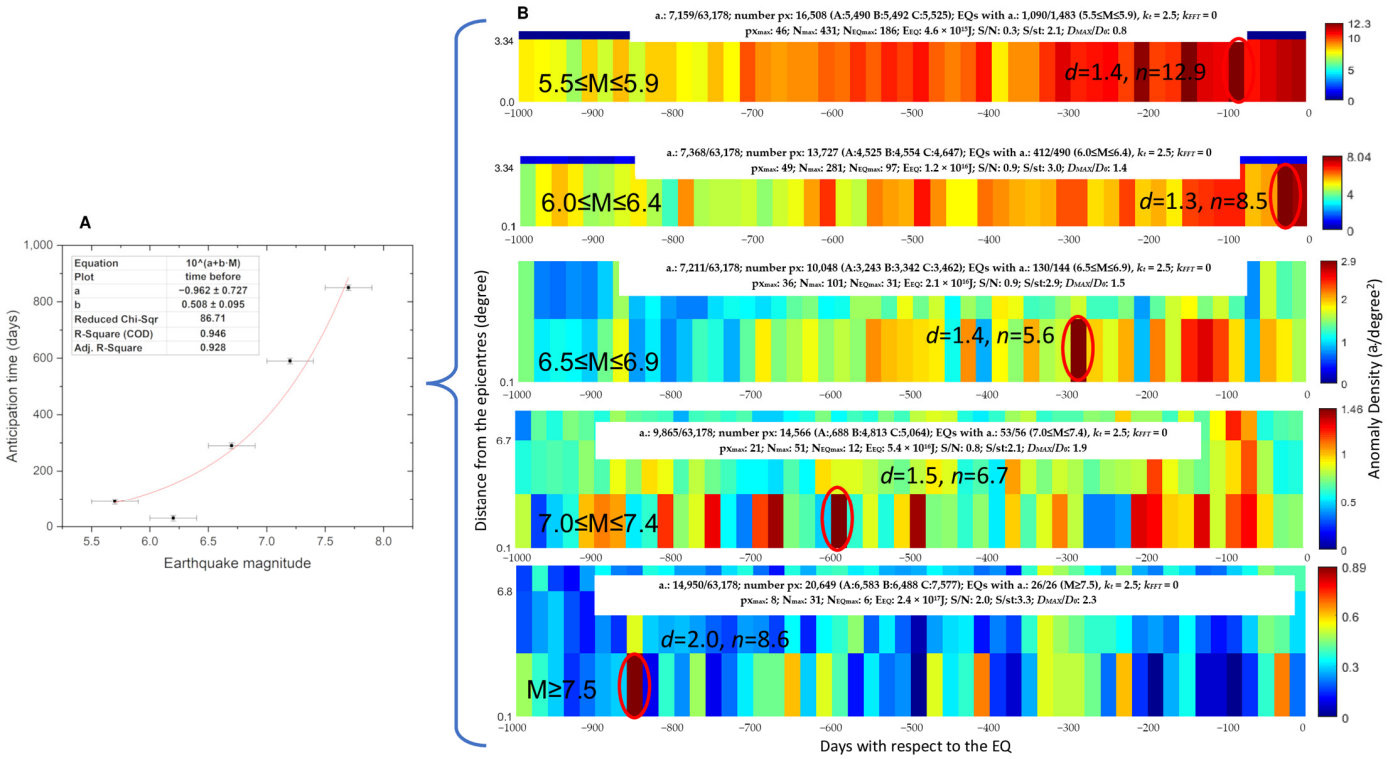

Figure 2. Correlation of *Swarm* magnetic field anomalies with earthquakes divided into five magnitude bands. (**A**) Fit of the anticipation time of maximum concentration (underlined by a red circle in subfigure (**B**) as a function of earthquake magnitude using the equation $\Delta T = 10^{a+b \cdot M}$. The error bar takes into account the width of the pixel. (**B**) Details of the analysis in the earthquake magnitude bands of $5.5 \leq M \leq 5.9$, $6.0 \leq M \leq 6.4$, $6.5 \leq M \leq 6.9$, $7.0 \leq M \leq 7.4$, and $M \geq 7.5$. Only the significant part of the superposed space-time graph is represented. The statistical indications of d (how many times the maximum real concentration is higher with respect to the random one) and n (how many standard deviations there are in which the real largest concentration is greater than the random one) are also shown. Such maximum concentrations (as objectively identified by the WSC algorithm) have been highlighted by a red or orange circle (the last one for a less significant concentration in terms of the Rikitake law). The color bar represents the density of the anomalies in terms of the number of anomalies per square degree.

A summary view of the WSC analysis of the *Swarm* magnetic field data applied to all the investigated M5.5+ earthquakes is provided in the Supplementary Materials in Figure S3, showing higher concentrations toward the earthquake occurrence.

To validate such results, an earthquake catalog with a shuffled magnitude has been produced, and we showed the results in Figure S4 in the Supplementary Materials. In the subplot on the left, it is possible to see that a correlation between the shuffled earthquake magnitudes and the real set is practically absent (R = 0.0004), while, on the right side of Figure S3, it is shown that the relationship between the anticipation time and the earthquake magnitude is lost, as expected after shuffling the earthquake catalog. Some minor correlations can still be found, but this could simply be due to the fact that, since we shuffled only magnitudes, the epicenter and the origin time of the events are still real, so the anomalies really preceded an earthquake.

Figure 3 shows the different analyses of the *Swarm* Y-East component magnetic field data, taking into account the signal's frequency correlated with M5.5+ earthquakes. For these analyses, we show the classical WSC with Method 1 (all possible combinations of anomalies and earthquakes) from 500 days before until 500 days after the earthquake. The periods are from the upward shorter period (2–10 s) (subpanels A) to the downward longer period (25–50 s) (subpanel C). We can note that it seems that the anticipation time increases

with the period of the signal, this being the time between the maximum concentration of the anomalies and the occurrence of the earthquake. This observation could be crucial for a future system to predict earthquakes, as the frequency of the signal could give important information of the time-lapse to the earthquake. We tried to provide a rough linear fit (see Figure S5 in the Supplementary Materials) of such an anticipation time, obtaining:

$$\Delta T = -24\ (\pm 19) + 4.01\ (\pm 0.82) \cdot P \tag{4}$$

where "ΔT" is the anticipation time in days, and "P" is the period of the signal in seconds.

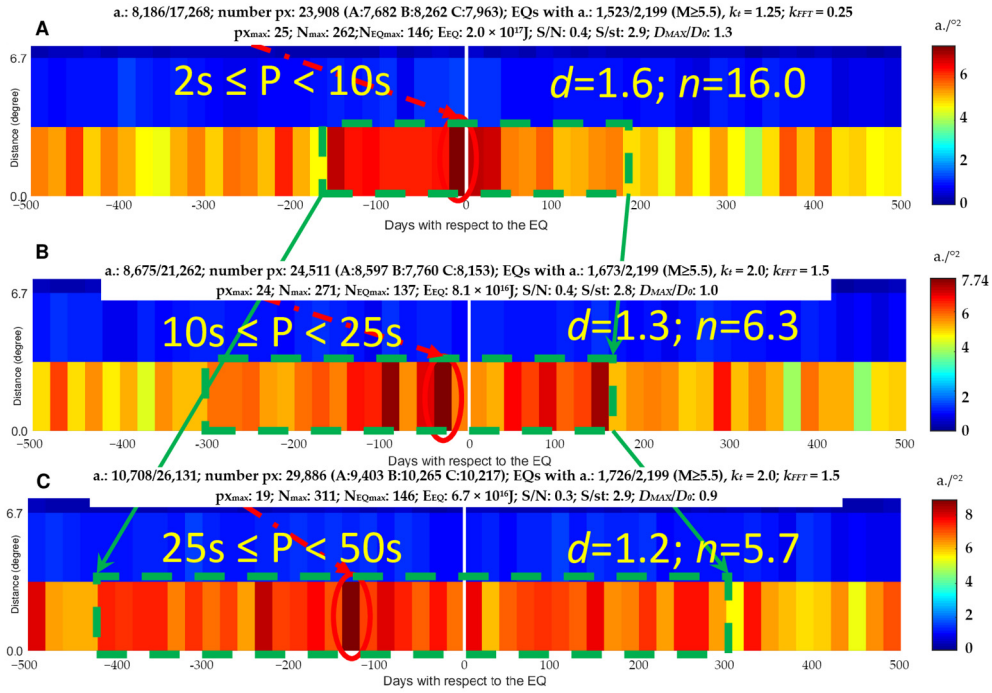

Figure 3. 8-year *Swarm* Y-mag data separated for frequency content in the anomalies correlated with M5.5+ earthquakes from 500 days before until 500 after their occurrence. The color bar represents the density of the anomalies in terms of the number of anomalies per square degree. The anomalies have been selected with higher signal content in three different period bands: (**A**) from 2 s to 10 s, (**B**) from 10 s to 25 s and (**C**) from 25 s to 50 s.

The fit provides a positive slope of about 4.0 days/s. The fact that the fit provides a negative intercept and then a possible negative anticipation time (and thus an effect after the earthquake) could be explained by the fact that the period stops at about 6 s before the earthquake's occurrence (i.e., $\Delta T = 0$, then $P = 6$ s). We provide a specific discussion on these results in Section 4.4.

We finally noted that there seems to be a very long period underlined by dashed green boxes in Figure 3, with higher anomaly concentrations with respect to the rest (the identification of the green boxes is taken by sight considering the "more red or brown" bins, subjectively). We speculate that the density of the anomaly in the tails (i.e., before or after the green dashed box) is not due to the earthquake and that it is in the background due to other sources, while the increase in the anomalies could be related to a sort of seismic activation and to the consequences of the seismic event after their occurrence. Even these higher anomaly regions increase their duration (before the earthquake) with the period of the investigated signal. Future studies are fundamental to investigate this aspect better.

Table S1 (in the Supplementary Materials) summarizes the main statistical results for all the investigated combinations of the 8-year *Swarm* magnetic field data correlated with M5.5+ shallow earthquakes. In particular, the two statistical quantities d and n are reported, along with the indication of when the maximum concentration of anomalies

occurs in the bin closest to the epicenter (negative if it occurs before the earthquake and positive if it happens after) and how many earthquakes are associated with anomalies in the pixel with the maximum concentration of anomalies. When a concentration passed the statistical evaluation criteria defined in [29] (i.e., $d \geq 1.5$ and $n \geq 4.0$) and occurred before the earthquake, we underline the row in green.

3.2. Swarm Electron Density Results

In this section, we applied the WSC algorithm to the electron density (*Ne*) data recorded by the three main satellites of the *Swarm* constellation from 2 December 2013 until 1 December 2021, i.e., the first 8 years of available data. Most of the results of *Ne* are provided in the Supplementary Materials, as they have not been found to be statistically significant. Figure S6 (in the Supplementary Materials) provides the results of WSC applied to 8 years of *Swarm Ne* data correlated with M5.5+ shallow earthquakes using the above four methods to associate the anomalies and earthquakes. The results do not pass the statistical criteria defined in [29]: $d \geq 1.5$ and $n \geq 4.0$. Furthermore, the analyses with the minimization of log (ΔT R) and the maximum earthquake magnitude (methods 2 and 3) find a post-seismic bin as the maximum concentration. In fact, the analysis in the long symmetrical time from 500 days before until 500 days after the earthquakes with the same data (Figure S7 in the Supplementary Materials) shows low or null significance, and, overall, the number of anomalies after the earthquake (15,618) is greater than those before the earthquake (15,504); their difference being equal to 114 anomalies, which is lower than the square root of the anomalies, which is equal to 125 and could be considered as an approximation of their uncertainty, as further discussed in Section 4.4.

In the same way that we detected an increase in the anticipation time of the anomalies with the earthquake magnitude in the magnetic field data (Figure 2), we now apply the same approach to 8 years of the *Swarm Ne* data, as shown in Figure S8 in the Supplementary Materials. In this case, we tried to make a fit through the maximum concentrations of anomalies detected by the WSC algorithm in the first row (i.e., closer to the earthquake epicenter) of different magnitude ranges following the empirical Rikitake law. We note that the magnitude 7.5+ earthquakes analysis shows the absolute maximum concentration on the second row, i.e., between 380 km and 750 km from the epicenter. As such, a magnitude range is the one with fewer earthquakes (26 in total); this effect could be due to an insufficient number of cases to construct good statistics. Furthermore, it is important to note that these analyses did not pass the statistical evaluation criteria, and some of them even show a concentration of the same intensity as the one expected for a random simulation ($d \cong 1$) and a negative n, indicating a real largest concentration lower than the random one. Even if the concentration of anomalies is not significant, the maximum concentration in the row closer to the epicenter for magnitudes $\geq$6 seems to follow the Rikitake law, as can be seen in the fit shown in Figure S8A, which provides the following coefficients: $a = -3.5 \pm 2.1$ and $b = 0.83 \pm 0.27$. The maximum concentration in the magnitude band $5.5 \leq M \leq 5.9$ is found 250 days before the earthquake, but the concentration 10 days before the earthquake is also high but lower than the maximum and, in the fit, has been used as the objective maximum extracted by the code. So, we can suppose that there may be some anomalies related to the earthquake, but the "anomaly definition" employed is too weak to extract all possible seismo-induced phenomena, consequently including many anomalies not related to earthquakes.

To improve the anomaly definition, we introduce the analysis of frequency content in the investigated window with the same approach as that one used for the magnetic field data. As can be seen in Figure 4, the significance of the results is improved for most of the analyses, passing the statistical criteria ($d \geq 1.5$ and $n \geq 4.0$). We note that, for the shorter period analysis in the symmetrical period from $-$500 days to 500 days with respect to the earthquake, the maximum concentration of the anomalies is post-seismic, and for the analysis in the signal period range between 10 s and 25 s from $-$90 days to 30 days, the maximum concentration is a "co-seismic" effect. Even if statistically significant, these

results do not contribute to the main purpose of this paper, i.e., a better understanding of the preparatory phase of medium-large earthquakes. On the other hand, the investigation in the lower frequency band in which the longest period is equal to 25–50 s shows not only highly significant results but also pre-seismic maximum concentrations of anomalies both for the investigation in the time window from −90 days to 30 days and for the one from −500 days to 500 days at about −59 days and −290 days, respectively (see Table S2). Such a result seems to indicate that taking the frequency content of the anomalies into account could help to discriminate the ones possibly caused by the preparation phase of earthquakes from the other ones caused by other phenomena.

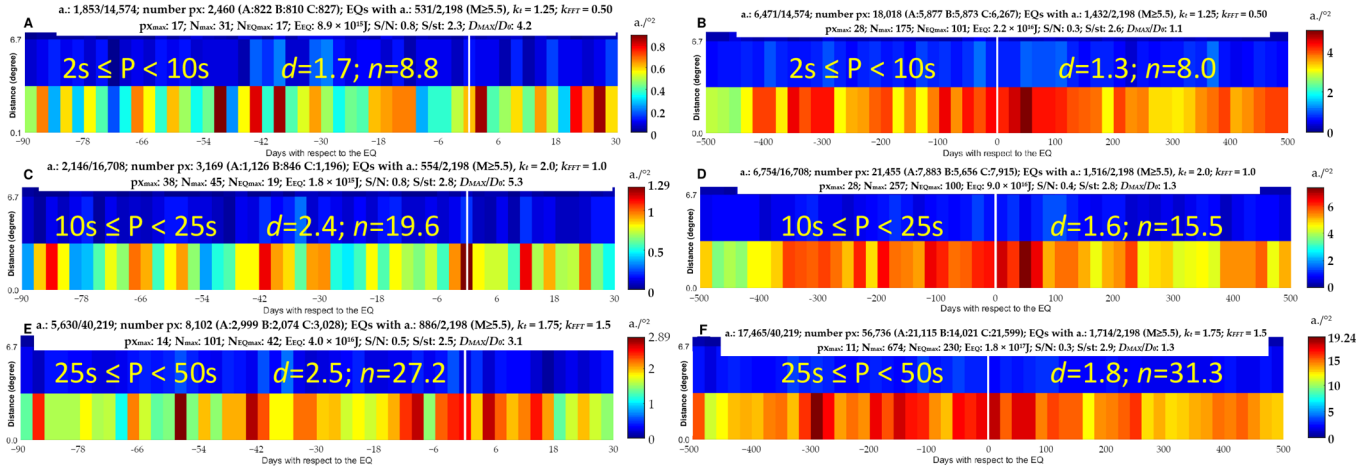

Figure 4. 8-year *Swarm* Ne data WSC analyses separated for frequency content in the anomalies correlated with M5.5+ earthquakes for 120 days (left) and 1000 days (right) around the EQ occurrence, in particular: (**A**) signal period from 2 s to 10 s and analysis from −90 days to +30 days with respect to the earthquake, (**B**) signal period from 2 s to 10 s and analysis from −500 days to +500 days with respect to the earthquake, (**C**) signal period from 10 s to 25 s and analysis from −90 days to +30 days with respect to the earthquake, (**D**) signal period from 10 s to 25 s and analysis from −500 days to +500 days with respect to the earthquake, (**E**) signal period from 25 s to 50 s and analysis from −90 days to +30 days with respect to the earthquake, and (**F**) signal period from 25 s to 50 s and analysis from −500 days to +500 days with respect to the earthquake. The color bar represents the density of the anomalies in terms of the number of anomalies per square degree.

Finally, Table S2 (in the Supplementary Materials) reports the main statistical parameters for all the performed analyses for 8 years of *Swarm Ne* data. The statistically significant results (i.e., the ones with $d \geq 1.5$ and $n \geq 4.0$) that precede the earthquake are underlined in green, as in Table S1. It is possible to note that just three out of sixteen results for *Ne* passed these criteria. Despite this, introducing the analysis of the signal frequency provides more significant results in the lowest frequency band (i.e., the period between 25 s and 50 s).

4. Discussion

4.1. General Comparison for Magnetic Field and Ne Results

Comparing the results of the electron density and magnetic field measured aboard the satellite, it is possible to note that the *Swarm Ne* results are not statistically significant. One reason for this could be the large corresponding number of detected anomalies, which is about 80,000. It will be interesting in future works to apply the same technique to CSES data, as, due to the satellite's Sun-synchronous orbit, it would permit to have *Ne* deep local nighttime (02:00 LT) data, always avoiding the effects of the solar irradiation (for example after sunset, when the ionosphere can show perturbation even until midnight or little later [38]). Therefore, the fixed local time reduces the signal variation in *Swarm* due to its gradual orbital precession. In addition, the crossing of critical local times close to

the terminator can create perturbations or even false anomalies due to the shadow/light passage of the *Swarm* satellite along the same orbit.

Swarm satellites show better results for the magnetic field. This could be due to the intrinsically higher quality of magnetic instrumentation in comparison with that of Electric Field Instruments and to the satellite design (in particular, the star cameras on the same optical bench as the fluxgate magnetometers). Physically, this could also be explained as the magnetic field is usually less affected by the local time than *Ne*. Hence, its precession in *Swarm* satellites (see the discussion above) seems not to affect the usability of its measurements to search for possible pre-earthquake ionospheric disturbances.

In addition, a specific comparison of the coefficients found by the empirical Rikitake law in this work for the *Swarm* magnetic field and electron density data and the ones found by De Santis et al. [29] is provided in Figure S9 of the Supplementary Materials. We confirm the previous results and find that almost all the results are within the trend proposed in 1987 by Rikitake [37] for earthquake precursors of the quasi first kind (i.e., earth-currents, resistivity, radon, underground water, and other geochemical elements) or only the geomagnetic precursor (from the ground). This result is promising because it means that, with the availability of new satellite data, we are confirming an empirical trend obtained decades ago for ground precursors and extending its validity to ionospheric precursors, as recently found in De Santis et al. [29].

4.2. Validation of the Results by Confusion Matrix Performance Evaluation and ROC Curves

The results have been evaluated by the so-called "confusion matrix", which is a table of two rows × two columns used to assess the performances of a prediction model, crossing the presence (or not) of an ionospheric anomaly followed (or not) by an earthquake in the given time within the pre-chosen distance and time.

Here, we considered the same anomalies presented in the results, but we evaluated a cell that has 6° geomagnetic latitude for 6° geographic longitude and 2.4 days (for investigations previously conducted 90 days before the earthquake) or 20 days (for investigations conducted 500 days before the earthquake). The evaluation of the cell has been selected among the classic four cases:

1. True positive (*TP*): in the cell, there is at least an anomaly, and an earthquake follows within the next 90 days
2. True negative (*TN*): in the cell, there are no anomalies, and no earthquakes follow in the next 90 days in the same cell.
3. False positive (*FP*): in the cell, there is one or more anomalies, and no earthquakes follow in the next 90 days in the same cell
4. False negative (*FN*): in the cell, there are no anomalies, and an earthquake follows in the next 90 days.

From the evaluation of the number of true and false positives and negatives, the accuracy "*Acc*" has been computed as the total number of good cases over the total cases:

$$Acc = \frac{TP + TN}{TP + TN + FP + FN} \quad (5)$$

Better performance with respect to a random prediction is achieved when $Acc > 50\%$. We also calculated the Hit Rate (*HR*) and False Positive Rate (*FR*); the former expresses the percentage of predicted events, while the latter is the rate of false alarms:

$$HR = \frac{TP}{TP + FN} \quad FR = \frac{FP}{FP + TN} \quad (6)$$

An ideal prediction system would give the limit case with $HR = 100\%$ (all events are predicted) and $FR = 0\%$ (no false alarms), while a real system is better as close as possible to such limit case, and, typically, the earthquake prediction systems are not suitable for

use with the population when the false positive rate is too high. Finally, the Alarmed Time-Space "*AT*" (also called the alarm rate in the literature [39]) has been estimated:

$$AT = \frac{TP + FP}{TP + TN + FP + FN} \quad (7)$$

This quantity is important to check that a good prediction is not just achieved regarding an analyzed space-time that is too large or even an entire space-time. For example, the affirmation that "*in the future, in the World, an M5.5+ earthquake will occur*" is surely true, but it is not a "prediction", because it does not predict the exact time, and the space domain is too large (the whole world). Given the same accuracy, a prediction is preferable with a lower *AT*. The alarmed time can also be compared with the number of positive cases (*TP* + *FN*) with respect to the total cases, as, even an ideal (so, perfect) prediction needs to alarm at least all of the space-time that any event occurred.

Table 1 reports the evaluation of performances in terms of confusion matrices for the *Swarm* magnetic field and electron density data considering 90 days and 500 days before the M5.5+ earthquakes. These tables reflect the analyses shown in Figures 1, 3, 4, S2, S4 and S5, even if we consider only the time before the earthquakes, as the confusion matrix is a tool to assess the prediction capability of a system, so only the ionospheric anomalies that preceded the earthquake can be "positively" evaluated. It is possible to note that all the analyses show a high accuracy, from 72% until 95%. Contrariwise, the hit rates tend to be rather low (i.e., from ~1% to ~19%), as several earthquakes are not preceded by anomalies in the considered interval of time, and, overall, several earthquakes did not show anomalies continuously in the 90 (or 500) days before their occurrence. The alarmed space-time windows are very low (i.e., around one or a few percent) for all the investigations with an alarm-window time of 90 days, and they are between 5.1% and 19.1% for the analyses performed in a time window of 500 days. Both the investigated time windows show alarmed times below the 50% threshold—in some cases, lower than 1%—which provide further evidence of the non-chance nature of the detected anomalies in relation to the following earthquakes. The accuracy is similar to that of a previous work performed on *Swarm* electromagnetic data and earthquakes but using a machine learning approach [40]. Furthermore, the overall performances reflected the previous considerations, with the scores for the magnetic field being generally better than those for the electron density. Further, better scores were always yielded when the frequency content of the signal was investigated, confirming that it is fundamental to take into account the signal frequency of the possible electromagnetic ionospheric precursor in future studies.

In order to further statically check the predicting capability of the magnetic field and electron density anomalies extracted in this work as the best candidates for earthquake precursors by WSC, the Receiving Operating Characteristic (ROC) graph has been calculated. ROC is a well-established method to test a precursor candidate, e.g., [41], and it is a graph where the false positive rate is conventionally reported on the horizontal axis and the hit rate is reported on the vertical one. The diagonal from (0%, 0%) to (100%, 100%) represents the random case, while the upper-left corner (0%, 100%) is an ideal case that predicts all the events without any false alarm. A good prediction is required to be as far from the diagonal toward the ideal case as possible.

In our case, we extract all the anomalies identified as statistically significant in this work, i.e., the pre-earthquake concentrations that show a statistical coefficient $d \geq 1.5$ and $n \geq 4.0$, as previously used in this work and first defined by De Santis et al. [29]. In this section, other concentrations that are different from the absolute maximum one that passed this statistical criterion have been also taken into account. Collecting all the anomalies from the magnetic field and electron density *Swarm* data and all the techniques, we produced a new dataset of the best anomalies that contains 4831 *Swarm* anomalous signals after cleaning the overcounted ones.

With the new dataset of the best WSC anomalies, the "Confusion matrix" and ROC diagram have been evaluated and reported in Table 2 and Figure 5, respectively. The step

time of calculus has been set to be equal to the alerted time, and the window following the one with any *Swarm* electromagnetic anomaly is alerted if it contains any anomaly; otherwise, it is not alerted. Comparing Table 2 with Table 1, it is possible to fully confirm that the selections made in this paper extracted the statistically best pre-earthquake candidates permitted to reduce the false positive rate and increased the hit rate.

Table 1. Confusion matrices of the *Swarm* magnetic field and electron density anomalies identified in the 90 days or 500 days before the M5.5+ earthquakes.

			Magnetic Data		**Magnetic Data 2–10 s**		**Magnetic Data, 10–25 s**		**Magnetic Data, 25–50 s**	
			Earthquake		Earthquake		Earthquake		Earthquake	
			Yes	No	Yes	No	Yes	No	Yes	No
90 days before the earthquake	Anomalies	Yes	1396	25,654	573	9477	555	10,453	655	13,149
		No	50,454	1,091,776	51,277	1,107,953	51,295	1,106,977	51,195	1,104,281
	Hit and false positive rates		*HR* = 2.7%	*FR* = 0.23%	*HR*=1.11%	*FR*=0.85%	*HR* = 1.07%	*FR* = 0.94%	*HR* = 1.26%	*FR* = 1.18%
	Accuracy and Alarmed Time		*Acc* = 93.5%	*AT* = 2.31%	*Acc* = 94.8%	*AT* = 0.86%	*Acc* = 94.7%	*AT* = 0.94%	*Acc* = 94.5%	*AT* = 1.18%
			Earthquake		Earthquake		Earthquake		Earthquake	
			Yes	No	Yes	No	Yes	No	Yes	No
500 days before the earthquake	Anomalies	Yes	3255	19,575	1378	7826	1522	8800	1805	10,882
		No	15,325	102,965	17,202	114,714	17,058	113,740	16,775	111,658
	Hit and false positive rates		*HR* = 17.5%	*FR* = 16.0	*HR* = 7.42%	*FR* = 6.39%	*HR* = 8.19%	*FR* = 7.18%	*HR* = 9.71%	*FR* = 8.88%
	Accuracy and Alarmed Time		*Acc* = 75.3%	*AT* = 16.2%	*Acc* = 82.2%	*AT* = 6.52%	*Acc* = 81.7%	*AT* = 7.31%	*Acc* = 80.40%	*AT* = 8.99%
			***Ne* data**		***Ne* data 2–10 s**		***Ne* data, 10–25 s**		***Ne* data, 25–50 s**	
			Earthquake		Earthquake		Earthquake		Earthquake	
			Yes	No	Yes	No	Yes	No	Yes	No
90 days before the earthquake	Anomalies	Yes	1380	32,605	345	7984	434	7460	1100	16,156
		No	50,502	1,084,793	51,537	1,109,414	51,448	1,109,938	50,782	1,101,242
	Hit and false positive rates		*HR* = 2.66%	*FR* = 2.92%	*HR* = 0.66%	*FR* = 0.71%	*HR* = 0.84%	*FR* = 0.67%	*HR* = 2.12%	*FR* = 1.44%
	Accuracy and Alarmed Time		*Acc* = 92.9%	*AT* = 2.91%	*Acc* = 94.9%	*AT* = 0.71%	*Acc* = 95.0%	*AT* = 0.68%	*Acc* = 94.3%	*AT* = 1.48%
			Earthquake		Earthquake		Earthquake		Earthquake	
			Yes	No	Yes	No	Yes	No	Yes	No
500 days before the earthquake	Anomalies	Yes	3436	23,490	949	6744	1039	6101	2311	11,662
		No	15,164	99,030	17,651	115,776	17,561	116,419	16,289	110,858
	Hit and false positive rates		*HR* = 18.5%	*FR* = 19.2%	*HR* = 5.10%	*FR* = 5.50%	*HR* = 5.59%	*FR* = 4.98%	*HR* = 12.4%	*FR* = 9.52%
	Accuracy and Alarmed Time		*Acc* = 72.6%	*AT* = 19.1%	*Acc* = 82.7%	*AT* = 5.45%	*Acc* = 83.2%	*AT* = 5.06%	*Acc* = 80.2%	*AT* = 9.90%

Table 2. Confusion matrices of the best *Swarm* magnetic field and electron density anomalies identified in the WSC concentrations that passed the statistical significance test (i.e., the ones with $d \geq 1.5$ and $n \geq 4.0$).

		Alerted Time of 90 Days		**Alerted Time of 500 Days**	
		Earthquake		Earthquake	
		Yes	No	Yes	No
Anomalies	Yes	564	1112	406	478
	No	800	29204	258	4618
Hit and false positive rates		*HR* = 41.35%	*FR* = 3.67%	*HR* = 61.15%	*FR* = 9.38%
Accuracy and Alarmed Time		*Acc* = 94.0%	*AT* = 5.29%	*Acc* = 87.2%	*AT* = 15.35%

The ROC curve in bold blue in Figure 5 is obtained after testing several alerted times from 10 days (lower left side) to 2500 days (upper side). Two black arrows have underlined the two alerted times of 90 and 500 days, and they correspond to the one used in Table 2 and are mostly selected in this paper. In the same figures, the Area Under the Curve (AUC) has also been represented as a black inclined hatch for the random case (i.e., the one under the diagonal equal to 50% for the definition) and as a red inclined hatch for the real best *Swarm* anomalies, estimated to be equal to 83.6%. So, the AUC of the real data is 1.67 times better than that of a random predictor, confirming that WSC applied to *Swarm* data is able to extract potential pre-earthquake ionospheric disturbances.

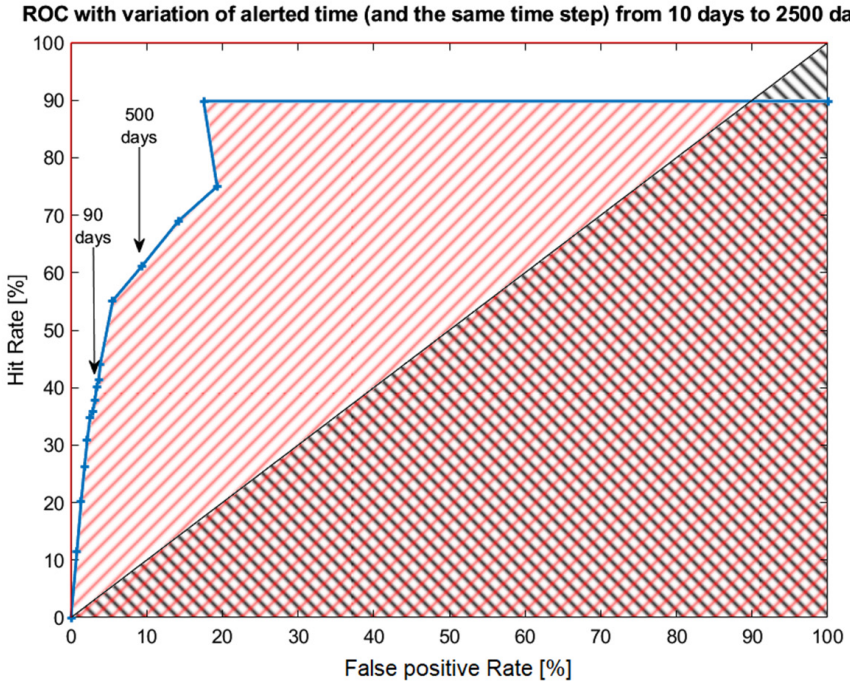

Figure 5. Receiving Operating Characteristic (ROC) graph for the best *Swarm* magnetic field and electron density anomalies (i.e., the ones in WSC concentrations with significant statistical parameters $d \geq 1.5$ and $n \geq 4.0$) calculated, varying the alerted time from 10 days to 2500 days. The Area Under the Curve (AUC) is represented as a black dashed pattern for a random case and as a red dashed pattern for the real *Swarm* case.

4.3. Improving the Superposed Epoch Approach by Taking into Account the Rikitake Law

The results of this paper, especially for the magnetic field anomalies, strongly confirm the empirical Rikitake law [37], which predicts that the logarithm of anticipation time linearly increases with earthquake magnitude. If such a law is true, then the superposed epoch approach would not work due to the mixing of several earthquakes with different magnitudes. It seems to work in the real case, but we think that this is due to the natural distribution of the earthquake magnitudes that follows the Gutenberg–Richter [42] earthquake distribution, privileging the smaller magnitude events. In this paper, we propose a new approach to addressing this issue when the epochs are superposed by "normalizing" the time scale using the Rikitike law, with the coefficients (a and b) being those proposed by De Santis et al. [29] for the *Swarm* magnetic field and electron density satellite data and referring to an M6.5 earthquake, following the next equation:

$$\Delta T' = \Delta T \cdot \frac{10^{(a+b \cdot 6.5)}}{10^{a+b \cdot M}} \tag{8}$$

where $\Delta T'$ is the normalized anticipation time, ΔT is the original time with respect to the earthquake, and M is the magnitude of the earthquake under analysis. Even if the formula can be, in principle, also applied to post-earthquake anomalies, we think that it is not proper to use it in such a way, as the formula is constructed on possible precursors. The reference magnitude (here, chosen as M6.5) can be, in principle, any magnitude, and the results are not affected by this choice. Its scope is to report the time in a different scale chosen as the number of days that preceded an M6.5 earthquake. M6.5 is an intermediate magnitude with a high number of events in the investigated period to be able to clearly show possible precursors, according to the results illustrated in this paper.

To select the window of analysis, we look at the results from [29] and plotted the expected anticipation time as a function of the earthquake magnitude (in Figure 6, as the orange curve). Based on these data, we decided to analyze 150 days before the earthquake

for the magnetic field data and 85 days for the *Ne* measurements (when $M = 6.5$, i.e., our reference point). We would underline that, using Equation (4), the analyzed time before the earthquake is not fixed (as in the previous analyses), but it is different for any earthquake as a function of its magnitude, and it is represented as the blue curve in Figure 6, i.e., the result of applying Equation (4)—that is, how many days the normalized time corresponds for other magnitudes. For example, the analyzed time before an M8.0 earthquake is 4037 days for the magnetic field (or 1576 days for *Ne*) according to Equation (4), and the time interval from 4037 days before and until the event will be compressed in the horizontal axis (of Figures 7 and 8) and shown to be equivalent to 150 days to 0 days of an M6.5 earthquake. We note that, for the magnetic field, the larger magnitude earthquakes (M > 8) could show an anticipation time that is greater than that of the 8 years of *Swarm* data available at the moment (the red dashed horizontal line in Figure 6).

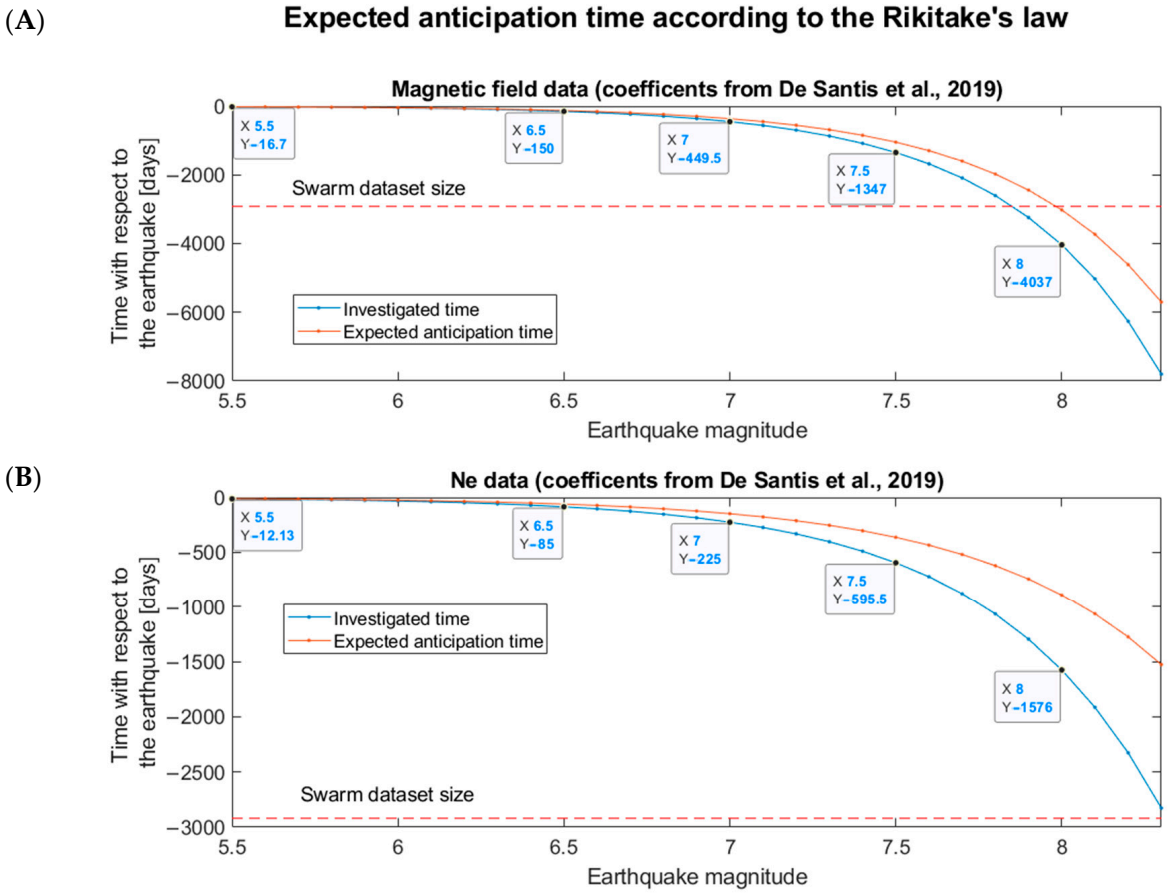

Figure 6. Expected anticipation time of magnetic field (**A**) and *Ne* (**B**) anomalies with respect to the earthquake, using the Rikitake law [37] and considering the coefficients found by De Santis et al. [29] for 4.7 years of *Swarm* data (orange line). The investigated time window is shown as a blue line, and the 8-year *Swarm* dataset maximum size is shown as a dashed red line. The data tips provide the time that has been analyzed before a specific magnitude earthquake, applying Equation (4).

We test and apply this approach to the most significant results of the *Swarm* data, which are the investigations of the magnetic field and *Ne* data with Method 1 and the *Swarm* magnetic field anomalies in the band of 2–10 s and the *Ne* anomalies in the band of 25–50 s, which are those with the best statistical indications from the previous analyses.

Figure 7 shows the results for the *Swarm* data without taking into account the frequency of the signal. The maximum concentration has a higher statistical significance with respect to the previous analyses: in fact, for the magnetic field data, d passes from 1.7 to 2.1, and for the *Ne* data, d passes from 1.3 to 1.5, which also means that, from a non-statistically

significant result, we obtain a higher significance with this different superposed time approach, which implies that we could better investigate the identified anomalies to search for seismo-ionospheric disturbances.

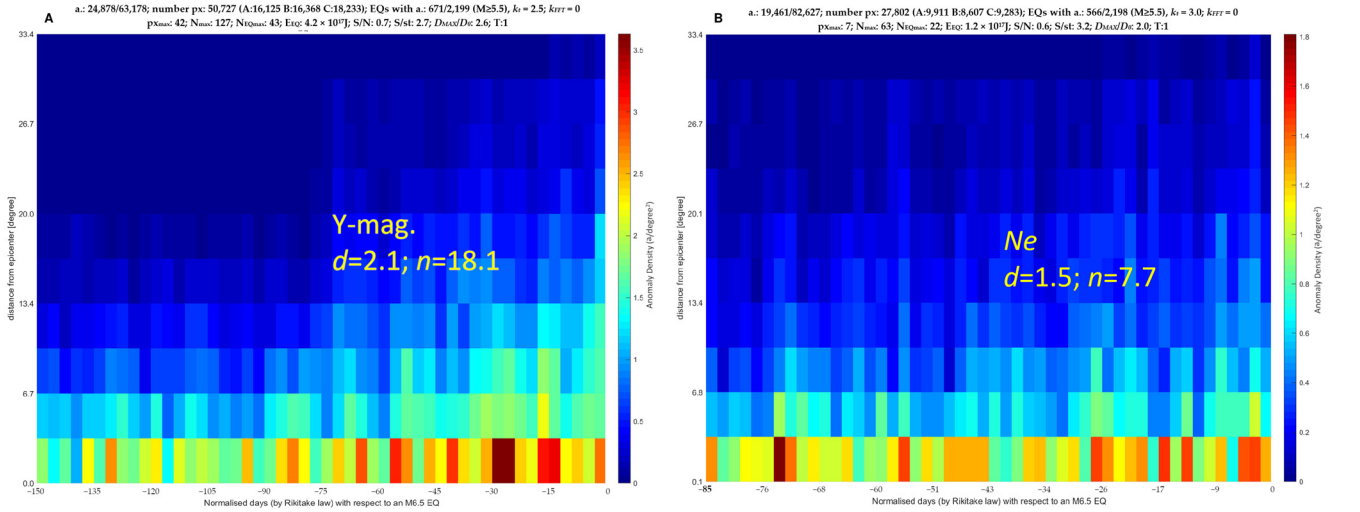

Figure 7. *Swarm* magnetic field data (Y-mag in (**A**)) and electron density (*Ne* in (**B**)) correlated with M5.5+ earthquakes using modified time according to the empirical Rikitake law.

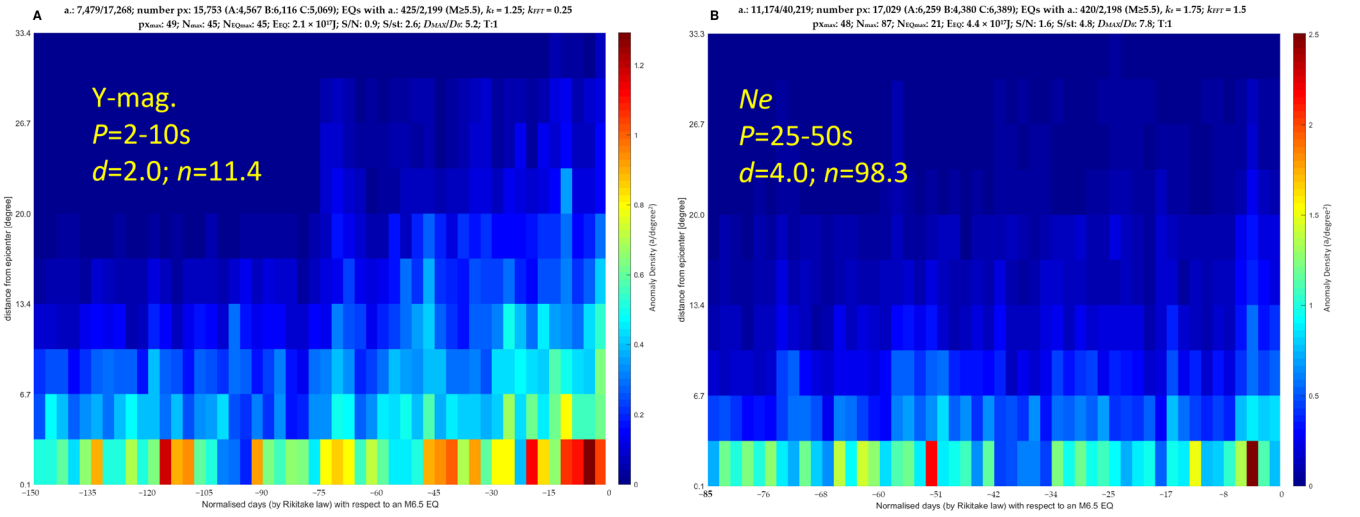

Figure 8. *Swarm* magnetic field data in the shorter period of 2–10 s (Y-mag in (**A**)) and electron density in the longer period of 25–50 s (*Ne* in (**B**)) correlated with M5.5+ earthquakes using modified time according to the empirical Rikitake law.

In the same way, in Figure 8, we apply this approach to the anomalies extracted by analyzing the frequency content of the magnetic field and *Ne* data. The frequency selected is the best from the previous analysis, so we obtained the magnetic field data in the quicker signal (2–10 s) and the *Ne* data in the slower signals (25–50 s). In this case, there is a general gain in the statistical improvements of both the *d* and *n* parameters (for the magnetic field data: *d* passes from 1.8 to 2.0, and *n* passes from 9.5 to 11.4; for the *Ne* data, *d* passes from 2.5 to 4.0, and *n* passes from 27.2 to 98.3, recording a very strong increase in statistical significance).

Finally, we underline that this approach seems very promising but requires a very large dataset. In fact, for the larger magnitude earthquakes, the whole time is not covered, even with 8 years of satellite data. On the other hand, for the visual inspection of the results, the immediate reading is lost with this approach: for example, the magnetic field data of

Figure 7A show several concentrations of anomalies between 75 days and 1 month before the M6.5 earthquakes, but such time corresponds to a different interval for any earthquake magnitude that can be estimated by Equation (4) and is represented in Figure 6A. However, as the empirical Rikitake law seems to describe the possible precursor well, it is fundamental to consider it and include it in a future prediction platform. In practice, detecting an anomaly can indicate a lower magnitude earthquake or a larger magnitude earthquake at a later time, and, if a lower magnitude earthquake does not happen immediately, after a number of days/weeks, the prediction can be adjusted, increasing the magnitude of the expected earthquake. Unfortunately, the larger number of false alarms (the anomalies not associated with any seismic events) makes it still impossible to implement such a prediction system.

4.4. Some Features of the Largest Concentrations

In the results shown in Figure 3, it seems to be observed that the content of the high frequency of the magnetic field signal of the possible earthquake precursor becomes more intense as the earthquake is approaching. There is not a simple explanation for this, and the present theories would suggest the contrary direction. From a seismological point of view, the crack dimension is supposed to increase toward the earthquake (e.g., [43,44]), the duration of the electromagnetic pulses eventually generated by the microfracture is supposed to be proportional to the crack dimension, and the emitted frequency is supposed to be proportional to the inverse of the pulse duration [6,7]. Even supposing that the fault is simplified as a two planar faces capacitor forming an oscillating circuit with the resistance and inductance of the ground (it can be the fluid patches in the rocks that act as a "transmission line" for the higher conductivity of fluids), the frequency "ω" is supposed to decrease with the crack size "*l*", which increases (a similar calculus that found that $\omega \propto \frac{1}{l}$ is provided by Kachakhidze et al. [45] and Liperovsky et al. [21]). These calculations and theories would not support the result presented in this paper, as they point to the opposite conclusion. However, first of all, we think that the problem is really open. Furthermore, we are not sure that the electromagnetic disturbances observed in the ionosphere are directly produced on the fault, as other phenomena can act at the ground-lower atmosphere interface, as suggested by Kuo et al. [10,11], who simulated the formation of ionospheric disturbances with accumulation on the Earth's surface of positive-holes released from the crack in the fault or a very different and complex chain of processes that influence the ionosphere as a consequence of the global atmospheric electric circuit alteration induced by air ionization from radon release, as theorized by Pulinets and Ouzounov [16]. In the last two mechanisms, it would be very difficult for the frequency of the supposed generated signal to be related to any crack evolution model, so it would be complicated to predict if the frequency of the magnetic field signal can increase or decrease toward the earthquake occurrence. Further studies will be necessary both in theory and in the observations, as shown here.

We finally investigated if the earthquakes involved in the absolute maximum concentrations of Figure 3A–C share some common features, such as focal mechanism or the location of the hypocenter beneath the sea or the land. A similar investigation on the *Swarm Ne* data and on earthquake occurrences over sea or land has been reported by He et al. [46]. Even if the authors did not find a particular "preference" in such classification, they found a better correlation for higher magnitude events, as was also detected in the present work.

First of all, we found that the earthquakes that are associated with the three maximum concentrations in the different analyzed signal bands (146 EQs, 137 EQs, and 146 EQs, respectively) are actually different events (except for two that are shared in all three concentrations), so the increase in frequency toward the earthquake occurrence could be apparent, and it is possible that the frequency of the generated signal depends on other parameters such as those investigated in the following. Table 3 reports the number of earthquakes and their percentage in the specific class. The focal mechanism has been

checked, searching for the same earthquake in the global Centroid Moment Tensor (CMT) catalog [47,48] with a maximum tolerance of 2 min on the origin time, 2.5 on the magnitude estimation, and 2 degrees in the epicenter localization. Using one of the rake angles of the moment tensors solution, the focal mechanism has been classified as "reverse" (or "thrust") if $+20^\circ <$ rake $< +160^\circ$, "normal" if $-160^\circ <$ rake $< -20^\circ$, or "strike-slip" if $-20^\circ \leq$ rake $\leq +20^\circ$ or if $|\text{rake}| \geq 160^\circ$, following Cronin [49].

Table 3. Investigation of a possible relation with the focal mechanism with the recorded frequency of the magnetic field anomalous signals from the *Swarm* and sea or land epicenter location. The significant percentage of deviation from the standard earthquake distribution (i.e., the ones $\geq 5\%$ in their absolute value) are marked by bold numbers. Green (red) numbers represent positive (negative) deviation percentages with respect to the reference.

Focal Mechanism	Earthquakes with Anomalies in the Band 2–10 s	Earthquakes with Anomalies in the Band 10–25 s	Earthquakes with Anomalies in the Band 25–50 s	All the Earthquakes
strike-slip	**50 (35.2%) −10.1%**	54 (39.4%) +0.6%	**54 (37.2%) −5.0%**	846 (39.2%)
reverse	**67 (47.2%) +10.5%**	**62 (45.3%) +6.0%**	64 (44.1%) +3.4%	922 (42.7%)
normal	25 (17.6%) −2.8%	**21 (15.3%) −15.4%**	27 (18.6%) +2.8%	391 (18.1%)
Sea or land				
Land	**16 (11.0%) −35.2%**	24 (17.5%) +3.6%	**30 (20.6%) +21.5%**	372 (16.9%)
Sea	**130 (89.0%) +7.2%**	113 (82.5%) −0.7%	116 (79.5%) −4.4%	1827 (83.1%)

The classification for the focal mechanism and the sea/land localization of the epicenters has been reported in the last column of Table 3 and for all the earthquakes investigated in this study. Further, it needs to be taken as a reference to search for any deviations from these percentages. We report in green (positive) or red (negative) the deviation percentage with respect to the reference, and in bold, we underline the significant difference for the focal mechanisms. Faster signals (2–10 s) seem more likely (+10.5% with respect to their natural distribution) to be produced by reverse focal mechanism earthquakes at the expense of strike-slip ones (−10.1%). The signals with a period in the range 10–25 s seem less likely (−15.4% with respect to their standard distribution) to be produced by normal fault earthquakes, and for the slower signals, the deviation percentages are not greater than 5%, so they are not really significant. Unfortunately, the detected deviations are not statistically significant, and deeper research in the future will be necessary to understand whether the focal mechanism has no influence on the possible ionospheric electromagnetic earthquake disturbances or if our study is too limited to have a clear detection of such dependence. On the other side, land earthquakes are more likely to show lower frequency signals (from faster to slower frequencies, they are −32.2%, +3.6%, and +21.5%), and, complementarily, the sea earthquakes seem likely to produce faster signals (from faster to slower frequencies, they are +7.2%, −0.7%, and −4.4%), as the percentage shows a clear trend with significant deviations for the highest and lowest frequency signals.

Finally, we find that only two earthquakes (above 146 with anomalies in 2–10 s, 137 in 10–25 s, and 146 in 25–50 s) are common events to all of these concentrations, so the results of this analysis are related to different earthquakes, and it is not clear if the frequency of the eventual electromagnetic wave produced by a single earthquake changes with the time, while the focal mechanism seems to have a slight or null influence on the signal frequency, and the localization in sea or land seems to play an important role for the frequency of the anomalies.

4.5. General Comparison of the Number of "Pre-" and "Post-" Earthquake Anomalies

Finally, we provide an objective comparison of the number of anomalies detected before and after the earthquake with a symmetrical analyzed time in Table 4. In this

table, we provide the difference between the anomalies detected before and the ones detected after the earthquake. The percentage of such difference refers to the anomalies after the earthquake, and the uncertainty is estimated as the square root of the maximum number of anomalies. We consider the result significant if the difference is greater than the estimated uncertainty. A negative difference indicates that the number of anomalies detected after the earthquake is greater than the number of those detected before the earthquake. Normalization with respect to the total hours of geomagnetical quiet time is provided to take into account the possible imbalance in the investigated events due to our cut of the geomagnetic perturbed times (i.e., the ones when $|Dst| > 20$ nT and/or $ap > 10$ nT). The normalized quantities are provided in the second line of each cell with the label "Norm". Such imbalance due to geomagnetic activity can be due not only to sporadically geomagnetic storms but also to the different solar activity that was at a "minimum" at the beginning of the *Swarm* mission and is now in the increasing stage toward the next "maximum". The incomplete dataset in the first and last 500 days of analysis could enhance such a difference in the solar cycle. Most of the investigations have a significant differential number of anomalies that preceded the earthquake, supporting the hypothesis that some of these anomalies are induced by the preparation phase of earthquakes. The analysis with the higher percentage of pre-earthquake anomalies is the Y-East magnetic field in the period band of 2–10 s. Concerning the *Swarm Ne* anomalies in the period band of 25–50 s, we note a relatively high percentage considering the high number of total anomalies (40,219) compared with the result of the "Y, no-band". Furthermore, if we look at the general pattern, it is possible to suppose that the pre-seismic anomalies start about 400 days before the earthquake as the color of the concentration becomes darker (about orange, i.e., with a concentration of anomalies equal to or greater than seven anomalies/degree^2) until the earthquake and persists until about 250 days after the earthquake, when it seems to go back at a background level (which shows a yellow color corresponding to about 5.5 anomalies/degree^2). We recognize that such investigations are biased by the fact that higher magnitude earthquakes tend to show anomalies ahead of time, but such earthquakes are fewer in number (according to the Gutenberg–Richter magnitude distribution [42]), so most of the weight on the anomalies is posed by lower magnitude events. Even if 8 years of data seems like quite a long time, only a longer satellite dataset could help to better investigate this aspect. For this reason, we would like to underline the importance of maintaining the orbiting of the *Swarm* constellation (and other missions equipped with magnetometers, such as CSES) for as long as possible.

Table 4. Comparison of the number of anomalies in the closer bin to the epicenter before and after the earthquake for the symmetrical investigations (from −500 days to +500 days) of 8 years of *Swarm* data correlated with M5.5+ earthquakes by the WSC algorithm. A normalization ("Norm") is provided to take into account possible different geomagnetic activities occurring before and after each investigated event.

Parameter, Period Band	Anomalies before the Earthquake	Anomalies after the Earthquake	Difference of the Anomalies	Estimated Uncertainty	Is the Result Significant?
Y, no-band	16,630 Norm: 16,584	16,436 Norm: 16,481	194 (1.2%) Norm: 103 (0.6%)	129	No [1]
Y, 2–10 s	4959 Norm: 4953	4563 Norm: 4568	396 (8.7%) Norm: 385 (8.4%)	70	Yes
Y, 10–25 s	5078 Norm: 5066	4917 Norm: 4928	161 (3.3%) Norm: 137 (2.8%)	71	Yes
Y, 25–50 s	6297 Norm: 6273	5858 Norm: 5880	439 (7.5%) Norm: 392 (6.7%)	79	Yes
Ne, no-band	15,504 Norm: 15,469	15,618 Norm: 15,652	−114 (−0.7%) −182 (−1.2%)	125	Yes, but post-seismic

Table 4. *Cont.*

Parameter, Period Band	Anomalies before the Earthquake	Anomalies after the Earthquake	Difference of the Anomalies	Estimated Uncertainty	Is the Result Significant?
Ne, 2–10 s	3157 Norm: 3136	3337 Norm: 3360	−180 (−5.4%) Norm: −224 (−6.7%)	58	Yes, but post-seismic
Ne, 10–25 s	4661 Norm: 4669	4562 Norm: 4554	99 (2.2%) 114 (2.5%)	68	Yes
Ne, 25–50 s	13,033 Norm: 12,991	12,538 Norm: 12,579	495 (3.9%) Norm: 413 (3.3%)	114	Yes

[1] Such difference is not significant if we take into account the normalization, i.e., it could be due to unbalanced geomagnetic activity in the investigated period.

5. Conclusions

In this paper, we extended the work published by De Santis et al. [29] to a longer period (8 years) than that originally analyzed (4.7 years) of *Swarm* data correlated with M5.5+ shallow earthquakes. Here, we not only provide an analysis extended to the first 8 years of *Swarm* data but also introduce some new methodologies to improve the definition of the anomalies (by frequency analysis) and in terms of better investigation of the results—in particular, searching for possible influences of the seismo-tectonic context on the possible pre-earthquake electromagnetic signals. New methodologies and investigations are proposed to take into account the frequency of the signal and the different anticipation times of anomalies expected for several magnitude earthquakes. We found that several concentrations of ionospheric anomalies are statistically significant, well overpassing the given thresholds of $d \geq 1.5$ and $n \geq 4.0$—i.e., they are very much greater than the concentrations obtained from the space-time-homogenously-distributed anomalies, and we can infer that the earthquakes associated with such significant concentrations could be more likely "predicted", even if this is not the goal of the present work. By the ROC curve, we confirm that the anomalies selected by WSC and the aforementioned statistical criteria over "d" and "n" have predicting capabilities, showing an AUC that is 1.67 times better than that of a random predictor. Future studies could be oriented to filter the signals that are most prone to earthquake-induced anomalies (for example, Zhu et al. [50]) in order to better depict the signal "features" of possible seismo-induced phenomena in the ionosphere. Nevertheless, although such ionospheric pre-earthquake disturbances are still widely debated, there is some evidence, in the literature and in this paper, that they statistically exist.

Our main conclusions are:

1. The anticipation time "ΔT" of the anomaly increases with the magnitude of the incoming earthquakes following the Rikitake laws [37], with these specific coefficients being $\Delta T_{mag} = 10^{-0.96+0.51 \cdot M}$ and $\Delta T_{Ne} = 10^{-3.46+0.83 \cdot M}$ for the magnetic field "mag" and electron density data, respectively. The anticipation time of large earthquakes (M7.5+) seems to be some years before the event and has been detected.
2. The focal mechanism seems to have a small or null influence on the generated frequency of the possible pre-earthquake anomalies.
3. Earthquakes localized in the land areas tend to be preceded by lower frequency anomalous signals, while sea earthquakes are more likely to be preceded by faster signal anomalies.
4. The *Swarm* magnetic field signal anomalies generally show a better correlation with earthquakes than the electron density ones do.
5. A more selective set of parameters, achieved here by the investigation of the signal frequency, reduces the size of the anomaly dataset, and it is shown that the possible correlation with the seismic event has a higher statistical significance for both the magnetic field and *Ne* observations.
6. Frequency analysis seems to be fundamental in some cases: for electron density, we find a higher correlation with anomalies, with a signal period in the range of 25–50 s.

7. All the results in this paper have been tested with the "confusion matrix" approach, reaching an accuracy from 75% to 95% and an alarmed time-space from 0.7% to 19.1%. The real results show a predicting capability that is 1.67 times better than that of a random predictor, according to the AUC of the ROC curve, which further proves a prediction capability of the best detected ionospheric anomalies by WSC.

The future perspective of this work can include, but is not limited to, an improvement of the anomaly definition criteria and the extension to a larger dataset and to other satellites such as CSES-01. By the way, CNSA, together with the Italian Space Agency (ASI), is preparing a second CSES-02 satellite that is planned to be launched next year, forming the first-ever pair of satellites fully dedicated to searching for the possible ionospheric precursors of strong earthquakes.

Finally, we think that this study is fundamental to assessing the Lithosphere-Atmosphere-Ionosphere Coupling mechanism and for a future prediction system. Further, it integrates such kinds of studies with seismological investigations of the Earth's surface and chemical–physical analyses of the atmosphere (e.g., a preliminary comparison between magnetic anomalies and atmospheric surface temperature has been performed by Ghramy et al. [51]). So, as the earthquake is a complex phenomenon, by looking at all of the geo-layers together (as suggested in the "Geosystemics" approach by De Santis et al. [52]), it will be possible to better understand its physical features in its preparation phase and, hopefully, predict it one day.

Supplementary Materials: The following are available online at https://www.mdpi.com/article/10.3390/rs14112649/s1, Figure S1: Example of data processing to extract the anomaly, Figure S2: WSC applied to *Swarm* mag. from −500 to 500 days, Figure S3: WSC applied to *Swarm* mag. from −1000 days until the earthquake origin time, Figure S4: WSC applied to the shuffled magnitude earthquake catalog, Figure S5: Fit of anticipation time versus signal period, Table S1: Statistical evaluation of the results for the *Swarm* magnetic field, Figure S6: WSC applied to *Swarm Ne* with four different methods, Figure S7: WSC applied to *Swarm Ne* from −500 to 500 days, Figure S8: WSC applied to *Swarm Ne* in five earthquake magnitude bands, Table S2: Statistical evaluation of the results for the *Swarm Ne*, Figure S9: Comparison of the Rikitake law coefficients obtained in this work with the previous ones.

Author Contributions: Conceptualization, D.M. and A.D.S.; methodology, D.M., A.D.S. and S.A.C.; software, D.M., S.A.C. and M.S.; validation, S.A.C. and M.S.; formal analysis, D.M.; investigation, D.M.; resources, K.Z. and D.M.; data curation, D.M.; interpretation, D.M. and A.D.S.; writing—original draft preparation, D.M.; writing—review and editing, all authors; visualization, D.M.; supervision, A.D.S. and K.Z.; project administration, K.Z., D.M. and A.D.S.; funding acquisition, K.Z., D.M. and A.D.S. All authors have read and agreed to the published version of the manuscript.

Funding: This research was funded by the National Natural Science Foundation of China, grant number 41974084; the China Postdoctoral Science Foundation, grant number 2021M691190; the Italian Space Agency, grant number 2020-32-HH.0 (Limadou-Science+); the International Cooperation Project of the Department of Science and Technology of Jilin Province, grant number 20200801036GH; and the Italian Ministry of University and Research, grant number D53J19000170001 (Pianeta Dinamico—Working Earth).

Data Availability Statement: The *Swarm* satellite data are freely available from ftp and http servers (swarm-diss.eo.esa.int, last accessed on 3 January 2022). The USGS Earthquake catalog is freely accessible at https://earthquake.usgs.gov/earthquakes/map (accessed on 1 February 2022).

Acknowledgments: We warmly thank Francisco Javier Pavón-Carrasco for the software developed to analyze the *Swarm* data, and we would like to acknowledge Guido Ventura, Rita di Giovambattista, Loredana Perrone, Alessandro Piscini, Roger Haagmans, Giorgiana De Franceschi, Luca Spogli, Claudio Cesaroni, Ilaria Spassiani, and Matteo Taroni, who participated in some of the discussions about this work and its previous investigations carried out in the framework of the SAFE (SwArm For Earthquake study) ESA-funded project and in the following activities and projects.

Conflicts of Interest: The authors declare no conflict of interest. The funders had no role in the design of the study; in the collection, analyses, or interpretation of data; in the writing of the manuscript; or in the decision to publish the results.

Appendix A. Evaluation of the Declustering of the Earthquake Catalog on the Worldwide Statistical Correlation Results

This appendix is dedicated to evaluating how the decluster technique that was used to pre-process the earthquake catalog could have affected the results.

Determining if an earthquake is an isolated event or part of a seismic swarm or sequence—and, in this last case, discriminating between foreshocks, mainshocks, and aftershocks—has been always a very challenging topic for seismologists [53]. Very recent frontiers of seismology are even trying to evaluate in real-time if an earthquake is a foreshock or a mainshock by a traffic-light scheme based on the evaluation of the *b*-value of the Gutenberg–Richter distribution [54].

Declustering an earthquake catalog means the removal of the foreshocks and aftershocks in order to identify the "clusters" of seismicity led by the mainshock. The detection of the cluster is a difficult problem, and several approaches are available, such as that of Reasenberg [35] that we applied in this paper, which uses a radius around the event (a radius of 10 km for the present paper) and a time window to search for foreshocks (with 10 days in advance, for this paper) and aftershocks (in this paper: 20 days). If another earthquake is detected inside the space-time researched area, the same approach is applied until no other events are detected. The algorithm also takes into account the uncertainty of the earthquake localization that we selected from the values directly available in the USGS catalog. A different choice of such free parameters of the algorithm yields obviously different results. For example, in De Santis et al. [29], a shorter time window was used (1 day before and 10 days after), but we found that some events that occurred in the same tectonic context in a short time were not detected as the same cluster for such strict time windows; therefore, in the present work, we decided to use a slightly longer time window. As already presented in the discussion section, the statistical results are very consistent among the two works, demonstrating that, even with different decluster parameters in the Reasenberg approach and the slightly different earthquake catalog, the main results of our Worldwide Statistical Correlation (WSC) algorithm are not affected significantly. The reason for this is probably that, in the final WSC results, the bins are generally large in space (3.34°) and time (from 2.4 days to 20 days), so the low "space and time" resolution homogenizes the differences among the two declustered earthquake catalogs. Here, we want to explore how the results are affected by using another declustering technique—in particular, that provided by Urhammer [55]—or by using the original undeclustered catalog. More recent seismological techniques have been developed, such as the Epidemic-Type Aftershock Sequence (ETAS) model that was also applied to decluster earthquake catalogs [56]. The ETAS technique permits the obtention of the probability that an earthquake can trigger another one (or be triggered by another one) and also has some forecast capabilities [57]. ETAS declustering has been applied to global seismicity by Nandan et al. [58], but this is beyond of the scope of this paper (to test it by WSC). We propose, as a future improvement, the study of the ionospheric electromagnetic disturbances combined with the ETAS investigation of seismicity. Different decluster techniques have been compared by Mizrahi et al. [59] in terms of the Gutenberg–Richter parameters obtained after declustering the catalog and were also compared with the original catalog. From [59], it is possible to note that Reasenberg [35] and Urhammer [55] provide a different, non-superposed set of *a*- and *b*-values of the Gutenberg–Richter earthquake magnitude distribution, so we consider them as independent for the next test. We reanalyzed the *Swarm* magnetic field data presented in Figure 1 with the Urhammer declustered catalog and the earthquakes not declustered by associating all the anomalies to all the earthquakes (Method 1). In addition, we also propose Method 3 (maximum magnitude) to analyze the non-declustered catalog, as it could, in principle, provide similar results to a declustered catalog. In fact,

the declustering means extracting the mainshocks that have a higher magnitude than the foreshocks and aftershocks. So, associating the anomaly with the maximum magnitude earthquake could mean linking it with the mainshock. Contrariwise, we need to note that the seismic radius used by the decluster techniques tends to be very much smaller (e.g., 10 km) than the Dobrovolsky's radius used by our searching algorithm (e.g., ~600 km for M6.5), so it is not the same approach as that using the declustered catalog.

Figure A1 reports the results of the WSC applied to 8 years of *Swarm* magnetic field data and M5.5+ shallow earthquakes declustered by the above-mentioned techniques (on the left side: A and C) or not declustered (on the right side: B and D). In subfigure D, the method of "Max (magnitude)" has been applied to the WSC using the non-declustered earthquake catalog (i.e., the original one). It is possible to note that, in any case, some concentrations of anomalies at about 30 days and 80 days before the earthquake are underlined. Such evidence provides more proof that these concentrations are real and, furthermore, that they are not dependent on the way in which the earthquake catalog is treated. Comparing the two results with the declustered catalogs (subfigures A and C), it is possible to note that the results are very similar, even if the decluster technique is different. The pattern of concentrations is almost equal, with slightly differences, and the statistical significance is comparable. Even without declustering the earthquakes, some high-concentration bins are preserved, but such a choice leads to the overcounting of the anomalies with a value of 1.68 anomalies–EQ links over the number of anomalies associated with at least one earthquake. The overcounting is lower with the declustering by Reasenberg (1.36) [35] compared to that obtained by applying Urhammer's technique (1.41) [55], so even if the statistical significance in terms of d and n is a bit lower with Reasenberg [35], we think that such a technique is a better choice than that of Urhammer [55], as it has a lower overcounting of anomalies. Finally, the choice of the maximum magnitude with the non-declustered earthquake catalog confirms the other results; however, it also loses some seismic information that the declustering algorithm takes into account. In fact, this technique operates on a distance that, in several cases, goes behind the typical stress-interaction region between the earthquakes, as already mentioned above.

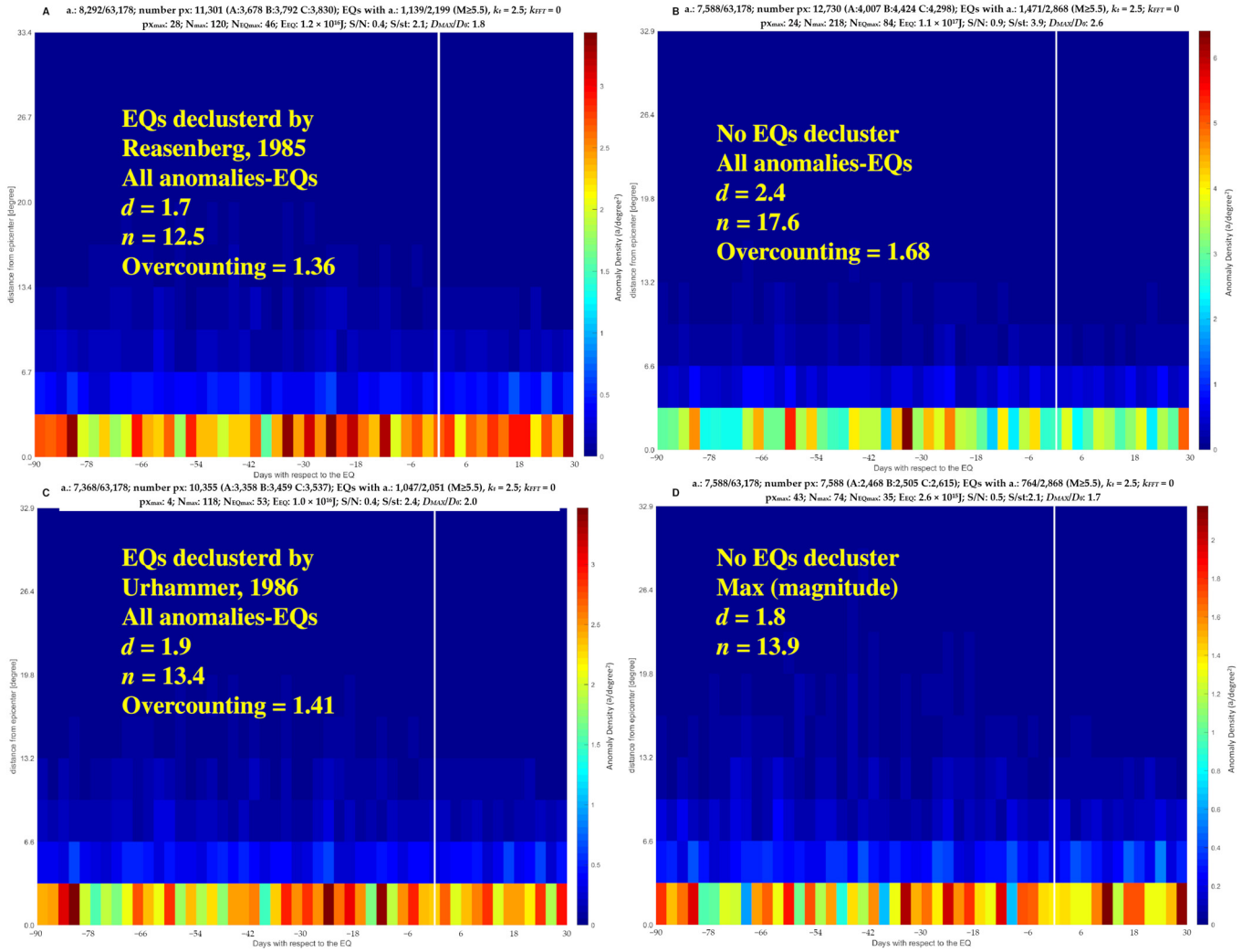

Figure A1. Comparison of the results of the Worldwide Statistical Correlation using two different declustering methods or by not declustering the catalog. The *Swarm* magnetic field data investigated from 90 days before the earthquake until 30 days after it are used for this example. The earthquake catalog has been declustered with: (**A**) Reasenberg, 1985 [35]; (**C**) Urhammer, 1986 [55]. The earthquake catalog used for the WSC of (**B**,**D**) has not been declustered. In (**A**–**C**), all anomalies have been assigned to any compatible earthquake, and the overcounting factor (the number of links between the anomalies and EQs divided by the number of anomalies with EQs) has been reported, while, in (**D**), each anomaly has been connected only to the higher magnitude earthquake among the possible ones (thus, there is no overcounting).

References

1. Rikitake, T. Classification of earthquake precursors. *Tectonophysics* **1979**, *54*, 293–309. [CrossRef]
2. Conti, L.; Picozza, P.; Sotgiu, A. A Critical Review of Ground Based Observations of Earthquake Precursors. *Front. Earth Sci.* **2021**, *9*, 676766. [CrossRef]
3. Picozza, P.; Conti, L.; Sotgiu, A. Looking for Earthquake Precursors From Space: A Critical Review. *Front. Earth Sci.* **2021**, *9*. [CrossRef]
4. Fraser-Smith, A.C.; Bernardi, A.; McGill, P.R.; Ladd, M.E.; Helliwell, R.A.; Villard, O.G., Jr. Low-frequency magnetic field measurements near the epicenter of the M_S7.1 Loma Prieta Earthquake. *Geophys. Res. Lett.* **1990**, *17*, 1465–1468. [CrossRef]
5. Molchanov, O.A.; Kopytenko, Y.A.; Voronov, P.M.; Matiashvili, T.G.; Fraser-Smith, A.C.; Bernardi, A. Results of ULF magnetic field measurements near the epicenters of the Spitak (M_s = 6.9) and Loma Prieta (M_s = 7.1) earthquakes: Comparative analysis. *Geophys. Res. Lett.* **1992**, *19*, 1495–1498. [CrossRef]
6. Molchanov, O.A.; Hayakawa, M. Generation of ULF electromagnetic emissions by microfracturing. *Geophys. Res. Lett.* **1995**, *22*, 3091–3094. [CrossRef]

7. Molchanov, O.; Hayakawa, M. On the generation mechanism of ULF seismogenic electromagnetic emissions. *Phys. Earth Planet. Inter.* **1998**, *105*, 201–210. [CrossRef]
8. Freund, F.T. Pre-earthquake signals: Underlying physical processes. *J. Southeast Asian Earth Sci.* **2011**, *41*, 383–400. [CrossRef]
9. Freund, F.; Ouillon, G.; Scoville, J.; Sornette, D. Earthquake precursors in the light of peroxy defects theory: Critical review of systematic observations. *Eur. Phys. J. Spec. Top.* **2021**, *230*, 7–46. [CrossRef]
10. Kuo, C.L.; Lee, L.C.; Huba, J.D. An improved coupling model for the lithosphere-atmosphere-ionosphere system. *J. Geophys. Res. Space Phys.* **2014**, *119*, 3189–3205. [CrossRef]
11. Kuo, C.-L.; Ho, Y.-Y.; Lee, L.-C. Electrical Coupling Between the Ionosphere and Surface Charges in the Earthquake Fault Zone. In *Pre-Earthquake Processes: A Multidisciplinary Approach to Earthquake Prediction Studies*; John Wiley & Sons, Inc.: Hoboken, NJ, USA, 2018; pp. 99–124. [CrossRef]
12. Prokhorov, B.E.; Zolotov, O.V. Comment on "An improved coupling model for the lithosphere-atmosphere-ionosphere system" by Kuo et al. [2014]. *J. Geophys. Res. Space Phys.* **2017**, *122*, 4865–4868. [CrossRef]
13. Kuo, C.-L.; Lee, L.-C. Reply to comment by B. E. Prokhorov and O. V. Zolotov on "An improved coupling model for the lithosphere-atmosphere-ionosphere system". *J. Geophys. Res. Space Phys.* **2017**, *122*, 4869–4874. [CrossRef]
14. Denisenko, V.V.; Boudjada, M.Y.; Lammer, H. Propagation of Seismogenic Electric Currents Through the Earth's Atmosphere. *J. Geophys. Res. Space Phys.* **2018**, *123*, 4290–4297. [CrossRef]
15. Denisenko, V.V.; Nesterov, S.A.; Boudjada, M.Y.; Lammer, H. A mathematical model of quasistationary electric field penetration from ground to the ionosphere with inclined magnetic field. *J. Atmospheric Sol.-Terr. Phys.* **2018**, *179*, 527–537. [CrossRef]
16. Pulinets, S.A.; Ouzounov, D. Lithosphere–Atmosphere–Ionosphere Coupling (LAIC) model—An unified concept for earthquake precursors validation. *J. Asian Earth Sci.* **2011**, *41*, 371–382. [CrossRef]
17. Scholz, C.H.; Sykes, L.R.; Aggarwal, Y.P. Earthquake Prediction: A Physical Basis. *Science* **1973**, *181*, 803–810. [CrossRef]
18. Ventura, G.; Di Giovambattista, R. Fluid pressure, stress field and propagation style of coalescing thrusts from the analysis of the 20 May 2012 M_L5.9 Emilia earthquake (Northern Apennines, Italy). *Terra Nova* **2013**, *25*, 72–78. [CrossRef]
19. Fidani, C.; Orsini, M.; Iezzi, G.; Vicentini, N.; Stoppa, F. Electric and Magnetic Recordings by Chieti CIEN Station During the Intense 2016–2017 Seismic Swarms in Central Italy. *Front. Earth Sci.* **2020**, *8*, 536332. [CrossRef]
20. Marchetti, D.; De Santis, A.; D'Arcangelo, S.; Poggio, F.; Jin, S.; Piscini, A.; Campuzano, S.A. Magnetic Field and Electron Density Anomalies from Swarm Satellites Preceding the Major Earthquakes of the 2016–2017 Amatrice-Norcia (Central Italy) Seismic Sequence. *Pure Appl. Geophys.* **2019**, *177*, 305–319. [CrossRef]
21. Liperovsky, V.A.; Pokhotelov, O.A.; Meister, C.-V.; Liperovskaya, E.V. Physical models of coupling in the lithosphere-atmosphere-ionosphere system before earthquakes. *Geomagn. Aeron.* **2008**, *48*, 795–806. [CrossRef]
22. Parrot, M.; Li, M. Demeter results related to seismic activity. *URSI Radio Sci. Bull.* **2015**, *2015*, 18–25. [CrossRef]
23. Yan, R.; Parrot, M.; Pinçon, J.-L. Statistical Study on Variations of the Ionospheric Ion Density Observed by DEMETER and Related to Seismic Activities. *J. Geophys. Res. Space Phys.* **2017**, *122*, 12421–12429. [CrossRef]
24. Ouyang, X.Y.; Parrot, M.; Bortnik, J. ULF Wave Activity Observed in the Nighttime Ionosphere Above and Some Hours Before Strong Earthquakes. *J. Geophys. Res. Space Phys.* **2020**, *125*, e2020JA028396. [CrossRef]
25. Zolotov, O.V. Ionosphere quasistatic electric fields disturbances over seismically active regions as inferred from satellite-based observations: A review. *Russ. J. Phys. Chem. B* **2015**, *9*, 785–788. [CrossRef]
26. Akhoondzadeh, M.; De Santis, A.; Marchetti, D.; Piscini, A.; Jin, S. Anomalous seismo-LAI variations potentially associated with the 2017 Mw = 7.3 Sarpol-e Zahab (Iran) earthquake from Swarm satellites, GPS-TEC and climatological data. *Adv. Space Res.* **2019**, *64*, 143–158. [CrossRef]
27. De Santis, A.; Marchetti, D.; Spogli, L.; Cianchini, G.; Pavón-Carrasco, F.J.; De Franceschi, G.; Di Giovambattista, R.; Perrone, L.; Qamili, E.; Cesaroni, C.; et al. Magnetic Field and Electron Density Data Analysis from Swarm Satellites Searching for Ionospheric Effects by Great Earthquakes: 12 Case Studies from 2014 to 2016. *Atmosphere* **2019**, *10*, 371. [CrossRef]
28. Marchetti, D.; De Santis, A.; Campuzano, S.A.; Soldani, M.; Piscini, A.; Sabbagh, D.; Cianchini, G.; Perrone, L.; Orlando, M. *Swarm* Satellite Magnetic Field Data Analysis Prior to 2019 Mw = 7.1 Ridgecrest (California, USA) Earthquake. *Geosciences* **2020**, *10*, 502. [CrossRef]
29. De Santis, A.; Marchetti, D.; Pavón-Carrasco, F.J.; Cianchini, G.; Perrone, L.; Abbattista, C.; Alfonsi, L.; Amoruso, L.; Campuzano, S.A.; Carbone, M.; et al. Precursory worldwide signatures of earthquake occurrences on Swarm satellite data. *Sci. Rep.* **2019**, *9*, 20287. [CrossRef]
30. De Santis, A.; Marchetti, D.; Perrone, L.; Campuzano, S.A.; Cianchini, G.; Cesaroni, C.; Di Mauro, D.; Orlando, M.; Piscini, A.; Sabbagh, D.; et al. Statistical correlation analysis of strong earthquakes and ionospheric electron density anomalies as observed by CSES-01. *Nuovo Cim. C* **2021**, *44*, 1–4. [CrossRef]
31. Friis-Christensen, E.; Lühr, H.; Hulot, G. *Swarm*: A constellation to study the Earth's magnetic field. *Earth Planets Space* **2006**, *58*, 351–358. [CrossRef]
32. Pinheiro, K.J.; Jackson, A.; Finlay, C.C. Measurements and uncertainties of the occurrence time of the 1969, 1978, 1991, and 1999 geomagnetic jerks. *Geochem. Geophys. Geosyst.* **2011**, *12*, Q10015. [CrossRef]
33. Yan, R.; Zhima, Z.; Xiong, C.; Shen, X.; Huang, J.; Guan, Y.; Zhu, X.; Liu, C. Comparison of Electron Density and Temperature From the CSES Satellite With Other Space-Borne and Ground-Based Observations. *J. Geophys. Res. Space Phys.* **2020**, *125*, e2019ja027747. [CrossRef]

34. Marchetti, D.; De Santis, A.; Shen, X.; Campuzano, S.A.; Perrone, L.; Piscini, A.; Di Giovambattista, R.; Jin, S.; Ippolito, A.; Cianchini, G.; et al. Possible Lithosphere-Atmosphere-Ionosphere Coupling effects prior to the 2018 Mw = 7.5 Indonesia earthquake from seismic, atmospheric and ionospheric data. *J. Southeast Asian Earth Sci.* **2019**, *188*, 104097. [CrossRef]
35. Reasenberg, P. Second-order moment of central California seismicity, 1969–1982. *J. Geophys. Res. Earth Surf.* **1985**, *90*, 5479–5495. [CrossRef]
36. Dobrovolsky, I.P.; Zubkov, S.I.; Miachkin, V.I. Estimation of the size of earthquake preparation zones. *Pure Appl. Geophys.* **1979**, *117*, 1025–1044. [CrossRef]
37. Rikitake, T. Earthquake precursors in Japan: Precursor time and detectability. *Tectonophysics* **1987**, *136*, 265–282. [CrossRef]
38. Song, R.; Hattori, K.; Zhang, X.; Liu, J.; Yoshino, C. Detecting the Ionospheric Disturbances in Japan Using the Three-Dimensional Computerized Tomography. *J. Geophys. Res. Space Phys.* **2021**, *126*, e2020ja028561. [CrossRef]
39. Shcherbakov, R.; Turcotte, D.L.; Rundle, J.B.; Tiampo, K.F.; Holliday, J.R. Forecasting the Locations of Future Large Earthquakes: An Analysis and Verification. *Pure Appl. Geophys.* **2010**, *167*, 743–749. [CrossRef]
40. Xiong, P.; Marchetti, D.; De Santis, A.; Zhang, X.; Shen, X. SafeNet: SwArm for Earthquake Perturbations Identification Using Deep Learning Networks. *Remote Sens.* **2021**, *13*, 5033. [CrossRef]
41. Fawcett, T. An Introduction to ROC analysis. *Pattern Recogn. Lett.* **2006**, *27*, 861–874. [CrossRef]
42. Gutenberg, B.; Richter, C.F. *Seismicity of the Earth and Associated Phenomena*, 2nd ed.; Princeton University Press: Princeton, NJ, USA, 1954.
43. McLaskey, G.C. Earthquake Initiation From Laboratory Observations and Implications for Foreshocks. *J. Geophys. Res. Solid Earth* **2019**, *124*, 12882–12904. [CrossRef]
44. Scholz, C. *The Mechanics of Earthquakes and Faulting*, 3rd ed.; Cambridge University Press: Cambridge, UK, 2019. [CrossRef]
45. Kachakhidze, M.K.; Kachakhidze, N.K.; Kaladze, T.D. A model of the generation of electromagnetic emissions detected prior to earthquakes. *Phys. Chem. Earth Parts A/B/C* **2015**, *85–86*, 78–81. [CrossRef]
46. He, Y.; Zhao, X.; Yang, D.; Wu, Y.; Li, Q. A study to investigate the relationship between ionospheric disturbance and seismic activity based on Swarm satellite data. *Phys. Earth Planet. Inter.* **2021**, *323*, 106826. [CrossRef]
47. Dziewonski, A.M.; Chou, T.-A.; Woodhouse, J.H. Determination of earthquake source parameters from waveform data for studies of global and regional seismicity. *J. Geophys. Res. Earth Surf.* **1981**, *86*, 2825–2852. [CrossRef]
48. Ekström, G.; Nettles, M.; Dziewoński, A. The global CMT project 2004–2010: Centroid-moment tensors for 13,017 earthquakes. *Phys. Earth Planet. Inter.* **2012**, *200*, 1–9. [CrossRef]
49. Cronin Vincent, S. A Primer on Focal Mechanism Solutions for Geologists. Lecture 11 of "OCEAN/ESS 410, Fall 2014 Marine Geology and Geophysics". 2010. Available online: https://www.ocean.washington.edu/courses/oc410/backgroundreading.html (accessed on 8 January 2022).
50. Zhu, K.; Fan, M.; He, X.; Marchetti, D.; Li, K.; Yu, Z.; Chi, C.; Sun, H.; Cheng, Y. Analysis of Swarm Satellite Magnetic Field Data Before the 2016 Ecuador (Mw = 7.8) Earthquake Based on Non-negative Matrix Factorization. *Front. Earth Sci.* **2021**, *9*, 621976. [CrossRef]
51. Ghamry, E.; Mohamed, E.K.; Abdalzaher, M.S.; Elwekeil, M.; Marchetti, D.; De Santis, A.; Hegy, M.; Yoshikawa, A.; Fathy, A. Integrating Pre-Earthquake Signatures From Different Precursor Tools. *IEEE Access* **2021**, *9*, 33268–33283. [CrossRef]
52. De Santis, A.; Abbattista, C.; Alfonsi, L.; Amoruso, L.; Campuzano, S.A.; Carbone, M.; Cesaroni, C.; Cianchini, G.; De Franceschi, G.; De Santis, A.; et al. Geosystemics View of Earthquakes. *Entropy* **2019**, *21*, 412. [CrossRef] [PubMed]
53. Jordan, T.H.; Chen, Y.-T.; Gasparini, P.; Madariaga, R.; Main, I.; Marzocchi, W.; Papadopoulos, G.; Sobolev, G.; Yamaoka, K.; Zschau, J. Operational Earthquake Forecasting—State of Knowledge and Guidelines for Utilization. *Ann. Geophys.* **2011**, *54*, 316–391. [CrossRef]
54. Gulia, L.; Wiemer, S. Real-time discrimination of earthquake foreshocks and aftershocks. *Nature* **2019**, *574*, 193–199. [CrossRef]
55. Uhrhammer, R. Characteristics of Northern and Central California Seismicity. *Earthq. Notes* **1986**, *57*, 21.
56. Console, R.; Jackson, D.D.; Kagan, Y.Y. Using the ETAS Model for Catalog Declustering and Seismic Background Assessment. *Pure Appl. Geophys.* **2010**, *167*, 819–830. [CrossRef]
57. Nandan, S.; Ouillon, G.; Sornette, D.; Wiemer, S. Forecasting the Rates of Future Aftershocks of All Generations Is Essential to Develop Better Earthquake Forecast Models. *J. Geophys. Res. Solid Earth* **2019**, *124*, 8404–8425. [CrossRef]
58. Nandan, S.; Kamer, Y.; Ouillon, G.; Hiemer, S.; Sornette, D. Global models for short-term earthquake forecasting and predictive skill assessment. *Eur. Phys. J. Spec. Top.* **2021**, *230*, 425–449. [CrossRef]
59. Mizrahi, L.; Nandan, S.; Wiemer, S. The Effect of Declustering on the Size Distribution of Mainshocks. *Seism. Res. Lett.* **2021**, *92*, 2333–2342. [CrossRef]

Remote Sensing of Environment 283 (2022) 113325

Contents lists available at ScienceDirect

Remote Sensing of Environment

journal homepage: www.elsevier.com/locate/rse

A comprehensive multiparametric and multilayer approach to study the preparation phase of large earthquakes from ground to space: The case study of the June 15 2019, M7.2 Kermadec Islands (New Zealand) earthquake

A. De Santis [a,*], L. Perrone [a], M. Calcara [a], S.A. Campuzano [b], G. Cianchini [a], S. D'Arcangelo [a,c], D. Di Mauro [a], D. Marchetti [d], A. Nardi [a], M. Orlando [a], A. Piscini [a], D. Sabbagh [a], M. Soldani [a]

[a] Istituto Nazionale di Geofisica e Vulcanologia, 00143 Rome, Italy
[b] Instituto de Geociencias IGEO (CSIC-UCM), 28040 Madrid, Spain
[c] Universidad Complutense de Madrid - UCM, 28040 Madrid, Spain
[d] College of Instrumentation and Electrical Engineering, Jilin University, 130061 Changchun, China

ARTICLE INFO

Edited by Jing M. Chen

Keywords:
Pre-earthquake anomalies
LAIC
Earthquake
Swarm satellites
CSES

ABSTRACT

This work deals with a comprehensive multiparametric and multilayer approach to study earthquake-related processes that occur during the preparation phase of a large earthquake. As a case study, the paper investigates the M7.2 Kermadec Islands (New Zealand) large earthquake that occurred on June 15, 2019 as the result of shallow reverse faulting within the Tonga-Kermadec subduction zone. The analyses focused on seismic (earthquake catalogs), atmospheric (climatological archives) and ionospheric data from ground to space (mainly satellite) in order to disclose the possible Lithosphere-Atmosphere-Ionosphere Coupling (LAIC). The ionospheric investigations analysed and compared the Global Navigation Satellite System (GNSS) receiver network with in-situ observations from space thanks to both the European Space Agency (ESA) Swarm constellation and the China National Space Administration (CNSA in partnership with Italian Space Agency, ASI) satellite dedicated to search for possible ionospheric disturbances before medium-large earthquakes, i.e. the China Seismo-Electromagnetic Satellite (CSES-01). An interesting comparison is made with another subsequent earthquake with comparable magnitude (M7.1) that occurred in Ridgecrest, California (USA) on 6 July of the same year but in a different tectonic context. Both earthquakes showed anomalies in several parameters (e.g. aerosol, skin temperature and some ionospheric quantities) that appeared at almost the same times before each earthquake occurrence, evidencing a chain of processes that collectively point to the moment of the corresponding mainshock. In both cases, it is demonstrated that a comprehensive multiparametric and multilayer analysis is fundamental to better understand the LAIC in the occasion of complex phenomena such as earthquakes.

1. Introduction

Earthquakes (EQs) release energies roughly proportional to 10^M, where M is their magnitude (e.g. Okal, 2019). The knowledge of the earthquake preparation process is a challenging task in the definition of the chain of events leading to the rupture. In case of large events, they are often made up of a sequence composed of foreshocks, mainshock and aftershocks (e.g. Mogi, 1963; Felzer et al., 2004). The recognition of all signals in the pre-seismic phase, with or without foreshocks, is the main task in earthquake prediction studies. Efforts have been made in real time foreshock phase recognition and, although some significant progress has been found in this field (e.g. McGuire et al., 2005; Gulia and Wiemer, 2019), some difficulties still remain (e.g. Dascher-Cousineau et al., 2020).

Even if one may usually consider a strategy based on seismic data analysis (e.g. De Santis et al., 2015; Cianchini et al., 2020), a non-seismic approach exists, based, for example, on the observation and detection of some anomalous behaviour of the above geolayers, i.e. atmosphere and ionosphere. This is simply justified by the fact that the lithospheric system under tectonic stress, including the earthquake preparation

* Corresponding author.
E-mail address: angelo.desantis@ingv.it (A. De Santis).

https://doi.org/10.1016/j.rse.2022.113325
Received 7 June 2022; Received in revised form 26 September 2022; Accepted 15 October 2022
Available online 28 October 2022

volume, is an open system, with, therefore, mass and energy exchange with neighbour environment, flowing, as an example, into the above atmosphere and, in turn, into the ionosphere, just during the preparation phase of the earthquake. This kind of interaction is also called Lithosphere-Atmosphere-Ionosphere Coupling (LAIC) (Hayakawa and Molchanov, 2002; Freund, 2011; Pulinets and Ouzounov, 2011). Usually, this approach takes advantage of the existence of dense ground observational networks and of currently orbiting satellites. These latter have the potential to have greater probability to be flying periodically over the seismic regions and detect any possible continuous or occasional precursors (e.g. Picozza et al., 2021).

Only recently, space missions were conducted and performed for the investigation of the circumterrestrial environment, with particular attention in observing and studying the possible coupling among solid earth, atmosphere, ionosphere and magnetosphere before strong earthquakes. The French DEMETER satellite (Parrot, 2002; Cussac et al., 2006) represented the very first attempt to put in low-Earth orbit a dedicated satellite for potential detection of ionospheric signals preceding strong earthquakes (e.g. Parrot, 2012). This satellite was flying from 2004 to 2010 and demonstrated to be able to monitor and detect ionospheric effects prior to large earthquakes (e.g. Zhima et al., 2020). Since 2013, the Swarm three-satellite mission by ESA is in progress to monitor the geomagnetic field at the best, taking advantage of the peculiar satellite orbital configuration: two satellites, Alpha and Charlie, fly at around 460 km of altitude while the third satellite, Bravo, flies at about 510 km. Its effectiveness to detect peculiar pre-earthquake anomalies of the magnetic field and electron density in the ionosphere has been lately studied and shown (De Santis et al., 2017, 2019b). The most recent space enterprise with the same objective has been the CSES-01 that was launched on 2 February 2018 and is still orbiting at about 500 km of altitude. Its on-board instruments represent the best nowadays to verify the possibility to observe anomalous behaviour of the ionosphere, possibly due to impending large earthquakes (Shen et al., 2018).

This study analyses multiparametric (seismic, atmospheric, Global Navigation Satellite System -GNSS and satellite) data trying to detect possible anomalies related to the M7.2 (as provided by GeoNet EQ catalogue, or M7.3 from USGS catalogue) Kermadec Islands (New Zealand) EQ, occurred on June 15, 2019 at 22:55:04 UTC, located at 30.644°S, 178.100°W and 46.0 km depth (USGS source: https://earthquake.usgs.gov/earthquakes/eventpage/us6000417i/executive). We also compare the results with the analogous findings of another recent seismic event, i.e. the M7.1 Ridgecrest EQ. (6 July 2019, California, USA; e.g. De Santis et al., 2020), whose open system character has been demonstrated in Pulinets et al. (2021) with the detection of an anomalous flux of radon, just days before the mainshock.

This paper is organized as follows. First, the used data are introduced, then the applied methods together with their main results are presented. Since this work is a comprehensive investigation of the EQ under study, the data analyses are made in the different geolayers from bottom to above, i.e. from lithosphere, atmosphere to ionosphere. All results are then combined and compared with those of the Ridgecrest EQ. We finally conclude with some discussion and conclusions. Although data and methods are different and heterogeneous, we attempt to provide a comprehensive and all-inclusive view of the found results, in the framework of the LAIC model. In addition, some Supplementary Material completes the work with further data analyses and results, complementary to those provided in the main text.

2. Data

In order to study the LAIC effects, several datasets are necessary. In fact, each geolayer that is investigated requires specific data from several sources. As the analysis is conducted separately in each layer, we cope with time/space different resolutions. However, the integration of the different results attempts to take into account these differences. Although some difficulties could be present to investigate the physics of the mechanism of coupling when the time or space resolution is limited, nevertheless the comparison with the results from several layers is still possible.

2.1. Lithospheric data

The seismic event under investigation was located in a very active region where one of the fastest plates (Pacific Plate) subducts beneath the Kermadec-Tonga subduction zone (Fig. 1a); here large earthquakes and volcanic eruptions are taking place (e.g. Smith and Price, 2006; D'Arcangelo et al., 2022).

The USGS catalogue (https://earthquake.usgs.gov/earthquakes/search/) and the national New Zealand catalogue, i.e. the GeoNet Earthquake Catalogue (https://www.geonet.org.nz/), were used in this study. The former catalogue has the advantage of having a global coverage due to a worldwide network of seismic stations and it has a magnitude of completeness (Mc) of about 4.5 worldwide (or even better in last years and for regions - e.g. in USA; Mueller, 2019). *Mc* is an important parameter when estimating *b*-values (Wiemer, 2000): *Mc* is the minimum magnitude for which, in a given region and temporal interval, all earthquakes with magnitude $M \geq Mc$ are recorded by the seismic network.

Since we are interested in a deeper understanding and characterisation of the specific region of New Zealand, for more detailed analyses and to achieve a lower magnitude of completeness, we retrieved the seismic data from the GeoNet site too, in the period between January 01, 2018 and June 14, 2019. The area is delimited by the Dobrovolsky strain radius (Dobrovolsky et al., 1979), that scales with magnitude M as $10^{0.43M}$ km, collecting around 18 thousand events. Although the seismic network is decentralised with respect to the epicentre (Fig. 1b), nonetheless the proximity of the northernmost station (GLKZ) assures a good detection capability in the area. The GeoNet earthquake catalogue permits to study more in detail the seismicity because the magnitude of completeness can reach 2.0, or even lower values: in particular it allows to search for some seismic "precursors" such as the variation of *b-value* (e.g. Herrmann et al., 2022) or some recognisable patterns, such as the seismic quiescence or its almost opposite, i.e. the *Accelerated Moment Release (*AMR), and its revised version, hence called R-AMR (*Revised Accelerated Moment Release;* De Santis et al., 2015). To this purpose, we downloaded the New Zealand seismic data from 2018 to the mainshock origin time in a broad region around the epicentre.

2.2. Atmospheric data

As the method of analysis is based on the comparison of the phenomenon's behaviour in the present time with that in the historical background, the downloaded data were analysed from the beginning of their availability until present, and every while we updated our archive with the most recent data. In particular, to investigate the atmosphere we retrieved several parameters, such as SKin Temperature (SKT), Total Column Water Vapour (TCWV), Outgoing Longwave Radiation (OLR), Aerosol Optical Depth (AOD), Carbon Monoxide (CO), Sulphur Dioxide (SO_2) and Methane (CH_4) from ECMWF (European Centre for Medium-range Weather Forecasts) and NASA-NOAA. Most of the data have been selected from climatological re-analysis datasets. These ones have the advantage of having a homogeneous coverage in space and time and to be only slightly altered by observation conditions, like cloud cover for satellite observations. ECMWF elaborated ERA-Interim from 1979 to 2019 and the new version ERA-5 with improvements such as temporal resolution of one hour (instead of 6 h of ERA-Interim) and more parameters and higher space resolution, updated to present in quasi-real time. NASA-NOAA elaborated the climatological model MERRA-2 (Gelaro et al., 2017). This model provides physical and chemical estimations of atmospheric conditions from 1980 to present (updated once per month). Temporal resolution is one hour and spatial resolution is

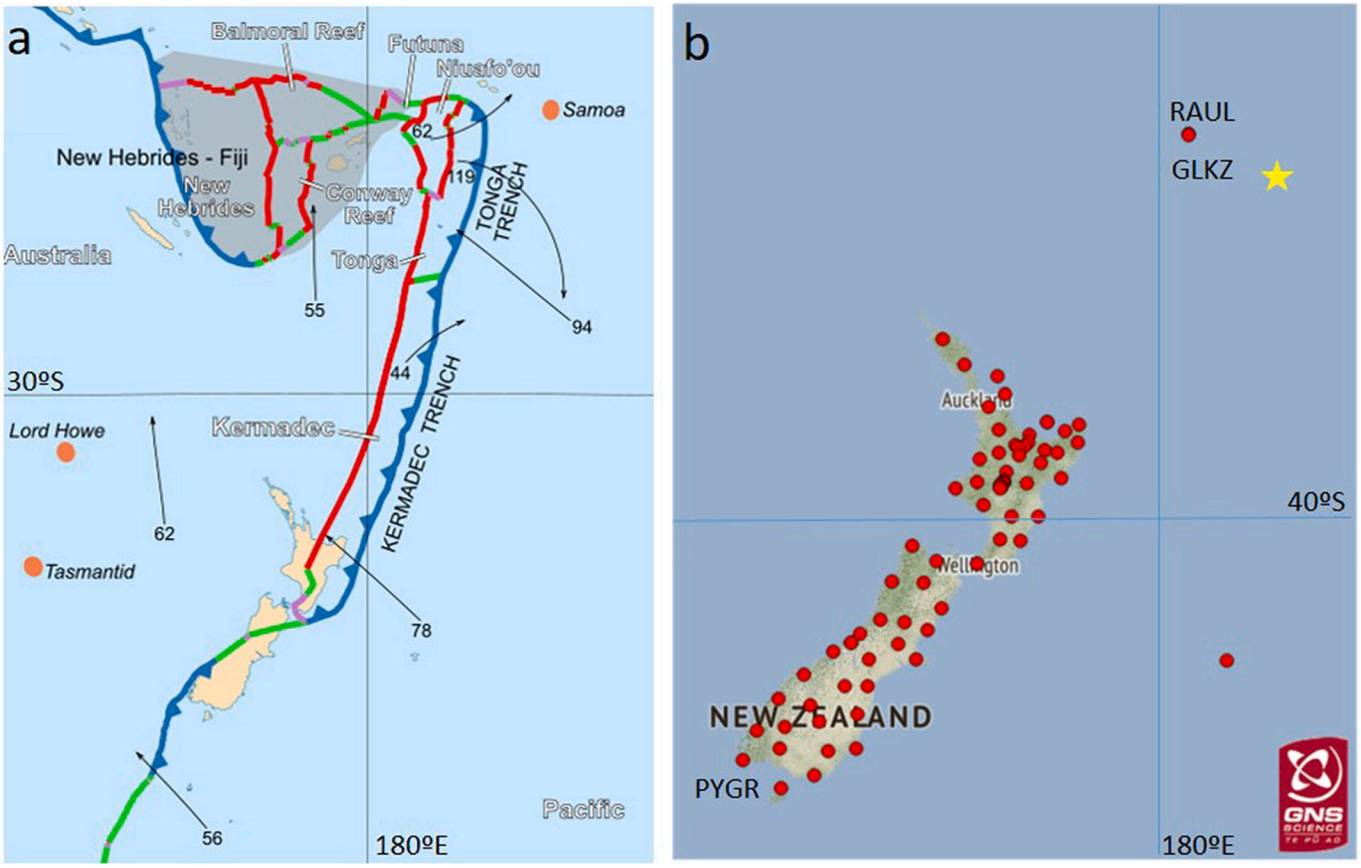

Fig. 1. (a) The Kermadec-Tonga subduction area, where the subduction direction and large velocities (the arrows and the associated velocities w.r.t. Africa in mm/yr) are evidenced. Tectonic margins are shown in red (diverging), green (transform), grey (orogens) and blue (subduction zones); red circles are seismographic stations on Islands (Image source: Wikipedia, under CC BY-SA 3.0); (b) Distribution of the seismographic stations in New Zealand: the northernmost station (GLKZ) is the closest one to the studied epicentre (Image source: GeoNet). Also two GNSS stations (RAUL, very close to the seismic station GLKZ, and PYGR) are shown: their TEC data have been used in our analysis. The yellow star shows the epicentre of the event. (For interpretation of the references to colour in this figure legend, the reader is referred to the web version of this article.)

0.625° longitude, 0.5° latitude. Both ERA-5 and MERRA-2 models were used to obtain the atmospheric parameters. We considered nighttime values because are typically less affected by local meteorological changes. The use of 40 years of data allows us to better evaluate the best background from which estimate the anomalies. The size of the geographical area investigated in the New Zealand region was determined by considering the circular earthquake preparation region (or Dobrovolsky area) centred in the earthquake epicentre (Dobrovolsky et al., 1979).

2.3. Ionospheric data

The ionospheric layer can be investigated in two ways: from in-situ observations by satellites (i.e. from satellites flying across ionosphere) and from ground observations by ionosondes and GNSS receivers. Our study addresses both approaches, mostly concentrating on CSES-01 satellite and integrating with ESA constellation Swarm three-satellites. The CSES-01 satellite is a multiplatform satellite whose main purpose is to search for ionospheric precursors of earthquakes, and for such reason it operates in "burst" mode over seismic active regions, i.e. seismic belts and China (Shen et al., 2018). We deeply investigated the plasma measurements (electron density, Ne and electron temperature, Te) from Langmuir Probes (LAP) and magnetic field measurements from High Precision Magnetometer (HPM) composed by two fluxgates and a Coupled Dark State scalar Magnetometer (CDSM) placed on one of the booms of the satellite. We also investigated the Search Coil Magnetometer (SCM) and Electric Field Detector (EFD) data from CSES-01. This satellite gives the possibility to have a good estimation of the background at two specific a.m. and p.m. local times due to its sun-synchronous orbit. For having a larger picture of the ionosphere at several local times, we integrated the magnetic field and plasma measurements from the Swarm constellation that is equipped with similar payloads with respect to CSES-01 satellite.

The CSES-01 HPM, LAP, SCM and EFD data were available at the CSES satellite web portal (www.leos.ac.cn). Regarding Swarm magnetic field data, they were downloaded as Level 1b low rate (1 Hz) data from all three satellites (up to baseline 0507) until 8 March 2020. For Swarm electron density data, we considered EFI LP (2 Hz), baseline 0501. Both datasets are provided in Common Data Format (CDF) and freely available in the ESA Swarm FTP and HTTP Server swarm-diss.eo.esa.int.

For the ground observations, we used GNSS data from the receivers of the GeoNet GNSS/GPS network (https://www.geonet.org.nz/), located within the earthquake preparation region, together with receivers outside the area of interest included for comparative analysis. The Total Electron Content (TEC), estimated from the time delay between two GPS (Global Positioning System) transmitting frequencies, can also be used to study the eventual effects in the ionosphere due to the preparation phase of strong earthquakes (e.g. Zhu and Jiang, 2020). By the other hand, a ionosonde has the advantage to determine important ionospheric parameters with the best precision, for example the altitude of the F2 layer, its limit-transmitting frequency, the eventual presence of the sporadic layer E, etcetera. Unfortunately, no ionosonde data are available from that area.

3. Data analyses and results

3.1. Seismological data analysis

The seismic data were retrieved from GeoNet Geological Information for New Zealand, in the period between 1 January 2018 and 14 June 2019 over a circular area contained by the Dobrovolsky strain radius, comprising 18,291 events. To characterise the seismicity trend, the first step was to calculate the magnitude of completeness (*Mc*). We computed *Mc* as a function of time by sliding the time window containing 150 earthquakes by steps of 5 events (Fig. 2a) and its variation in time in bold (grey lines are the upper and lower bands of confidence). Limits of the graph are set between 1 and 3, because it is the typical range of the *Mc* values from a dense seismic network.

Mc values of GeoNet network are quite stable and ranging between 1.8 and 2.2, for the time period considered. So, considering the largest value of the range, the catalogue was filtered in order to exclude all earthquakes with magnitudes lower than $Mc = 2.2$ and to obtain the *b-value* behaviour in time (Fig. 2b). The latter parameter depends on different physical and tectonic setting conditions: stress regime, heterogeneities of materials and temperature (Scholz, 2015). Low *b-values* have been correlated to asperity areas, possible origin of future earthquakes (e.g. Nanjo and Yoshida, 2021). From Fig. 2b it is worth noting a general tendence of decrease, with larger decrease at the end of 2018.

Accelerating seismicity is quite common during the preparation process of EQs. It can be detected by the Accelerated Moment Release (AMR) method, and its recent revised version (R-AMR; De Santis et al., 2015), applied to the EQ catalogue. The AMR method (e.g. Bowman et al., 1998; Bufe and Varnes, 1993) proposes that the cumulative value of the Benioff strain $s(t)$ (Benioff, 1949), which is proportional to the square root of the EQ energy, may progress following a power-law diverging function with time:

$$s(t) = \sum_{i=1}^{n(t)} \sqrt{E(t_i)} = A + B(t_f - t)^m \quad (1)$$

where $E(t_i)$ is the energy of the i-th event; $n(t)$ is the number of earthquakes at time t; $A \equiv s(t)_{|t=t_f} > 0$ at the time of failure t_f (i.e. the mainshock); $B < 0$ and $0 < m < 1$ are constant parameters, usually estimated by a non-linear least squares regression of data; m is an exponent representing the degree of accelerating energy release (De Santis et al., 2010), whose values usually are in the interval $[0.2, 0.6]$ (Mignan, 2011). The estimation of the acceleration is given by the so-called *C*-factor (Bowman et al., 1998), defined as the ratio between the root mean square (rms) of the residuals of the non-linear (power-law) fit and the root mean square of the linear fit:

$$C = \frac{rms_{nlin}}{rms_{lin}} \quad (2)$$

If C is <1, then acceleration is present, and the lower C, the more the acceleration occurs in the seismic data.

When focusing on the state of a specific fault, also the distance R_i of the i-th foreshock of the sequence from the mainshock plays an important role. De Santis et al. (2015) introduced a *revised* version of AMR (called R-AMR) to take into account the maximum distance R, supposing that the effects of preceding EQs are still perceived at the fault level, the so-called *minimum strain radius* (Dobrovolsky et al., 1979). The expression for the cumulative reduced strain becomes:

$$\underline{s}(t) = \sum_{i=1}^{n(t)} \sqrt{E(t_i)} \cdot G(R_i) \quad (3)$$

where $G(R_i)$ is an attenuation function depending on the distance R_i of the i-th EQ from the epicentre, modelled by De Santis et al. (2015) as

$$G(r) = \begin{cases} r^{-\gamma_0} & r \le R_0 \\ r^{-\gamma_1} & r > R_0 \end{cases} \quad (4)$$

where R_0 denotes the limit between two regions around the seismogenic fault, each with its own weighting exponent γ. By analysing 14 case studies worldwide, Cianchini et al. (2020) evidenced that γ_1 is generally equal to 0.5, while reasonably we set $\gamma_0 = 0$ (De Santis et al., 2015; Cianchini et al., 2020), because there is a small area around the epicentre with negligible attenuation.

The R-AMR estimates, in a sufficiently large area, the collective but surely different effect of each i-th EQ on the fault under study, according to its magnitude M_i and distance R_i from the fault. When we applied the R-AMR method (De Santis et al., 2015) to the downloaded catalogue, we observed that the seismicity accelerated during the preparation phase of the earthquake (Fig. 3). An automatic search for a significant acceleration was applied to seismic time series from the date before the EQ back to past values till C was <0.6. It is interesting to notice that the R-AMR detects a clear seismic acceleration ($C = 0.56$) when starting from middle June 2018 and predicts a magnitude similar to the real one (M(A) = 7.1 and M(B) = 7.4; see De Santis et al., 2015 or Cianchini et al., 2020 for their definitions) and a time of failure which is only around 20 days after the mainshock.

3.2. Atmospheric data analysis

In the LAIC approach, some atmospheric quantities and contents of gases have been simultaneously processed in order to identify possible persistent anomalies some days or months before the impending earthquake (Pulinets and Ouzounov, 2011). In particular, a Climatological Analysis for Seismic PRecursor Identification (CAPRI) algorithm (Piscini et al., 2017, 2019) has been applied to the ECMWF Reanalysis v5 (ERA5) and ECMWF Copernicus Atmosphere Monitoring Service (CAMS) climatological dataset with a spatial grid of 0.25° x 0.25°.

The time series of each atmospheric quantity has been collected and preprocessed in order to apply CAPRI algorithm which compares daily time series of the investigated year with the forty-year (1979–2018) historical time series in a temporal window of some months preceding

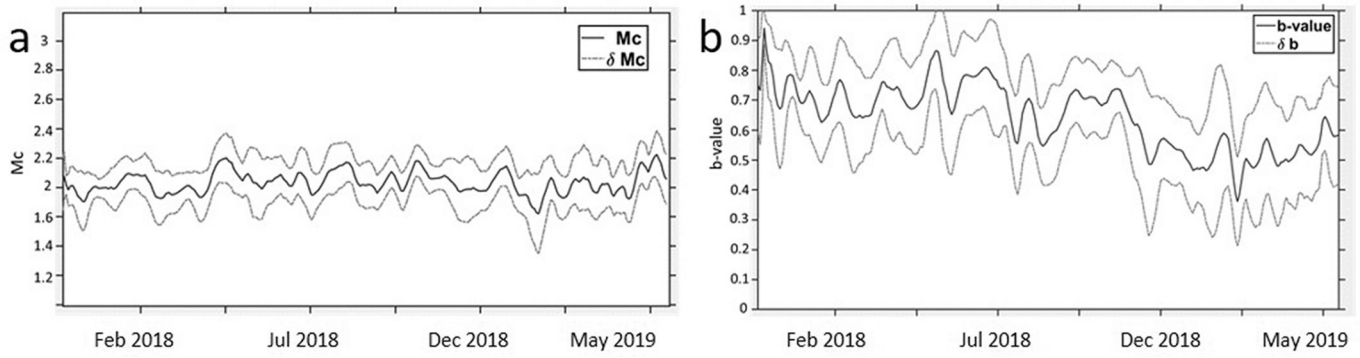

Fig. 2. Estimation of (a) Mc and (b) b-value in function of time with their bands of confidence for the earthquake of interest.

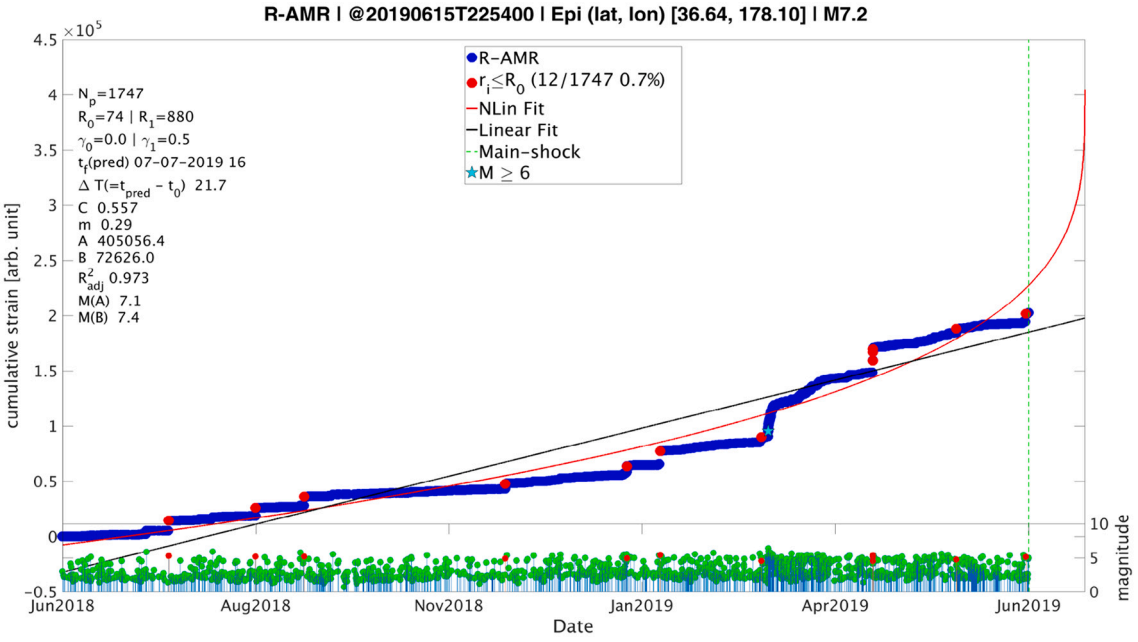

Fig. 3. The R-AMR analysis of the New Zealand catalogue around the 2019 M7.2 Kermadec Islands EQ. The algorithm evidenced an increased seismicity following a rather large foreshock (M > 6; shown as a cyan star) in March 2019, a few months before the mainshock. The figure shows also some parameters involved in the R-AMR analysis (see text for more details). (For interpretation of the references to colour in this figure legend, the reader is referred to the web version of this article.)

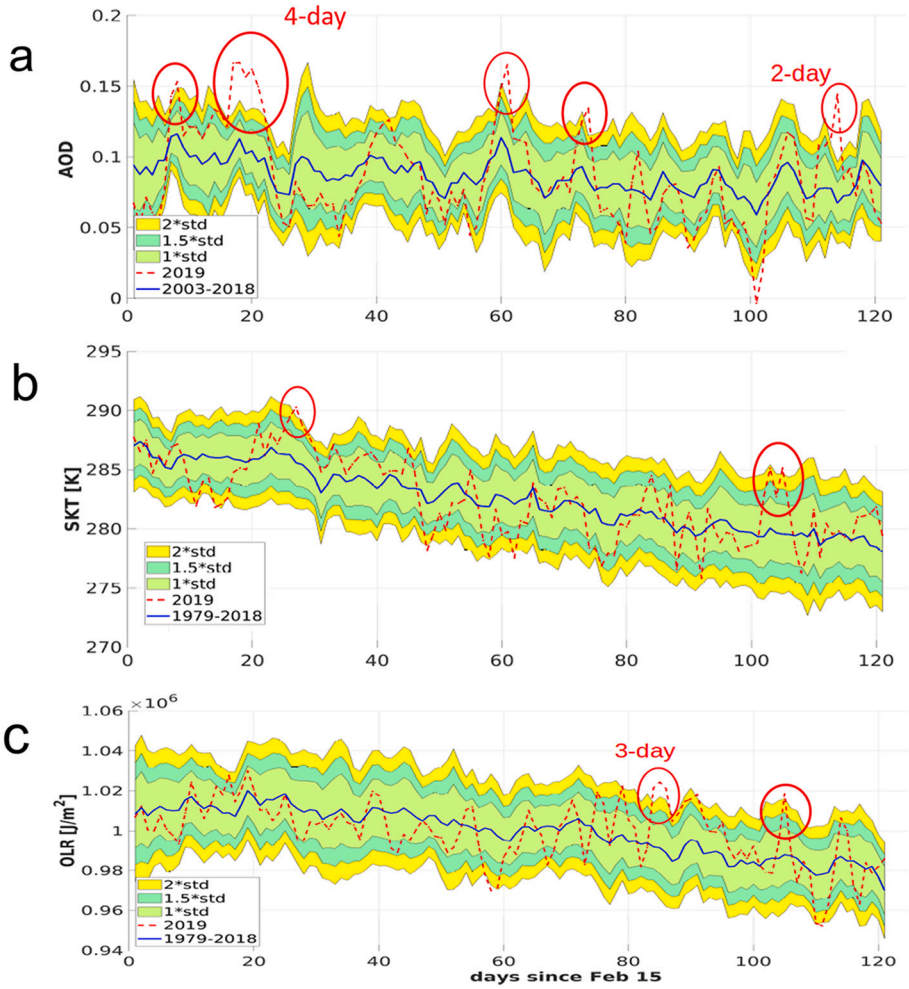

Fig. 4. Case study for the 2019 Kermadec Islands earthquake ECMWF AOD (a), SKT (b) and OLR (c). The 2019 time series (red dashed line) is compared with the historical time series (1979–2018 for SKT and OLR, 2003–2018 for AOD, blue line). The circles put in evidence the identified anomalous days. Coloured stripes indicate 1.0 (green), 1.5 (cyan) and 2.0 (yellow) times the standard deviation (std) from the mean of the historical time series, respectively. The earthquake occurred at the end of the analysed period (120 days). (For interpretation of the references to colour in this figure legend, the reader is referred to the web version of this article.)

the seismic event. If the observable of interest exceeds with a certain persistence the mean of the time series twice the standard deviation, an anomaly is identified. In this work we considered an interval of four months before the earthquake and preferred to identify also single day anomalies, at the cost to have more anomalies than usual.

In particular for ERA5 dataset, that starts from 1979, we focused on physical variables related to thermal radiative interaction of atmosphere with surface, i.e. SKT, TCWV and OLR. ERA5 provides hourly estimates of a large number of atmospheric, land and oceanic climate variables. The data cover the Earth's surface on a 30 km grid and resolve the atmosphere using 137 levels from the surface up to a height of 80 km.

As regard CAMS dataset, content of the main gases, possibly related to surface emissions (Chiodini et al., 2004, 2020), such as CO, SO_2, CH_4 and AOD, have been analysed, with the same 0.25° x 0.25° spatial grid resolution, with the exception of CO dataset that has a spatial resolution with a grid of 0.75° x 0.75°. The CAMS reanalysis dataset covers the period from January 2003 to 2020. We used all data from January 2003 to the date of the earthquake. The CAMS reanalysis is the latest global reanalysis dataset of atmospheric composition (AC) produced by CAMS, consisting of 3-dimensional time-consistent AC fields, including aerosols, chemical species and greenhouse gases (GHGs).

ECMWF climatological analysis for Kermadec Islands 2019 M7.2 seismic event puts in evidence some anomalous days for some of the studied parameters. In particular, AOD shows a 4-day persistent anomaly starting on 3 March 2019, and three single anomalies on 23 February, 17 April and 30 May 2019 (Fig. 4a), with positive anomalies around the epicentre (Fig. 5a). SKT shows two single anomalies on 13 March 2019 and on 30 May 2019 (Fig. 4b), with maximum concentration in northern New Zealand (Fig. 5b). OLR reveals a 3-day persistent anomaly starting on 9 May 2019 and two single anomalies on 15 and 30 May 2019 (Fig. 4c), with the EQ epicentre at the border between maximum and negative values (Fig. 5c). TCWV analysis shows three single anomalies, on 14 March, 31 March and 30 May 2019 (see Supplementary Material). As regards Sulphur dioxide content, it shows two anomalies on 11 April and 3 June (a two-day anomaly) 2019 with spatial concentrations as shown in the Supplementary Material. Methane shows three single anomalies on 10 March 2019, 23 and 25 May 2019, whilst CO analysis does not show any anomaly in the 120 day time window analysed (see Supplementary Material).

A confutation analysis performed for a year without significant

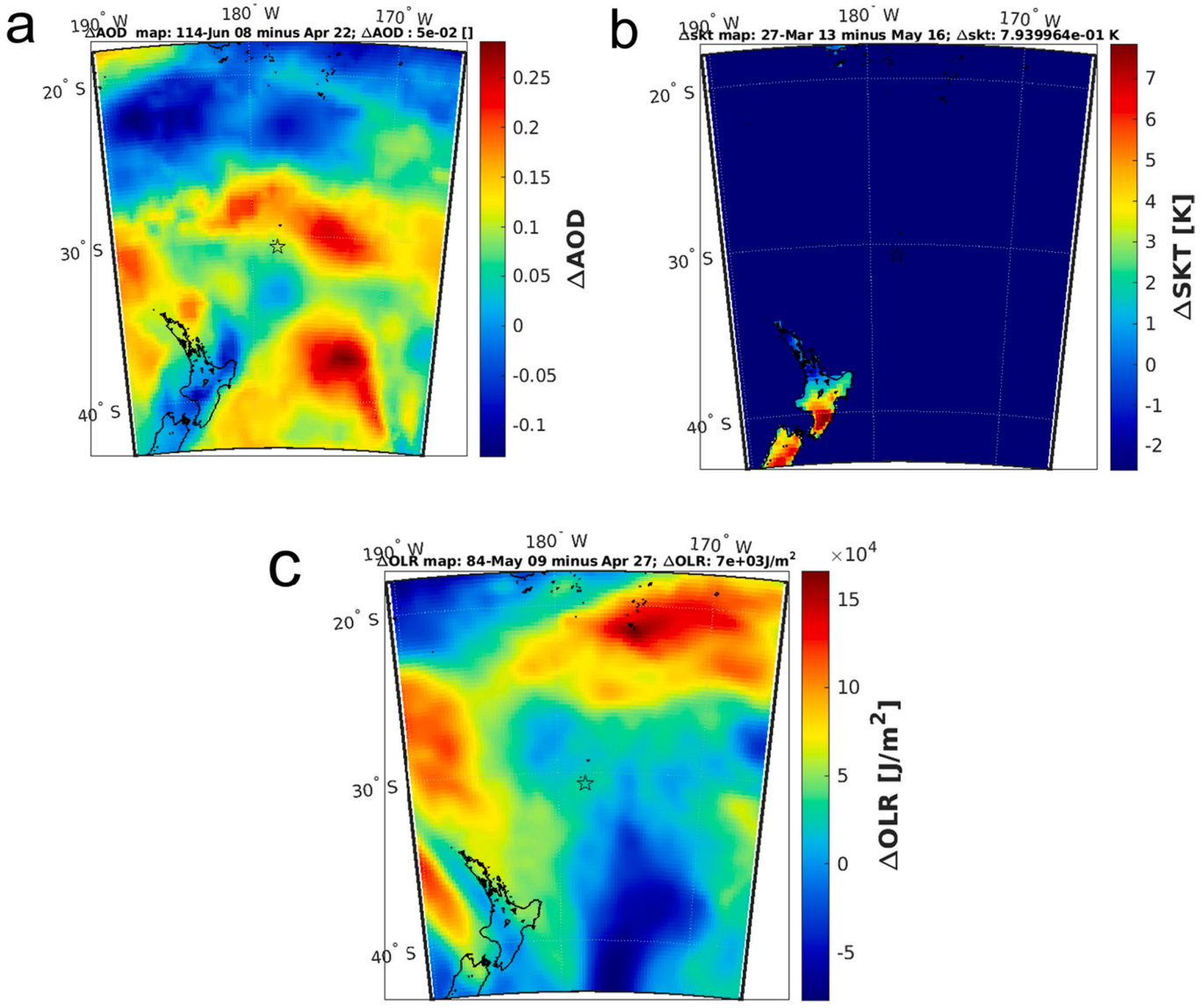

Fig. 5. ECMWF AOD (a), SKT (b) and OLR (c) anomalous day maps of the case study for the 2019 Kermadec Islands earthquake. The values are given as difference with respect to a typical non-anomalous day.

seismicity (i.e. 2018) is shown in the Supplementary Material where SKT and OLR do not show significant anomalies. AOD and SO_2 show many less anomalies than those detected by the same atmospheric quantities in 2019, i.e. the year of the EQ.

3.3. Satellite magnetic and electron density data analysis

After the analyses of lithospheric (i.e. seismological) and atmospheric data, we move to analyse the state of the ionosphere during the preparation of the Kermadec Islands EQ by satellites and GNSS receivers. Swarm and CSES-01 magnetic and Ne datasets are used to analyse and integrate the different approaches that can be implemented to detect electromagnetic anomalies caused by earthquakes preparation phase, thanks to their low earth orbits, at around 500 km of altitude. As shown in the Supplementary Material, starting from MASS (MAgnetic Swarm anomaly detection by Spline analysis; see for example De Santis et al., 2017, 2019b), four different approaches (hereafter also called Method 1, 2, 3 or 4, respectively) have been implemented: 1) classic MASS: using first differences divided by the time interval from sample to next sample and b-splines to remove the long trend; 2) using first differences of the data but removing the long trend by means of a 10-degree polynomial; 3) using the global geomagnetic field model CHAOS (i.e. a magnetic model initially based on **CHA**mp, **Ø**rsted and **S**ac-c satellites; the most recent version 7 also includes Swarm satellite data; Finlay et al., 2020), only for magnetic data, to calculate differences with respect to the satellite data and b-splines to remove the long trend; 4) using CHAOS model to calculate differences with respect to the satellite data and 10-degree polynomial to remove the long trend. The first approach (Method 1), i.e. the classic MASS, has the great advantage to be self-consistent, without the need of a global geomagnetic field model.

The main result of these analyses is a list of the most accurate and consistent anomalies that are provided by the classic MASS, being present in CSES-01 and Swarm magnetic tracks. This study has been performed considering 150 days before the EQ, detecting a promising anomaly 110 days (more than three months) before this event, present in different platform datasets. Fig. 6 shows an example acquired by CSES-01 and Swarm satellites on 25 February 2019. Fig. S11 in the Supplementary Material shows that the solar conditions before and during the found anomaly were quite calm, excluding the possibility of an external magnetic field effect.

In addition, on this day no M5+ EQs have been recorded from the USGS seismic network in a 1500 km area around the M7.2 EQ epicentre, so the anomaly is a great candidate as a possible precursor of the earthquake. From Swarm-CSES-01 joint analysis, the anomaly lasts for several hours from about 9:35 UTC to 17:10 UTC (i.e. 7 h and 35 min), still with a possible residual at 21:15 UTC. The peak of intensity of the anomaly has been recorded by nighttime passage of CSES-01 satellite in the area at 14:35 UTC, reaching a significant anomaly of 20 nT peak-to-peak, which seems in any case too much for a seismo-induced phenomenon.

Fig. 7 shows a CSES-01 anomalous track detected the day before the previous case. Also this anomaly is quite interesting: in fact, the highest intensity is in the Y-East component as expected for internal anomalies (Pinheiro et al., 2011) and it is the only anomaly in the whole track between 50° South and 50° North of geomagnetic latitude. In addition, also this track presents an anomaly intensity in the Y component of about 20 nT. The geomagnetic conditions were quiet (geomagnetic indices: Dst = −1 nT, ap = 4 nT and AE = 24 nT; source: World Data Center for Geomagnetism, Kyoto, http://wdc.kugi.kyoto-u.ac.jp/) and the anomaly is localised over land, in the southern segment of the plate boundary and at the border (but inside) the Dobrovolsky area. It is interesting to notice that the anomalies appear in the magnetic field components (larger in the Y-component) but not in the total intensity: this implies that the perturbation rotates the magnetic field vector without changing its intensity.

Fig. 8 shows a CSES-01 magnetic field track that contains a decrease

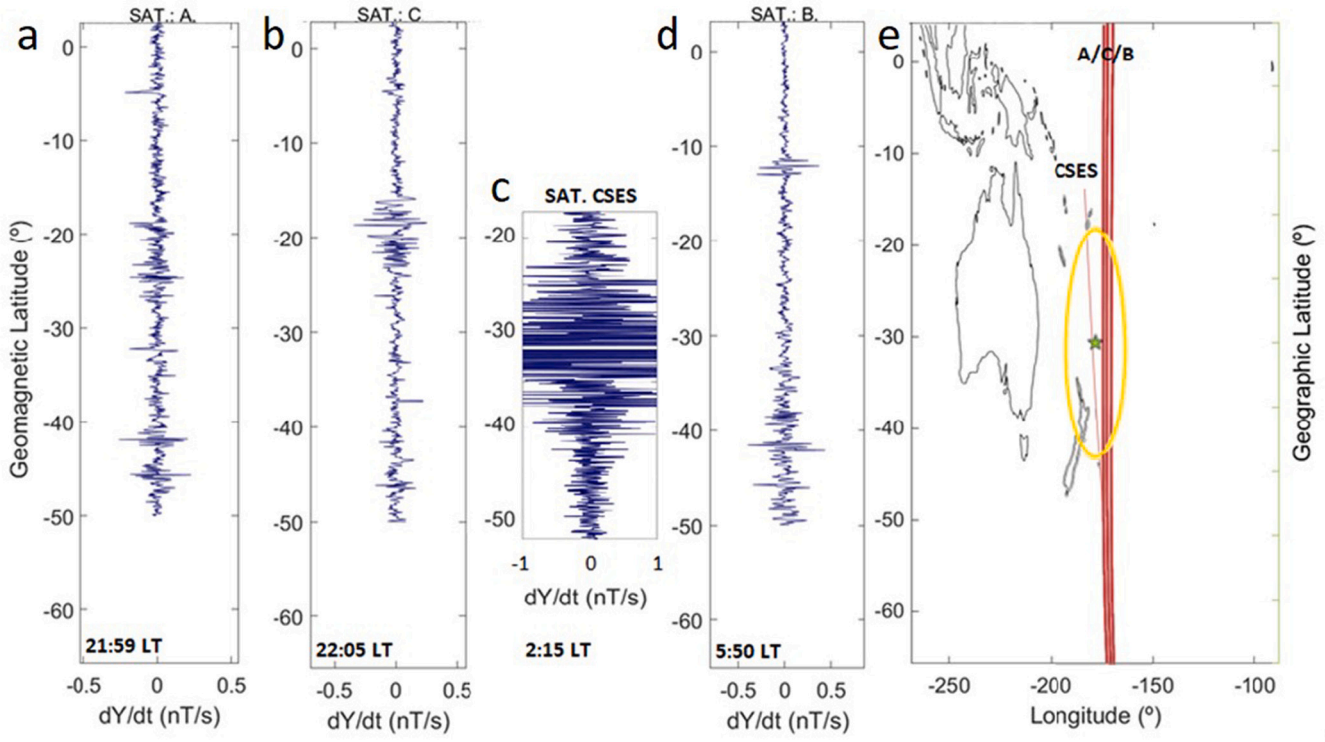

Fig. 6. Magnetic field Y-component analysis using the classic MASS method (Method 1) in different tracks of Swarm A (a), B (b), C(d) and CSES-01 (c) on 25 February 2019 for the local time windows as indicated in the form hh:mm. Red lines in panel e (with the geographical map) correspond to the four satellites' paths. The yellow oval is the Dobrovolsky area; the star is the EQ epicentre. (For interpretation of the references to colour in this figure legend, the reader is referred to the web version of this article.)

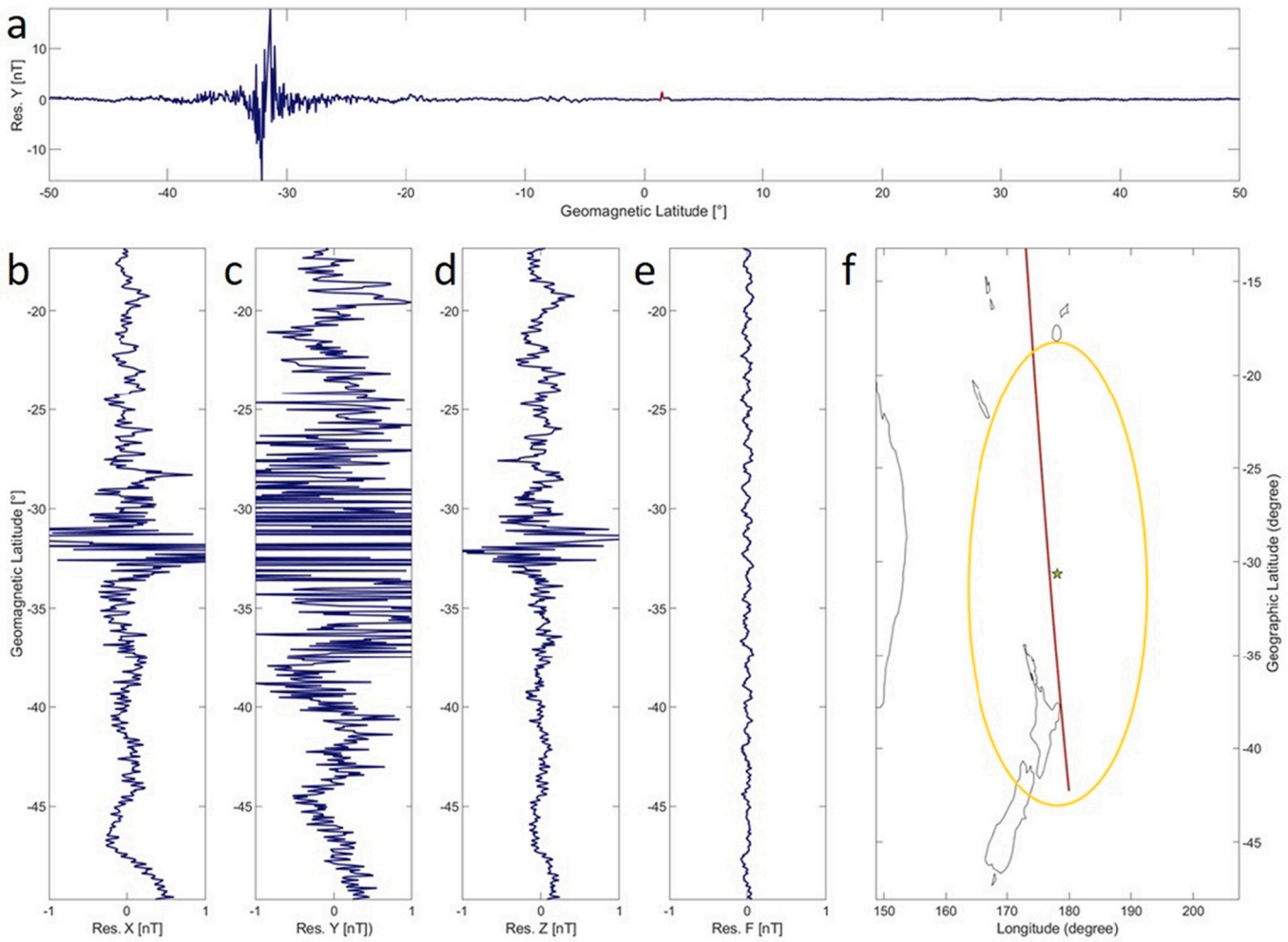

Fig. 7. Anomalous magnetic track of CSES-01 on 24 February 2019 analysed by method 3. a) Residuals of Y component vs. time; Residuals of (b) X, (c)Y, (d) Z and (e) F and (f) geographical map. The yellow oval is the Dobrovolsky area; the star is the EQ epicentre; the red line is the satellite path. (For interpretation of the references to colour in this figure legend, the reader is referred to the web version of this article.)

of Y-East component of magnetic field around the future epicentral latitude (extended a little northern). The track, acquired in geomagnetic quiet time (with Dst = −4 nT, ap = 4 nT and AE = 225 nT), shows a little geomagnetic activity at higher latitudes but the level is not anyway so strong.

Fig. 9 shows the track acquired by Swarm Charlie only 22 h and 36 min before the event. We notice a certain similarity of the anomaly with the track acquired 15 min before the Ridgecrest (California, USA) M7.1 EQ occurrence (see Fig. 1 of Marchetti et al., 2020). In addition, the ionospheric plasma has been investigated, with particular attention to the electron density Ne, to search for possible pre-earthquake ionospheric disturbances by the NeLOG algorithm (see De Santis et al., 2019a, for a full description of the method). NeLOG analyses the decimal logarithm of Ne by a 10-degree polynomial fit (red lines in Fig. 10a) and calculates the residual. If a sample overpasses by k_t times the standard deviation of the residual, it is marked by a blue asterisk in the figure. The method then classifies the track as "anomalous" if it contains >10 anomalous samples in the Dobrovolsky area. Fig. 10 shows an interesting example of an anomalous Ne track of Swarm Alpha satellite acquired 119 days before the M7.2 Kermadec Islands (New Zealand) EQ. This track shows a clear enhancement of Ne at a geomagnetic latitude of about −28° similar to the example shown in De Santis et al., 2021 with CSES-01 satellite in the case of a smaller magnitude earthquake. The track has been acquired during geomagnetic very quiet conditions (Dst = −6 nT and a_p = 0 nT). The same track is given in the Supplementary Material (Fig. S13) where, together with Ne, also the tracks of Te and Vs of Swarm-A satellite are shown.

On 1 June 2019, i.e. two weeks before the mainshock, Swarm Alpha detected an interesting electron density latitudinal profile that crossed the longitude of the incoming earthquake epicentre during nighttime and quiet geomagnetic conditions (see Fig. 11). The red box enlightens a part of the Ne profile that seems to be anomalously increased in terms of its absolute value between −44° and − 29° of latitude. Furthermore the same track shows two perturbations around the mean track value highlighted by continuous and dashed red ovals. Interestingly, all such anomalous features are localised inside the Dobrovolsky area and, in particular, the stronger perturbation, underlined by the continuous red oval, is localised at the same latitude of the future epicentre. Such perturbations not only are unusual at night time LT = 01:13 AM but also are localised southern of the typical geomagnetic latitude of the possible residual of daily EIA that could appear at about −15° / -20° geomagnetic latitude, and also sufficiently far from the South pole. Therefore for exclusion the remaining hypothesis on its origin could be a seismo-induced phenomenon.

3.4. Total Electron Content (TEC) data analysis

TEC data from GNSS receivers can also be analysed to detect electromagnetic anomalies possibly related to impending earthquakes. Vertical TEC (vTEC) data calibrated applying the techniques described

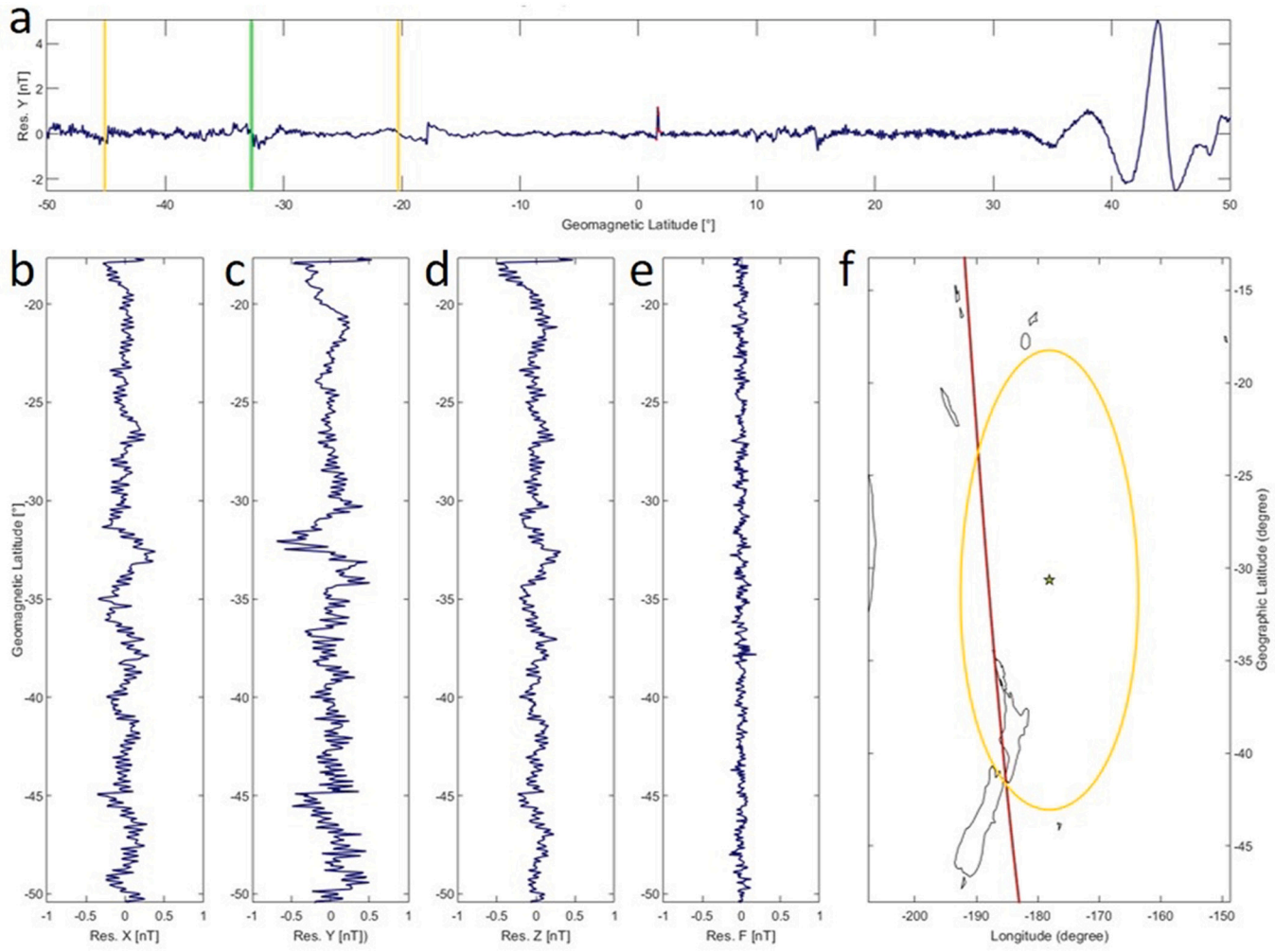

Fig. 8. As Fig. 7 but on 30 April 2019 analysed by method 3. In (a), the vertical lines represent epicentral latitude (green) and limits of the Dobrovolsky area (yellow). In (f), the green star represents the epicentre location while the yellow circle is the corresponding Dobrovolsky area. (For interpretation of the references to colour in this figure legend, the reader is referred to the web version of this article.)

in Ciraolo et al. (2007) and Cesaroni et al. (2015) to RINEX data recorded from 4 months preceding up to 1 month after the earthquake occurrence at selected stations of the GeoNet GNSS/GPS network are used for this purpose, i.e. RAUL, GLKZ and PYGR (see Fig. 1b).

Anomalous variations of vTEC are defined following four different approaches, respectively applied to a single station (method **1**, applied to data close to the epicentre), two stations (methods **2** and **3**, consisting of differential analyses between data close to the epicentre and rather distant ones), and three stations (method **4**, differential analysis among data from stations at different distances from the epicentre). For all the methods, geomagnetic conditions are taken into account in order to exclude anomalies of external origin.

Among such approaches, the two-station differential analysis of method **3** seems to be the most promising, and is presented here in detail (for the detailed definitions and analyses by the other methods, see the Supplementary Material). In this method, the vTEC relative deviations (dTEC) between data of a couple of distant receivers is considered, in the specific:

$$\mathrm{dTEC} = (\mathrm{vTEC}_{\mathrm{RAUL}} - \mathrm{vTEC}_{\mathrm{PYGR}})/\mathrm{vTEC}_{\mathrm{PYGR}}, \quad (5)$$

being RAUL receiver (29.24° S; 177.93° W) the closest available to the earthquake epicentre, with a distance of 156 km, while PYGR (46.17° S; 166.68° E) is the most distant one among those of the GeoNet network, with a distance of about 2170 km (Fig. 1b). This means that dTEC large values reflect vTEC large values near the epicentre in correspondence to lower values outside the earthquake preparation zone, being then considered possibly affected by pre-earthquake processes.

In method **3**, the anomalies are defined by comparing the dTEC values calculated every 30 s to the mean linear trend m of the linear fit to data within the 4 months prior to the earthquake. In this case, an anomaly is defined as a set of dTEC values continuously exceeding $m + 2$ TECU (corresponding to about $m + 3.5\sigma$ in case of a Gaussian distribution of the residuals) for at least 5 min. The anomalies occurred under disturbed geomagnetic conditions are discarded, where $|\mathrm{Dst}| > 20$nT or AE $>$ 200 nT conditions are applied to the instantaneous and daily maxima of the corresponding geomagnetic indices as a proxy of disturbed conditions. Fig. 12 shows the application of this method to the earthquake under analysis. In the same figure also the EQ occurrences are shown together with their range of magnitudes (when more than one EQ occurred on the same day and in the Dobrovolsky area).

This analysis revealed three possible precursory anomalies, some of which were detected also using different approaches. In particular, the 18 March anomaly is recognized also by method **2** (Fig. S16 in the Supplementary Material), and the one of 5 June by both methods **1** applied to RAUL data (Fig. S15) and method **2**, despite the latter confirming the anomaly only with respect to the first background (Fig. S16a). It should be noted here that the application of method **4** for the three-station differential analysis revealed only an anomaly on 18 March, detected also by both the methods for the two-station differential

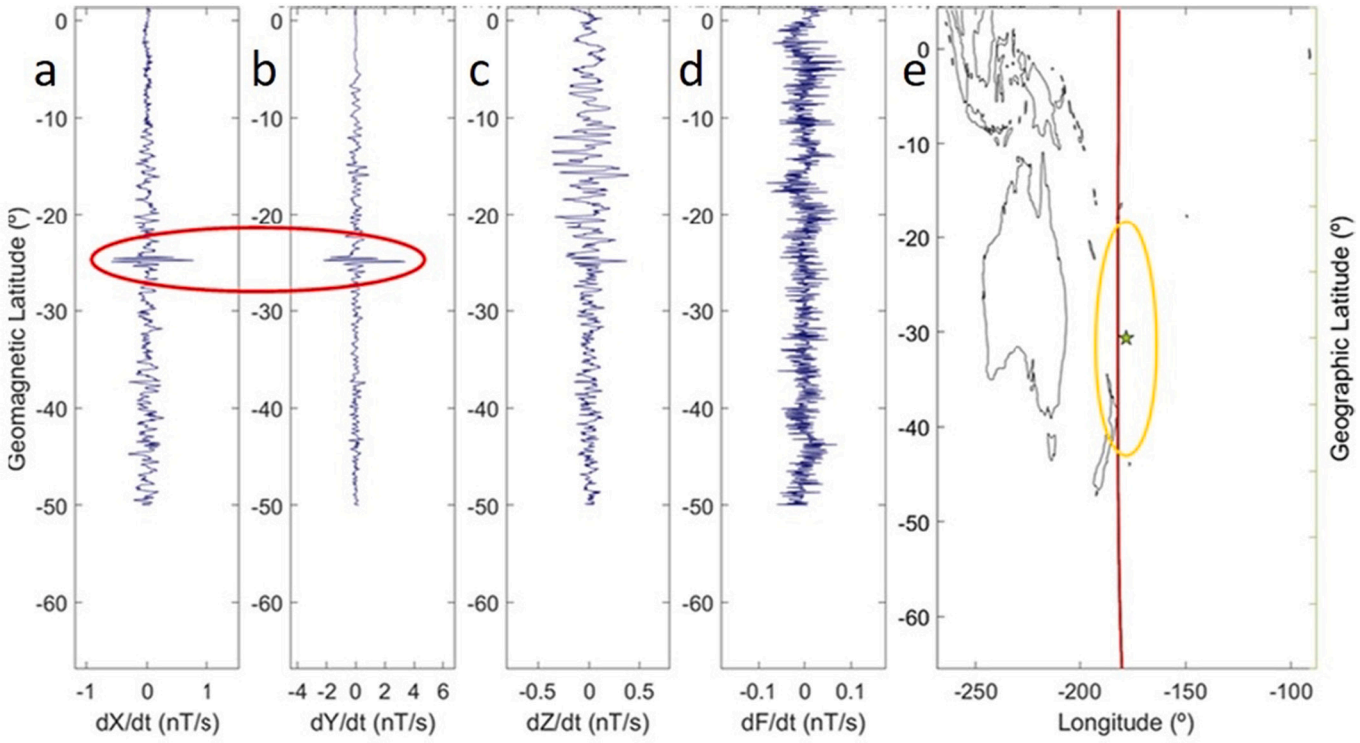

Fig. 9. Anomalous magnetic track of Swarm Charlie on 15 June 2019 (the day of the earthquake) analysed by method 1 (MASS), showing the first differences of a) X, b) Y, c) Z magnetic field components and d) total intensity; e) geographical map with Dobrovolsky area (yellow), satellite orbit (red) and epicentre (green star). (For interpretation of the references to colour in this figure legend, the reader is referred to the web version of this article.)

analysis, as possibly related to the impending earthquake. Of course, we cannot exclude that some anomaly could be associated to a closer EQ with lower magnitude (indicated by a vertical green arrow in Fig. 12), but since the discrimination is impossible, we attribute all found anomalies to the preparation of the largest magnitude M7.2 EQ of interest.

The Supplementary Material also presents the same analysis but applied to the same 4-month period of the 2018 year as confutation analysis. Please note that this tectonic area is very active seismically so it is almost impossible to find periods without significant seismicity: we chose 2018 because only two M5.7+ EQs (actually one outside but close to the period of interest) occurred in this period (while in the investigated 2019 year there were 9 EQs). Also in 2018 there are some anomalies, but many less than in 2019, and those occurred could be precursors of the few EQs occurred in this period of 2018.

3.5. CSES-01 Search Coil Magnetometer and Electric Field Detector spectral analysis

Spectral analysis of magnetic and electric signals acquired by Search Coil Magnetometer (SCM) and Electric Field Detector (EFD), working on board CSES-01 satellite (Wang et al., 2018), were also considered in the period 1 June - 13 July 2019. In particular, we analysed magnetic and electric field variations in the Extremely Low Frequency band (ELF, 200–2200 Hz, with 10.24 kHz and 5.12 KHz sampling rate, respectively). Our aim is to detect anomalies preceding large earthquakes, by means of the evaluation of the spectral information content emerging in some frequency band, in similar way as applied in previous case studies (e.g. Carbone et al., 2021; Piersanti et al., 2020; Wang et al., 2018). Fig. 13 shows the CSES-01 orbit 74,991 (day 10 June 2019), passing through the Dobrovolsky area (green circle) of the Kermadec Islands (New Zealand) EQ, while Fig. 14 illustrates the spectrograms of both SCM (a) and EFD (b) in the ELF band.

Observing the spectrograms of the magnetic field (all three components) and the electric field (mainly Y and Z components), we can see the presence of a possible anomaly within the Dobrovolsky area at frequencies lower than around 500 Hz (see Fig. 14).

To better study this anomaly, we resorted to the concept of Shannon Entropy (Shannon, 1948). A spectrogram represents the temporal variation of the power spectral density; starting from this, at any moment the entropy H(S) associated with the spectrum S is calculated as defined by Shannon (1948):

$$H(S) = -\sum_{i=1}^{N} p(s_i) \cdot log_{10} p(s_i) \quad (6)$$

where S is a discrete random variable that can assume N distinct values $s_1, \ldots, s_N$ and the probability function $p(s_i)$ represents its statistical distribution. The results are shown in the Fig. 15, which represents the trends of the normalised entropy $H(S)/log_{10}N$ as time varies, for the magnetic and the electric fields. Entropy is higher if there is decorrelation between samples, while it is lower when values $s_1, \ldots, s_N$ are correlated.

As you can see, in the area near the epicentre there seems to show a clear correlation between the samples of the spectrum of magnetic and electric fields, while elsewhere these seem to be less correlated with each other.

The main feature that emerges from both the magnetic and electric field spectrograms (Fig. 14) is the power concentration around the Dobrovolsky area (green vertical lines) in a limited region of the spectrum (below and close to 500 Hz). A similar anomaly frequency was detected for 2009 L'Aquila EQ (in that case it was 330 Hz; Bertello et al., 2018). The energy concentration in a limited range of frequencies reflects in the evident concave behaviour in the entropy (Fig. 15). A deeper inspection reveals the same power concentration in the equivalent spectral band ($f \leq 500$ Hz) in both magnetic and electric field spectra, in a portion of the orbit (latitude interval) which is the symmetrical counterpart with respect to the magnetic equator (see Fig. 13). Although less energetic (and so less clear), of course this similar feature emerges,

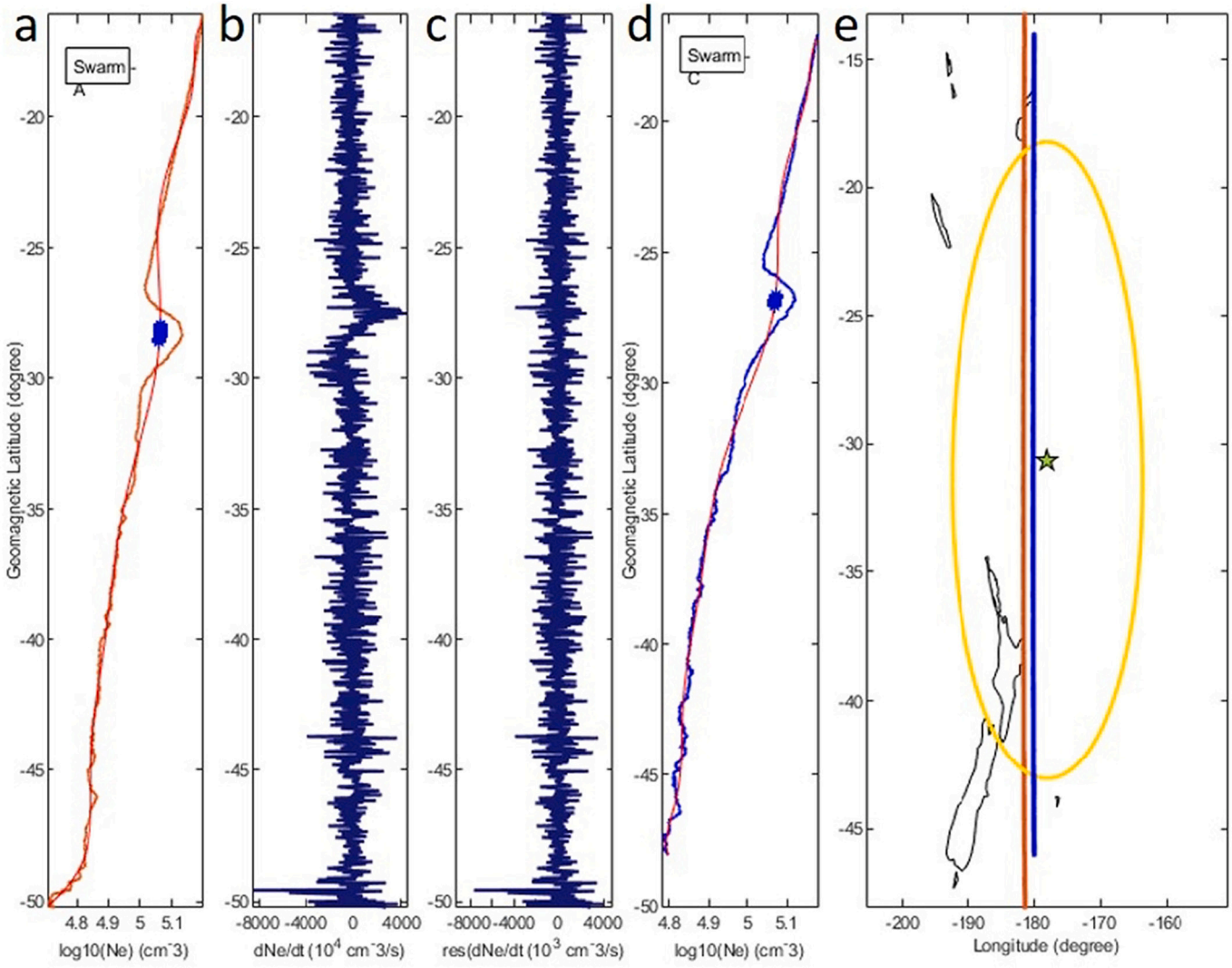

Fig. 10. Anomalous electron density Ne track of Swarm Alpha on 16 February 2019 (~119 days before the mainshock) elaborated by NeLOG with $k_t = 2.5$. From left the figure shows: a) the log Ne, b) the first differences of Ne and c) residual with respect to the mean polynomial trend for satellite Alpha; then it shows d) the log Ne for Swarm Charlie. The two orbits are shown in the geographic map in e): red for Alpha and blue for Charlie. (For interpretation of the references to colour in this figure legend, the reader is referred to the web version of this article.)

correspondingly, in their entropies, where the evident depression around the Dobrovolsky area replicates to a lesser extent in the symmetric area, delimited by the magenta vertical lines (Fig. 15). A clear and founded explanation requires a deeper and focused inspection. Nonetheless, a simple speculation could be that the entropy decreases over the preparation area (represented by the Dobrovolsky region) because of the coupling between the lithosphere under stress and the above ionosphere (through the atmosphere in the between); and that coupling reflects to the symmetric latitudes through the current system along the magnetic field lines (e.g. Sorokin et al., 2019).

4. A comparison with 2019 M7.1 Ridgecrest Earthquake

In this section, the occurrences of the various precursors of the Kermadec Islands EQ with those of Ridgecrest EQ (occurred on 6 July 2019 03:19:53 (UTC) - 35.770°N 117.599° W, 8.0km depth) are compared. The likeness of the pre-earthquake anomalies between the two earthquakes is instructive because the two earthquakes have similar magnitudes, although they occurred in two very different tectonic contexts. Table 1 summarises the occurrences of the anomalies, where the number corresponds to the day with respect to the EQ occurrence, being in bold black those of Kermadec Islands EQ and in light black those of Ridgecrest EQ. The rows of the table are placed from top to bottom almost in altitude order, i.e. from lithosphere, atmosphere to ionosphere. In general, the anomalies tend to occur closer to the earthquake occurrence going up into the atmosphere and ionosphere. As shown by Table 1, the lithospheric anomalies (either in terms of *b*-value decrease and the beginning of the R-AMR acceleration) precede all the atmospheric and ionospheric anomalies. In addition, some atmospheric and ionospheric anomalies appear at almost the same time with respect to the EQ occurrence: impressive almost simultaneous precursors (within a 10-day interval) appear around 90 days before the EQ for aerosol (AOD and AOT), SKT, TCWV and TEC values. Interestingly, the final acceleration (increasing number of anomalies) occurs as the earthquake is approaching (say, in the last two weeks), especially in the ionosphere. Another consideration is speculative, trying to connect atmospheric to ionospheric anomalies: while some of the latter (here called **Case 1** ionospheric anomalies) occur well before the atmospheric anomalies (e.g. Y and Ne at >100 days), others (here called ***Case 2*** ionospheric anomalies) seem to occur with some delay (5–10 days) with respect to the atmospheric anomalies. This delay seems more typical of a diffusion propagation of the atmosphere-ionosphere coupling that requires a

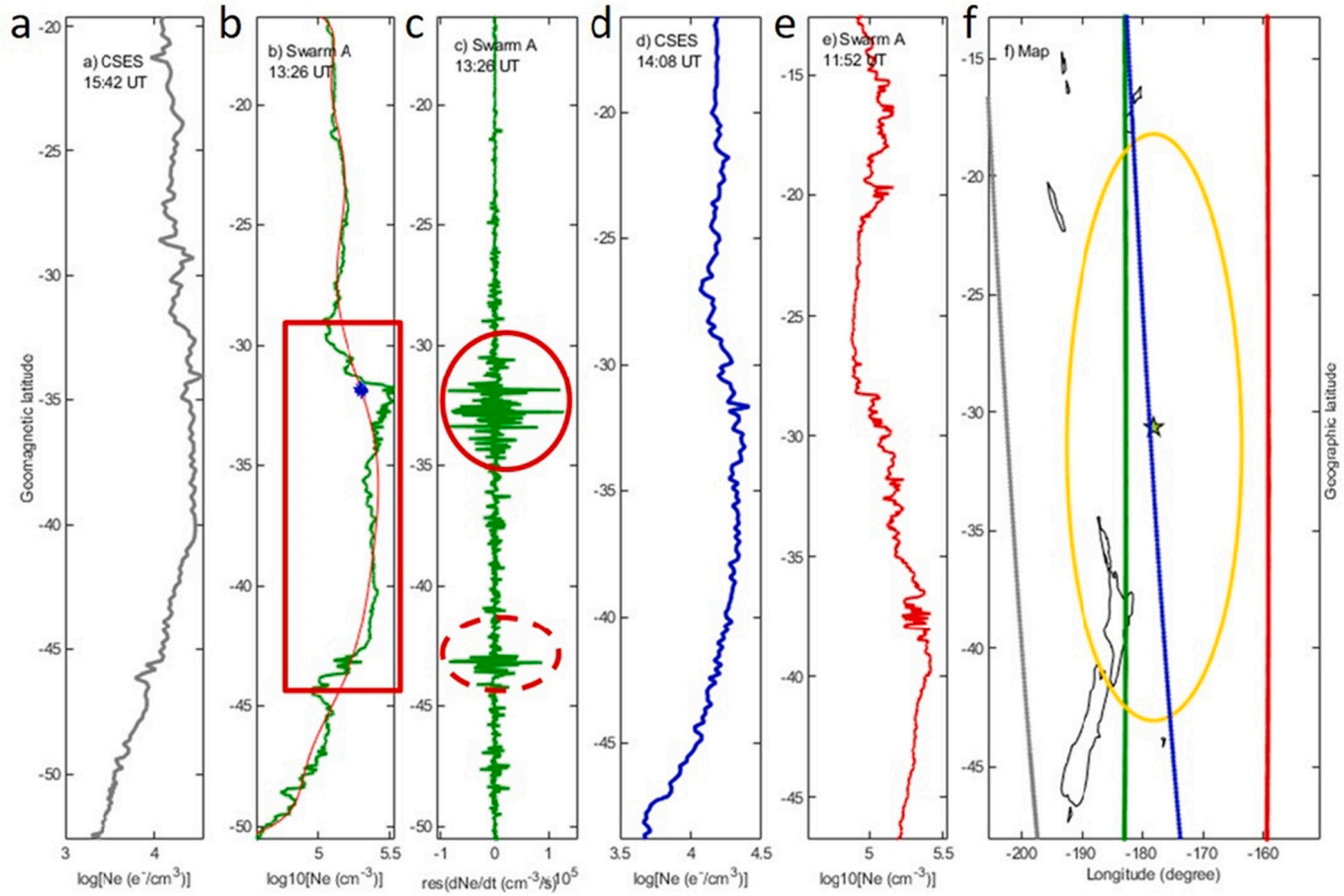

Fig. 11. CSES-01 and Swarm Alpha electron density tracks acquired on 1 June 2019 (~2 weeks before the mainshock). a) CSES-01 acquired at 15:42 UT; b) Swarm Alpha acquired at 13:26 UT; c) residual analysis by NeLog of track shown in b; d) CSES-01 track acquired at 14:08 UT; e) Swarm A acquired at 11:52 UT; f) map with the ground projections of the satellite tracks with the same colour used in the previous panels.

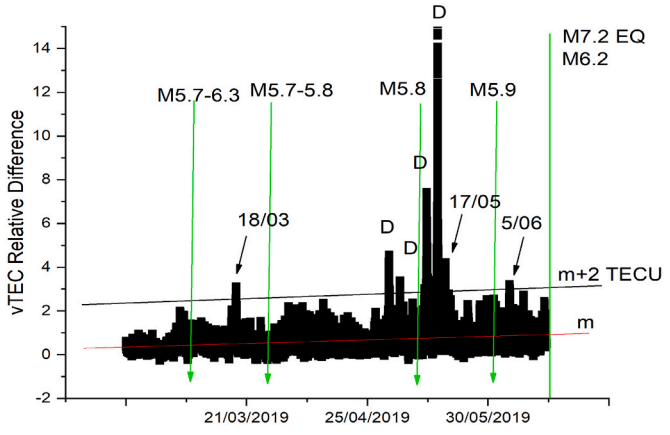

Fig. 12. vTEC two-station differential analysis (method **3**) for the 2019 M7.2 Kermadec Islands EQ. The black arrows indicate three anomalous days, while the vertical green line represents the time of the mainshock occurrence. D stands for disturbed ionosphere. In this figure, m is the mean trend (red line), and m + 2 (black line) is the chosen upper threshold for anomalies identification. The vertical green arrows represent the M5.7+ EQs occurred in the period of investigation (also the range of EQ magnitudes is shown). Please note that, on the same day of the M7.2 mainshock, another EQ occurred with magnitude 6.2.

mean vertical velocity of the order of 50–100 km/day and that produces the Case 2 anomalies in the ionosphere. The Case 1 anomalies in the ionosphere could be generated by a direct electromagnetic coupling between the lithosphere and the ionosphere, e.g. through the p-holes (Freund, 2011).

5. Discussion and conclusions

A full multiparametric and multilayer investigation of the case study of the M7.2 Kermadec Islands (New Zealand) 2019 EQ has been presented here. A chain of processes that start from the lithosphere and propagate through the atmosphere and finally reach the ionosphere is found through Table 1. In particular, we have analysed seismological, atmospheric, satellite and ground electromagnetic data to study the potential LAIC phenomena. The seismological data analysis showed that an acceleration took place during the preparation phase of the earthquake and the R-AMR technique predicted the magnitude of the impending EQ. From atmospheric data, several anomalies before the earthquake have been retrieved: AOD anomaly appears first around 100 days before the EQ, then followed by CH_4, SKT and TCWV around 90–80 days before the EQ. SO_2 anomaly appears around 60 days before the earthquake, almost together with another AOD anomaly. Among all atmospheric quantities, OLR is the last, appearing around 30–40 days before EQ. Finally SKT, TCWV and OLR show other anomalies around 15 days before EQ. Then 6 days before EQ, another AOD anomaly appears. The starting sequence of the anomalies resembles that found for two large Chinese earthquakes, i.e. 2008 M8 Wenchuan EQ and 2013 M7 Lushan EQ (Liu et al., 2020a), where AOD appeared >80 days before

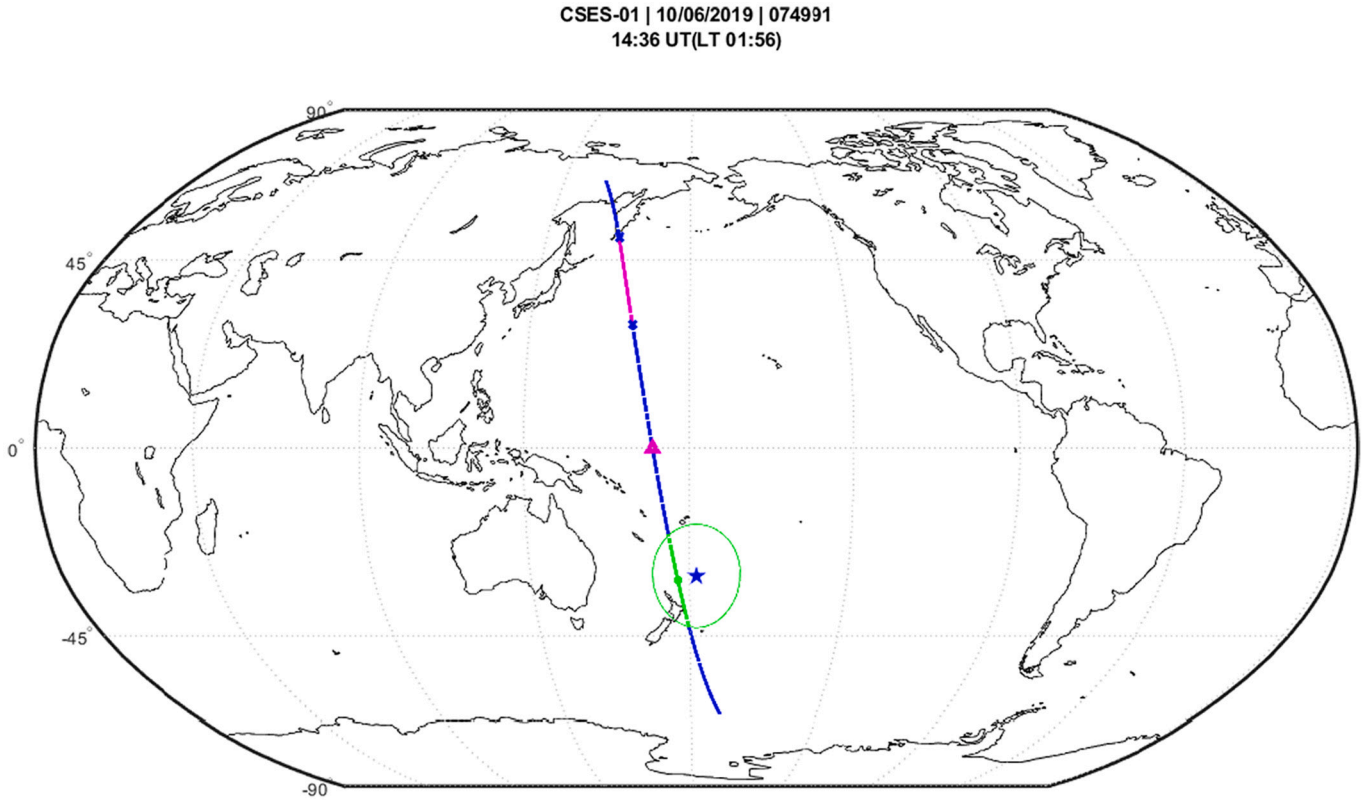

Fig. 13. Map showing the epicentre (blue star) of 2019 Kermadec Islands EQ, the corresponding Dobrovolsky area (green circle) and the track of the orbit number 74991 of CSES-01 (blue line). The green segment of the orbit inside the Dobrovolsky area corresponds to the interval within the solid green vertical lines in the spectrogram (Fig. 14); the magenta section in the upper part is its symmetric (with respect to the magnetic equator) counterpart. The small magenta triangle along the orbit represents the direction of the satellite fly (i.e. it is an ascending orbit). (For interpretation of the references to colour in this figure legend, the reader is referred to the web version of this article.)

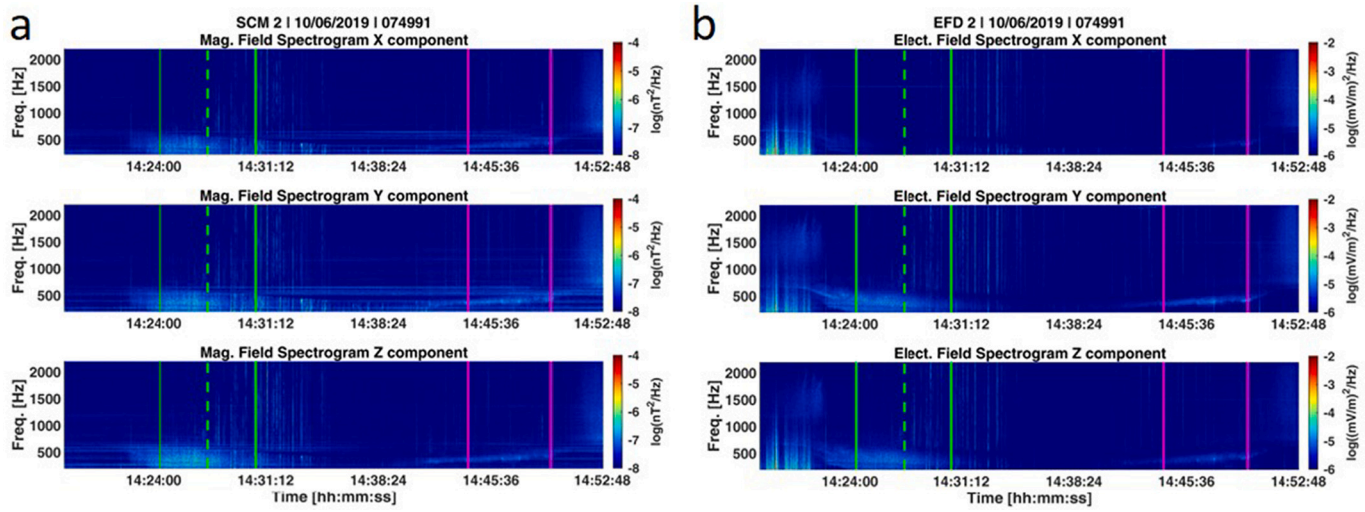

Fig. 14. Spectrograms of magnetic (a) and electric (b) field in the ELF band 5 days before the 2019 Kermadec Islands EQ (orbit number 74991). The solid green vertical lines correspond to the limits of the Dobrovolsky area; the dashed line indicates the time of the minimum distance between the epicentre and the orbit, while the area delimited by the magenta vertical lines represents the symmetric counterpart with respect to the magnetic equator. The intermittent noise of EFD at lower latitudes (well before 14:24:00) is very different from that within the Dobrovolsky region and probably due to some geomagnetic activity at the Auroral region. (For interpretation of the references to colour in this figure legend, the reader is referred to the web version of this article.)

EQ, preceding TCWV and SKT. The increase of aerosols before large earthquakes was already recognized >40 years ago (Tributsch, 1978) and confirmed in many subsequent works (e.g. Liperovsky et al., 2005; Liu et al., 2020a, 2020b). The appearance of a thermal anomaly at 90, 72, 25 and 15 days before the earthquakes of Ridgecrest or Kermadec Islands, shows that temperature is another important atmospheric precursor. Qin et al. (2012) analysed the temperature changes (in terms of air surface temperature and surface latent heat flux, SLHF) on occasion of two important 2010–2011 earthquakes in New Zealand (therefore in a region just a little more southern than the area of the present studied

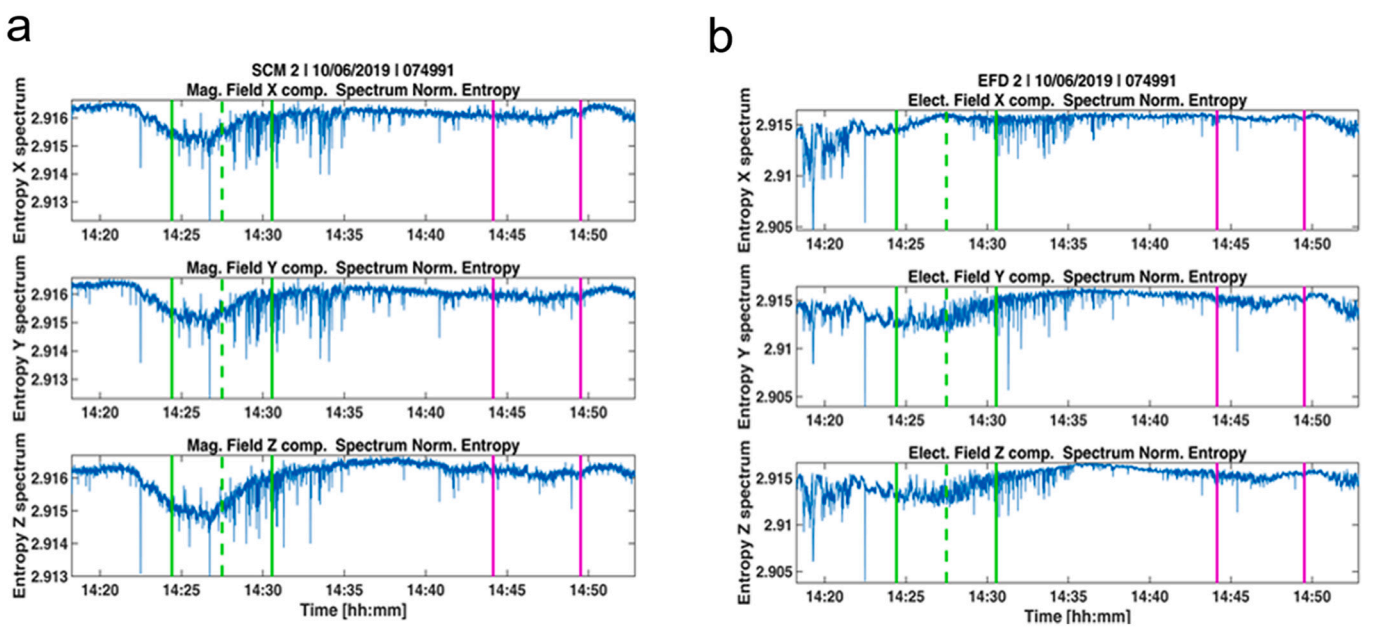

Fig. 15. Normalised entropy of power spectral densities of X,Y,and Z components of magnetic (a) and electric field (b) in the ELF band 5 days before the 2019 Kermadec Islands EQ (orbit number 74991). The solid green vertical lines correspond to the limits of the Dobrovolsky area; the dashed line indicates the time of the minimum distance between the epicentre and the orbit, while the area delimited by the magenta vertical lines represents the symmetric counterpart with respect to the magnetic equator. The large variability at the beginning of the electric field signal corresponds to perturbation at higher latitudes, so it is not related to pre-earthquake phenomena. (For interpretation of the references to colour in this figure legend, the reader is referred to the web version of this article.)

Table 1
Multi-precursor anomalies and their occurrence in terms of the day to the earthquake (Kermadec Islands EQ anomalies in bold black, Ridgecrest EQ anomalies in light black).

	Days to EQ	> 120	120	99	89	79	69	59	49	39	29	19	9
	from		-	-	-	-	-	-	-	-	-	-	-
	-		100	90	80	70	60	50	40	30	20	10	0
	to												
	b-value	**290**											
Lithosphere	R-AMR	**180**											
	D			90		75	65,60						
	AOD						**59**						
	AOT		**100–103**				60						**6**
	SKT			**93**									
				90		75					25	**15**	
Atmosphere	TCWV			**92**	85	**75**						**15**	
	CH_4			**99**		70					**20–22**		
	SO_2						**66**					**12**	
	OLR									**36, 30**		**15**	
	Ionosonde									34			
	IONO1												7
Ionosphere	TEC				**89**						**29**	**10**	
	ELF												**5**
	Y		**110**				65–70						**1**
	Ne		**109–119**										

Bold Black: Kermadec Islands (NZ) M7.2 EQ (this article).
Light Black**:** Ridgecrest (USA) M7.1 EQ.
D > 0 strength parameter Ridgecrest EQ – incremental part of the stresses (Bondur et al., 2020).
SKT, TCWV, CH_4, AOT, Ionosonde, Swarm Y mag. field (De Santis et al., 2020).
IONO1 - Ionospheric variability – Ridgecrest EQ (Pulinets et al., 2021).

earthquake) and noticed that there were some series of thermal anomalies at about 30 days before the mainshock (3 Sept. 2010 M7.1) and 60 and 3–4 days before the largest aftershock (21 February 2011 M6.3). Qin et al. (2012) also proposed four possible different mechanisms of Lithosphere- (Coversphere)-Atmosphere coupling: magmatic-hydrothermal fluids upwelling, soil moisture increasing, underground pore gases leaking, and positive holes activating and recombining.

Magnetic field and electron density data analyses from Swarm and CSES-01 satellites detected some interesting anomalies. In particular, a magnetic anomaly has been detected on 25 February 2019 during nighttime: comparing the different satellites (Swarm and CSES-01) that crossed the same region at different times, it was possible to follow the temporal evolution of the anomaly. In addition, not shown here, a clear increase of electron density was identified on the night of 26 February 2019, noticing that the maximum Ne value was very close to the future epicentre of the earthquake, and the solar conditions were relatively quiet (see Supplementary Material). Thanks to the orbital sun-synchronous configuration of CSES-01 (precisely at the same

nighttime or daytime), it was possible to confirm that Ne was incremented during deep nighttime, by reducing the chances that it could be just a residual of the daily activity. Furthermore, it was possible to confirm the consistency of Ne latitudinal profiles between CSES-01 and Swarm satellite missions. Another satellite payload analysed here was the Electric Field Detector on board CSES-01 satellite. An anomaly within the Dobrovolsky area, more evident in Y and Z components and similar to what was already detected in the spectrograms of the magnetic field from Search Coil Magnetometer was observed. Finally, from ground GNSS data analysis we have considered TEC data and identified three possible precursory anomalies, some of which were detected also using different approaches, from around 90, 30 and 10 days before the earthquake.

Preliminary conclusions show the necessity of integrating multiple datasets to better understand the preparation phase of medium-large earthquakes. Furthermore, the importance of the CSES-01 satellite, in conjunction with the Swarm satellites, has been shown in several contexts, not only useful to better constrain the state of the ionosphere, but also to find several disturbances possibly related to the earthquake occurrence. It has been seen that some of these characteristics have also been detected by the Swarm three-satellite constellation, proving the good integration between both satellite datasets and the potential of the methodology applied.

From the obtained results, summarised by Table 1, two kinds of LAIC can be found: one is practically direct, so its nature should be electromagnetic, as due to the release of p-holes and their propagation up to the ionosphere. The other is more typical of a thermodynamic diffusion process, probably due to a change of temperature and humidity that starts at the ground-atmosphere interface and slowly propagates through the atmosphere up to the ionosphere. A comprehensive way to collect all data anomalies is plotting the cumulative number of all anomalies for Kermadec Islands EQ with time (Fig. 16). A power law as given by eq. (1) fits very well the data pointing to the time of EQ occurrence. This agrees with the analogous power law behaviour of the cumulative number of anomalies for Ridgecrest EQ (De Santis et al., 2020), as approaching to the EQ occurrence. We point out that a power-law behaviour in time is typical of critical systems approaching a critical point where there is a significant change of the system properties (e.g. De Santis et al., 2019c). In this scenario, the EQ is a critical point of the lithosphere, and its imminent occurrence leaves some clues also in the atmosphere and ionosphere, because of their coupling with the lithosphere during the EQ preparation phase.

The results we found in this work were not obtained by chance: the Supplementary Material shows also a confutation analysis, either considering a random simulation or another year (i.e. 2018) without significant seismicity. In the former case, as expected the cumulative number of anomalies does not resemble a power law but a linear trend; in the latter case, when applied to the atmospheric and TEC data analyses, the anomalies are almost absent or just a few, i.e. many less than those found in the year of the earthquake.

The present results confirm those of previous case studies, such as the 2015 Mw7.8 Nepal EQ (De Santis et al., 2017), the 2016 Mw7.8 Ecuador EQ (Akhoondzadeh et al., 2018), the 2017 Mw7.3 Iran-Iraq border EQ (Akhoondzadeh et al., 2019), the 2018 Mw7.5 Indonesia EQ (Marchetti et al., 2019) and the 2019 Mw7.1 Ridgecrest California EQ (De Santis et al., 2020).

In the future perspective, we would like to extend this multi-parametric and multi-layer approach to new case studies, especially occurring during the Swarm and CSES-01 data simultaneous availability. We plan to present full multiparametric and multilayer investigations also of other large earthquakes with comparable magnitude. For instance, we could also extend the analysis to more recent cases, such as M7.1 Japan and the two concomitant events of 21 May 2021 in China (Madou Mw7.3 and Yangbi Mw6.1). Moreover, the intercomparison of all new and old results will allow us to confirm the chain of anomaly occurrences of different parameters and then validate the best LAIC model.

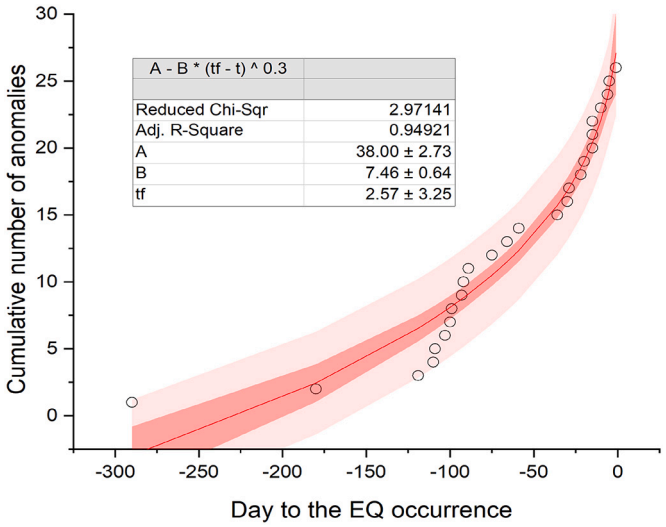

Fig. 16. Cumulative number of the anomalies found for Kermadec Islands EQ vs. time: the best fit (bold red curve) is a power law similar to eq. (1) that points to the EQ occurrence. The red band around the best fit is the 95% confidence interval, while the pink band is the 95% prediction band. (For interpretation of the references to colour in this figure legend, the reader is referred to the web version of this article.)

CRediT authorship contribution statement

A. De Santis: Funding acquisition, Conceptualization, Supervision, Methodology, Writing – original draft, Writing – review & editing. **L. Perrone:** Funding acquisition, Methodology, Writing – review & editing. **M. Calcara:** Investigation, Writing – review & editing. **S.A. Campuzano:** Methodology, Software, Validation, Writing – review & editing. **G. Cianchini:** Methodology, Software, Validation, Writing – review & editing. **S. D'Arcangelo:** Visualization, Investigation, Writing – review & editing. **D. Di Mauro:** Investigation, Writing – review & editing. **D. Marchetti:** Software, Validation, Visualization, Writing – review & editing. **A. Nardi:** Investigation, Writing – review & editing. **M. Orlando:** Software, Validation, Visualization, Writing – review & editing. **A. Piscini:** Software, Validation, Visualization, Writing – review & editing. **D. Sabbagh:** Software, Validation, Visualization, Writing – review & editing. **M. Soldani:** Software, Validation, Visualization, Writing – review & editing.

Declaration of Competing Interest

We, authors of the present paper, declare that there is no conflict of interest.

Data availability

data are available at weblink given in the manuscript

Acknowledgements

This work was undertaken in the framework of Limadou-Science+ funded by ASI (Italian Space Agency). Part of the funds were also given by Working Earth (Pianeta Dinamico) Project. We thank GeoNet (NZ) for providing TEC data (we also thank Claudio Cesaroni and Luca Spogli for giving suggestions on TEC data analyses) and the Kyoto World Data Center for Geomagnetism (http://wdc.kugi.kyoto-u.ac.jp/) for providing geomagnetic data indices. ESA is thanked for providing the Swarm satellite data and the CNSA (Chinese National Space

Administration) for providing CSES-01 satellite data.

Appendix A. Supplementary data

Supplementary data to this article can be found online at https://doi.org/10.1016/j.rse.2022.113325.

References

Akhoondzadeh, M., De Santis, A., Marchetti, D., Piscini, A., Cianchini, G., 2018. Multi precursors analysis associated with the powerful Ecuador (MW = 7.8) earthquake of 16 april 2016 using swarm satellites data in conjunction with other multi-platform satellite and ground data. Adv. Space Res. 61, 1, 248–263. https://doi.org/10.1016/j.asr.2017.07.014.

Akhoondzadeh, M., De Santis, A., Marchetti, D., Piscini, A., Jin, S., 2019. Anomalous seismo-LAI variations potentially associated with the 2017 Mw=7.3 Sarpol-e Zahab (Iran) earthquake from Swarm satellites, GPS-TEC and climatological data. Adv. Space Res. 64, 1, 143–158. https://doi.org/10.1016/j.asr.2019.03.020.

Benioff, H., 1949. Seismic evidence for the fault origin of oceanic deeps. GSA Bull. 60 (12), 1837–1856. https://doi.org/10.1130/0016-7606(1949)60[1837:SEFTFO]2.0.CO;2.

Bertello, I., Piersanti, M., Candidi, M., Diego, P., Ubertini, P., 2018. Electromagnetic field observations by the DEMETER satellite in connection with the 2009 L'Aquila earthquake. Ann. Geophys. 36, 1483–1493. https://doi.org/10.5194/angeo-36-1483-2018.

Bondur, V.G., Gokhberg, M.B., Garagash, I.A., Alekseev, D.A., 2020. Revealing short-term precursors of the strong M > 7 earthquakes in Southern California from the simulated stress-strain state patterns exploiting geomechanical model and seismic catalog data. Front. Earth Sci. 8, 571700 https://doi.org/10.3389/feart.2020.571700.

Bowman, D.D., Ouillon, G., Sammis, C.G., Sornette, A., Sornette, D., 1998. An observational test of the critical earthquake concept. J. Geophys. Res. 103 (B10), 24. https://doi.org/10.1029/98JB00792.

Bufe, C.G., Varnes, D.J., 1993. Predictive modelling of the seismic cycle of the greater San Francisco Bay region. J. Geophys. Res. 98, 9871–9883.

Carbone, V., Piersanti, M., Materassi, M., Battiston, R., Lepreti, F., Ubertini, P., 2021. A mathematical model of lithosphere-atmosphere coupling for seismic events. Sci. Rep. 11, 8682. https://doi.org/10.1038/s41598-021-88125-7.

Cesaroni, C., Spogli, L., Alfonsi, L., De Franceschi, G., Ciraolo, L., Monico, J.F.G., Scotto, C., Romano, V., Aquino, M., Bougard, B., 2015. L-band scintillations and calibrated total electron content gradients over Brazil during the last solar maximum. J. Space Weather Space Clim. 5, A36. https://doi.org/10.1051/swsc/2015038.

Chiodini, G., Cardellini, C., Amato, A., Boschi, E., Caliro, S., Frondini, F., Ventura, G., 2004. Carbon dioxide earth degassing and seismogenesis in central and southern Italy. Geophys. Res. Lett. 31 (L07615), 1–4. https://doi.org/10.1029/2004GL019480.

Chiodini, G., Cardellini, C., Di Luccio, F., Selva, J., Frondini, F., Caliro, S., Rosiello, A., Beddini, G., Ventura, G., 2020. Correlation between tectonic CO2 earth degassing and seismicity is revealed by a 10-year record in the apennines, Italy. Sci. Adv. 6 (35), eabc2938. https://doi.org/10.1126/sciadv.abc2938.

Cianchini, G., De Santis, A., Di Giovambattista, R., et al., 2020. Revised accelerated moment release under test: fourteen worldwide real case studies in 2014–2018 and simulations. Pure Appl. Geophys. 177, 4057–4087. https://doi.org/10.1007/s00024-020-02461-9.

Ciraolo, L., Azpilicueta, F., Brunini, C., Meza, A., Radicella, S.M., 2007. Calibration errors on experimental slant total electron content (TEC) determined with GPS. J. Geod. 81 (2), 111–120.

Cussac, T., Clair, M.-A., Ultré-Guerard, P., Buisson, F., Lassalle-Balier, G., Ledu, M., Elisabelar, C., Passot, X., Rey, N., 2006. The Demeter microsatellite and ground segment, planetary and space science 413–427 (5), 0032–0633. https://doi.org/10.1016/j.pss.2005.10.013.

D'Arcangelo, S., Bonforte, A., De Santis, A., Maugeri, S.R., Perrone, L., Soldani, M., Arena, G., Brogi, F., Calcara, M., Campuzano, S.A., Cianchini, G., Del Corpo, A., Di Mauro, D., Fidani, C., Ippolito, A., Lepidi, S., Marchetti, D., Nardi, A., Orlando, M., Piscini, A., Regi, M., Sabbagh, D., Zhima, Z., Yan, R., 2022. A Multi-Parametric and Multi-Layer Study to Investigate the Largest 2022 Hunga Tonga–Hunga Ha'apai Eruptions. Remote Sensing. 14 (15), 3649. https://doi.org/10.3390/rs14153649.

Dascher-Cousineau, K., Lay, T., Brodsky, E.E., 2020. Two foreshock sequences post gulia and wiemer (2019). Seismol. Res. Lett. 91, 2843–2850.

De Santis, A., Cianchini, G., Di Giovambattista, R., 2015. Accelerating moment release revisited: examples of application to italian seismic sequences. Tectonophysics 639, 82–98. https://doi.org/10.1016/j.tecto.2014.11.015.

De Santis, A., Balasis, G., Pavón-Carrasco, F.J., Cianchini, G., Mandea, M., 2017. Potential earthquake precursory pattern from space: the 2015 Nepal event as seen by magnetic swarm satellites. Earth Planet. Sci. Lett. 461, 119–126.

De Santis, A., Marchetti, D., Spogli, L., Cianchini, G., Pavón-Carrasco, F.J., De Franceschi, G., Di Giovambattista, R., Perrone, L., Qamili, E., Cesaroni, C., et al., 2019a. Magnetic field and electron density data analysis from swarm satellites searching for ionospheric effects by great earthquakes: 12 case studies from 2014 to 2016. Atmosphere 10, 371. https://doi.org/10.3390/atmos10070371.

De Santis, A., Cianchini, G., Qamili, E., Frepoli, A., 2010. The 2009 L'Aquila (Central Italy) seismic sequence as a chaotic process. Tectonophysics 496 (1–4), 44–52. https://doi.org/10.1016/j.tecto.2010.10.005.

De Santis, A., Marchetti, D., Pavón-Carrasco, F.J., Cianchini, G., Perrone, L., Abbattista, C., Alfonsi, L., Amoruso, L., Campuzano, S.A., Carbone, M., Cesaroni, C., De Franceschi, G., De Santis, A., Di Giovambattista, R., Ippolito, A., Piscini, A., Sabbagh, D., Soldani, M., Santoro, F., Spogli, L., Haagmans, R., 2019b. Precursory worldwide signatures of earthquake occurrences on swarm satellite data. Sci. Rep. 9, 20287. https://doi.org/10.1038/s41598-019-56599-1.

De Santis, A., Abbattista, C., Alfonsi, L., Amoruso, L., Campuzano, S.A., Carbone, M., Cesaroni, C., Cianchini, G., De Franceschi, G., De Santis, A., Di Giovambattista, R., Marchetti, D., Martino, L., Perrone, L., Piscini, A., Rainone, M.L., Soldani, M., Spogli, L., Santoro, F., 2019c. Geosystemics view of earthquakes. Entropy 21 (4), 412. https://doi.org/10.3390/e21040412.

De Santis, A., Cianchini, G., Marchetti, D., Piscini, A., Sabbagh, D., Perrone, L., Campuzano, S.A., Inan, S., 2020. A multiparametric approach to study the preparation phase of the 2019 M7.1 Ridgecrest (California, USA) Earthquake. Front. Earth Sci. 8, 478. https://doi.org/10.3389/feart.2020.540398.

De Santis, A., Marchetti, D., Perrone, L., Campuzano, S.A., Cianchini, G., Cesaroni, C., Di Mauro, D., Orlando, M., Piscini, A., Sabbagh, D., Soldani, M., Spogli, L., Zhima, Z., Shen, X., 2021. Statistical correlation analysis of strong earthquakes and ionospheric electron density anomalies as observed by CSES-01. Nuovo Cimento C 2021, 4–5. https://doi.org/10.1393/ncc/i2021-21119-1.

Dobrovolsky, I.P., Zubkov, S.I., Miachkin, V.I., 1979. Estimation of the size of earthquake preparation zones. PAGeoph. 117, 1025. https://doi.org/10.1007/BF00876083.

Felzer, K.R., Abercrombie, R.E., Ekström, G., 2004. A common origin for aftershocks, foreshocks, and multiplets. Bull. Seismol. Soc. Am. 94 (1), 88–98.

Finlay, C.C., Kloss, C., Olsen, N., et al., 2020. The CHAOS-7 geomagnetic field model and observed changes in the South Atlantic anomaly. Earth Planets Space 72, 156. https://doi.org/10.1186/s40623-020-01252-9.

Freund, F., 2011. Pre-earthquake signals: underlying physical processes. J. Asian Earth Sci. 383–400.

Gelaro, R., McCarty, W., Suárez, M.J., Todling, R., Molod, A., Takacs, L., Randles, C.A., Darmenov, A., Bosilovich, M.G., Reichle, R., Wargan, K., Coy, L., Cullather, R., Draper, C., Akella, S., Buchard, V., Conaty, A., da Silva, A.M., Gu, W., Kim, G.-K., Koster, R., Lucchesi, R., Merkova, D., Nielsen, J.E., Partyka, G., Pawson, S., Putman, W., Rienecker, M., Schubert, S.D.C., Sienkiewicz, M., Zhao, B., 2017. The Modern-Era Retrospective Analysis for Research and Applications, Version 2 (MERRA-2). Journal of Climate 30 (14), 5419–5454. https://doi.org/10.1175/JCLI-D-16-0758.1.

Gulia, L., Wiemer, S., 2019. Real-time discrimination of earthquake foreshocks and aftershocks. Nature 574, 193–199. https://doi.org/10.1038/s41586-019-1606-4.

Hayakawa, M., Molchanov, O.A., 2002. Seismo Electromagnetics Lithosphere-Atmosphere-Ionosphere Coupling (ed. TERRAPUB) 477 pages, Tokyo.

Herrmann, M., Piegari, E., Marzocchi, W., 2022. Revealing the spatiotemporal complexity of the magnitude distribution and b-value during an earthquake sequence. Nat. Commun. 13, 5087. https://doi.org/10.1038/s41467-022-32755-6.

Liperovsky, V.A., Meister, C.-V., Liperovskaya, E.V., Davidov, V.F., Bogdanov, V.V., 2005. On the possible influence of radon and aerosol injection on the atmosphere and ionosphere before earthquakes. Natural Hazards and Earth System Sciences 5 (6), 783–789. https://doi.org/10.5194/nhess-5-783-2005.

Liu, Q., De Santis, A., Piscini, A., Cianchini, G., Ventura, G., Shen, X., 2020a. Multi-parametric climatological analysis reveals the involvement of fluids in the preparation phase of the 2008 ms 8.0 wenchuan and 2013 ms 7.0 lushan earthquakes. Remote Sens. 12, 1663. https://doi.org/10.3390/rs12101663.

Liu, Q., Shen, X., Zhang, J., Cui, J., Tan, Q., Zhao, S., Li, M., 2020b. Aerosol anomalies associated with occurrence of recent strong earthquakes (> M 8.0). Terr. Atmos. Ocean. Sci. 31, 677–689. https://doi.org/10.3319/TAO.2020.05.22.01.

Marchetti, D., De Santis, A., Shen, X., Campuzano, S.A., Perrone, L., Piscini, A., Di Giovambattista, R., Jin, S., Ippolito, A., Cianchini, G., Cesaroni, C., Sabbagh, D., Spogli, L., Zhima, Z., Huang, J., 2019. Possible lithosphere-atmosphere-ionosphere coupling effects prior to the 2018 Mw=7.5 Indonesia earthquake from seismic, atmospheric and ionospheric data. J. Asian Earth Sci. https://doi.org/10.1016/j.jseaes.2019.104097.

Marchetti, D., De Santis, A., Campuzano, S.A., Soldani, M., Piscini, A., Sabbagh, D., Cianchini, G., Perrone, L., Orlando, M., 2020. Swarm Satellite Magnetic Field Data Analysis Prior to 2019 Mw = 7.1 Ridgecrest (California, USA) Earthquake 12, 502. https://doi.org/10.3390/geosciences10120502.

McGuire, J.J., Boettcher, M.S., Jordan, T.H., 2005. Foreshock sequences and short-term earthquake predictability on East Pacific rise transform faults. Nature 434, 457–461. https://doi.org/10.1038/nature03377.

Mignan, A., 2011. Retrospective on the Accelerating Seismic Release (ASR) hypothesis: Controversy and new horizons. Tectonophysics 505 (1–4), 1–16. https://doi.org/10.1016/j.tecto.2011.03.010.

Mogi, K., 1963. Some discussions on aftershocks, foreshocks and earthquake swarms – the fracture of a semi-infinite body caused by inner stress origin and its relation to the earthquake phenomena (3). Bull. Earthquake Res. Inst. Univ. Tokyo 41, 615–658.

Mueller, S.C., 2019. Earthquake Catalogs for the USGS National Seismic Hazard Maps. Seismological Research Letters 90 (1), 251–261. https://doi.org/10.1785/0220170108.

Nanjo, K.Z., Yoshida, A., 2021. Changes in the b value in and around the focal areas of the M6.9 and M6.8 earthquakes off the coast of Miyagi prefecture, Japan, in 2021. Earth Planets Space 73, 176. https://doi.org/10.1186/s40623-021-01511-3.

Okal, E.A., 2019. Energy and magnitude: a historical perspective. Pure Appl. Geophys. 176, 3815–3849. https://doi.org/10.1007/s00024-018-1994-7.

Parrot, M., 2002. The micro-satellite DEMETER. J. Geodynam. 33 (4–5), 535–541. https://doi.org/10.1016/S0264-3707(02)00014-5.

Parrot, M., 2012. Statistical analysis of automatically detected ion density variations recorded by DEMETER and their relation to seismic activity. Ann. Geophys. 55 (1). https://www.annalsofgeophysics.eu/index.php/annals/article/view/5270.

Picozza, P., Conti, L., Sotgiu, A., 2021. Looking for earthquake precursors from space: a critical review. Front. Earth Sci. 14 https://doi.org/10.3389/feart.2021.676775.

Piersanti, M., Materassi, M., Battiston, R., Carbone, V., Cicone, A., D'Angelo, G., Diego, P., Ubertini, P., 2020. Magnetospheric–Ionospheric–Lithospheric coupling model. 1: observations during the 5 august 2018 bayan earthquake. Magnetospheric-ionospheric-lithospheric coupling model 1. Remote Sens. 12 (20), 3299. https://doi.org/10.3390/rs12203299.

Pinheiro, K.J., Jackson, A., Finlay, C.C., 2011. Measurements and uncertainties of the occurrence time of the 1969, 1978, 1991, and 1999 geomagnetic jerks. Geochem. Geophys. Geosyst. 12, Q10015.

Piscini, A., De Santis, A., Marchetti, D., Cianchini, G., 2017. A multi-parametric climatological approach to study the 2016 amatrice-norcia (Central Italy) earthquake preparatory phase. Pure Appl. Geophys. 174 (10), 3673–3688.

Piscini, A., Marchetti, D., De Santis, A., 2019. Multi-parametric climatological analysis associated with global significant volcanic eruptions during 2002–2017. Pure and Appl. Geoph. 176 (8), 3629–3647. (https://link.springer.com/article/10.1007%2Fs00024-019-02147-x).

Pulinets, S., Ouzounov, D., 2011. Lithosphere–atmosphere–ionosphere coupling (LAIC) model-an unified concept for earthquake precursors validation. J. Asian Earth Sci. 41 (4–5), 371–382. https://doi.org/10.1016/j.jseaes.2010.03.005.

Pulinets, S., Tsidilina, M., Ouzounov, D., Davidenko, D., 2021. From Hector mine M7.1 to ridgecrest M7.1 earthquake. A look from a 20-year perspective. Atmosphere 12, 262. https://doi.org/10.3390/atmos12020262.

Qin, K., Wu, L.X., De Santis, A., Meng, J., Ma, W.Y., Cianchini, G., 2012. Quasi-synchronous multi-parameter anomalies associated with the 2010–2011 New Zealand earthquake sequence. Nat. Hazards Earth Syst. Sci. 12, 1059–1072. https://doi.org/10.5194/nhess-12-1059-2012.

Scholz, C.H., 2015. On the stress dependence of the earthquake b value. Geophys. Res. Lett. 42 (5), 1399–1402. https://doi.org/10.1002/2014GL062863.

Shannon, C.E., 1948. A mathematical theory of communication. Bell Syst. Tech. J. 27, 379–423.

Shen, X., Zhang, X., Yuan, S., et al., 2018. The state-of-the-art of the China seismo-electromagnetic satellite mission. Sci. China Technol. Sci. 61, 634–642. https://doi.org/10.1007/s11431-018-9242-0.

Smith, E.M.I., Price, R.C., 2006. The Tonga-kermadec arc and Havre-lau back-arc system: their role in the development of tectonic and magmatic models for the western Pacific, J. Volcanol. Geothermal Res. 156. 3–4, 315–331. https://doi.org/10.1016/j.jvolgeores.2006.03.006.

Sorokin, V.M., Yashchenko, A.K., Surkov, V.V., 2019. Generation of geomagnetic disturbances in the ionosphere by a tsunami wave. Geomagn. Aeron. 59, 221–233. https://doi.org/10.1134/S0016793219020130.

Tributsch, H., 1978. Do aerosol anomalies precede earthquakes? Nature 276, 606–608. https://doi.org/10.1038/276606a0.

Wang, Q., Huang, J.P., Zhang, X.M., Shen, X.H., Yuan, S.G., Zeng, L., Cao, J.B., 2018. China seismo-electromagnetic satellite search coil magnetometer data and initial results. Earth and Planetary Physics 2 (6), 462–468. https://doi.org/10.26464/epp2018044.

Wiemer, S., 2000. Minimum magnitude of completeness in earthquake catalogs: examples from Alaska, the Western United States, and Japan. Bull. Seismol. Soc. Am. 90 (4), 859–869. https://doi.org/10.1785/0119990114.

Zhima, Z., Huang, J., Shen, X., Chen, L., Piersanti, M., Yang, Y., Wang, Q., Zeng, L., Lei, J., Chu, W., Zhao, S., Hu, Y., Guo, F., 2020. Simultaneous observations of ELF/VLF rising-tone quasiperiodic waves and energetic electron precipitations in the high-latitude upper ionosphere. J. Geophys. Res. Space. Physics Volume 125, Issue 5. https://doi.org/10.1029/2019JA027574.

Zhu, F., Jiang, Y., 2020. Investigation of GIM-TEC disturbances before M $\geq$ 6.0 inland earthquakes during 2003–2017. Sci. Rep. 10, 18038. https://doi.org/10.1038/s41598-020-74995-w.